Investigation of waste forms, engineered barriers, and the geological environment for the final disposal of radioactive waste

Thesis for the Degree of Doctor of Philosophy (PhD)

by **Vanda Papp**

Supervisor: Dr. Mónika Kéri, Senior Lecturer
(University of Debrecen)
Industrial Consultant: Dr. Róbert Janovics
(Isotoptech Ltd.)

UNIVERSITY OF DEBRECEN
Doctoral Council for Natural Sciences and Engineering
Doctoral School of Chemistry
Debrecen, 2025.

Hereby I declare that I prepared this thesis within the Doctoral Council for Natural Sciences and Engineering, ***Doctoral School of Chemistry****, University of Debrecen in order to obtain a PhD Degree in Natural Sciences/ Engineering at Debrecen University.*
The results published in the thesis are not reported in any other PhD theses.

Debrecen, 202. . . . .

…………………………….
Vanda Papp

Hereby I confirm that ***Vanda Papp*** *candidate conducted her studies with my supervision within the* ***K/4*** *Doctoral Program of the* ***Doctoral School of Chemistry between 2021 and 2025****. The independent studies and research work of the candidate significantly contributed to the results published in the thesis.*
I also declare that the results published in the thesis are not reported in any other theses.
I support the acceptance of the thesis.

Debrecen, 20.. . . . . ………………………………
Dr. Mónika Kéri

Investigation of waste packages, engineered barriers, and the geological environment for the final disposal of radioactive waste

Dissertation submitted in partial fulfilment of the requirements for the doctoral (PhD)
degree
in Chemistry

Written by **Vanda Papp,** certified Chemist

Prepared in the framework of the Doctoral School of Chemistry of the University of
Debrecen
(Coordination and Analytical Chemistry, program K/4)

Dissertation advisors: **Dr. Mónika Kéri**, Senior Lecturer
(University of Debrecen)

The official opponents of the dissertation:

Dr. ....
Dr. ....

The evaluation committee:
chairperson: Dr. ....
members: Dr. ....
Dr. ....
Dr. ....
Dr. ....

The date and venue of the dissertation defense: ……………… 20…

Acknowledgement

I am deeply grateful to my supervisor, *Dr. Mónika Kéri*, for her dedicated guidance in my research and her invaluable support in my professional growth. Her patience, encouragement, and friendship throughout my university years have been truly invaluable.

I extend my appreciation to the *members of the Environmental Colloids Research Group* at the Department of Physical Chemistry for their professional help and for creating a friendly atmosphere. I would like to express my sincere thanks to *Prof. Dr. István Bányai* for introducing me to the intricacies of nuclear magnetic resonance methods and for always being available to help. I am also grateful to him for the discussions about kinetic models and for his help with modeling. I am thankful to *Dr. Levente Novák* for his significant help and for being able to contact him at any time with my smallest questions. I am sincerely grateful to *Dávid Nyul* for his numerous helpful pieces of advice, which made my work easier, especially regarding the use and maintenance of the NMR relaxometer. Additionally, I thank chemical technicians *Mihály Szatmári* and *László Szabó* for their assistance in my daily laboratory work.

I also wish to express my sincere gratitude to *Dr. Róbert Janovics* for his professional assistance and support during my PhD studies, as my industrial supervisor during the KDP-2021 program. I am particularly grateful for him and *Mihály Veres* for the opportunity to conduct my doctoral research in cooperation with the Isotoptech Ltd. I would like to thank *István Papp* for his support during my research and for conducting the elemental analysis measurements. I would like to express my sincere thanks to *Zoltán Nemes* for his numerous tips and practices regarding cements and the leaching experiments. I am also grateful to him and *Andor Hajnal* for their help with the implementation of the experiments for studying the long-term effect of waste storage conditions.

I also extend my gratitude to the *Public Limited Company for Radioactive Waste Management* for their permission to study the real cementation recipe of radioactive waste and allowance to perform experiments for studying the long-term effect of the waste storage conditions in the *National Radioactive Waste Repository*. I am also thankful to *Geochem Ltd.* and *Geolog Ltd.* for providing the boreholes of Boda Claystone Formation.

I would like to thank *Prof. Dr. Gyula Tircsó*, head of the department, for providing the opportunity to conduct my doctoral research and dissertation at the Department of Physical Chemistry.

I am also grateful to our collaborating partners for their contribution in providing us with an even more comprehensive picture of the structure of cement. I am particularly grateful to *Prof. Dr. Ioan Ardelean* for his assistance in performing FFC NMR measurements and for the discussions and help with modelling the dispersion curves. I also thank *Dr. Mihai Marius Rusu* for the useful discussions and suggestions. I extend my appreciation to *Prof. Dr. Krisztina László* and *Anna Bulátkó* for their help with the low temperature nitrogen adsorption measurements. I extend my gratitude to *Dr. Attila Csík and Tamás Fodor* for taking the SEM images and performing the XRD measurements. I am sincerely thankful to *Dr. Cedric J. Gommes* for his teaching and work on modeling cementitious materials, as well as his always helpful attitude. I also wish to express my gratitude to *Dr. Léonard Alexandre* for performing mercury intrusion porosimetry measurements.

I would also like to thank my former and current students, *Tamás Péter Kertész, Vivien Nagy, Tamás Bori, Veronika Bak, Fruzsina Flóra* and *Arnold Bede* for their help with the experimental work.

I am profoundly grateful to *my family*, whose unwavering support and generosity made it possible for me to pursue my goals. Their constant love and encouragement gave me the strength to rise again even during my most challenging moments.

Finally, I wish to express my heartfelt thanks to my fiancée, *Dr. Zoltán Balogh*, for always believing in me, motivating me, and standing by my side through every challenge along the way.

The research was supported by the KDP-2021 program of the Ministry for Innovation and Technology from the source of the National Research, Development and Innovation Fund [RH/322-2/2022]. The research was also supported by the National Research, Development and Innovation Office – NKFIH [PD 135169, K 131989] and was carried out within the framework of the RHK contract. The investigation of biodegradable polymers (kinetics) was supported by the New National Excellence Program code number ÚNKP-21-3 of the Ministry of Innovation and Technology, financed by the National Research, Development and Innovation Fund.

Table of Contents

Abbreviations

ASTM	American Society for Testing and Materials
BCF	Boda Claystone Formation
BET	Brunauer- Emmett-Teller theory
BJH	Barrett, Joyner and Halenda model
BVI	Bulk Volume Irreducible
CFL	Cumulative Fraction Leached
COSY	Correlated Spectroscopy
CPMG	Carr–Purcell–Meiboom–Gill pulse sequence
DOSY	Diffusion-Ordered Spectroscopy
DR	Dubinin–Radushkevich model
EBS	Engineered barrier system
EDTA	Ethylenediaminetetraacetic acid
FFC NMR	Fast Field Cycling NMR
FFI	Free-Fluid Index
GDF	Geological disposal facility
HF-NMR	High- field Nuclear Magnetic Resonance
HLW	High- level waste
HMBC	Heteronuclear Multiple Bond Correlation
HSQC	Heteronuclear Single Quantum Coherence
IAEA	International Atomic Energy Agency
ICP- MS	Inductively coupled plasma mass spectrometry
IFL	Incremental Fraction Leached
ILW	Intermediate- level waste
ILT	Inverse Laplace Transform
IUPAC	International Union of Pure and Applied Chemistry
LF-NMR	Low- field Nuclear Magnetic Resonance
LLW	Low-level waste
MERA	Multi Exponential Relaxation Analysis
MIP	Mercury Intrusion Porosimetry
NGD	Natural geological barrier
NMR	Nuclear Magnetic Resonance
NPP	Nuclear Power Plant
NRWR	National Radioactive Waste Repository
NSDF	Near-surface disposal facility
OPC	Ordinary Portland Cement
PFG- NMR	Pulsed- Field Gradient NMR
PURAM	Public Limited Company for Radioactive Waste Management
SEM	Scanning Electron Microscopy
SFW	Spent fuel waste
VLLW	Very low-level waste

1. Introduction

The application of multi-barrier systems in radioactive waste repositories is crucial, as a single containment layer cannot ensure complete containment of radionuclides over the required long period of time.[1, 2] By the combination of engineered barriers with the natural environment, the system provides multiple layers of protection.[1, 2] From the viewpoint of the potential migration of radionuclides from the repository, the comprehensive characterization of each level of the multi-barrier system is required. The typical components of the engineered barrier system are the solidified waste form, the waste container, and other buffer or backfilling materials. One of the most crucial parts of the engineered barrier system is the solidified waste, since the solid matrix is the primary barrier to the migration of radionuclides. Cementation is one of the main solidification techniques; however, in several cases, the improvement of the cement matrix is necessary, like in the form of blended cement.[3] Regarding the applicability of such materials, the comprehensive characterization of the solid matrix and its interaction with the waste itself is essential.

In this thesis, the structure and aqueous behavior of the different levels of a multi-barrier system are investigated from a materials science perspective to estimate their long-term stability. Special attention is paid to the examination of the structure influencing effect of the components of cemented waste packages. The diversity and complexity of the examined samples necessitated a multidisciplinary approach and the combined application of various techniques, mainly low-field NMR methods with the aim of showing how these can be applied in the characterization steps of radioactive waste management.

2. Research objectives

My PhD research can be divided into three main parts:

I) characterization of binders for radioactive waste immobilization

II) investigation of the impact of real waste management conditions

III) examination of the repository's multi-barrier system.

The aim of the topic *I)* was to characterize the micro- and mesostructure of Ordinary Portland Cement, a base binding material, and to show the applicability and sensitivity of NMR relaxometry for this purpose through comparison with other techniques. The second aim was to study the effect of metakaolin and fly ash, as pozzolanic additives for the improvement of cement, with the goal of finding a favorable additive and its ratio regarding the aimed application of the cement matrix.

The aim of the topic *II)* was to study the real waste management conditions. On one hand, it meant to describe the leaching behavior, porosity, and permeability of model cemented waste packages prepared according to the actual cementing recipe of liquid radioactive waste (condensation residue). On the other hand, the long-term behavior of model waste packages was monitored under real disposal conditions in the NRWR.

The aim of the topic *III)* was to investigate the aqueous behavior of two levels of the multi-barrier system of waste repositories: *a)* the swelling properties of Na-and Ca- bentonite as engineered barriers; and *b)* the $T_{2\text{-}cutoff}$ value, characterizing the effective porosity, of Boda Claystone Formation, the geological environment suitable for the disposal of high-level waste in Hungary.

Furthermore, our aim was also to comprehensively describe the diffusivity of water within the individual levels (waste package, bentonite, geological environment) of a repository to predict the mobility of ground water.

3. Literature overview

3.1. Radioactive waste management in Hungary

"*Where half of the electricity comes from*" can be read on the website of the Paks Nuclear Power Plant (NPP). Nuclear energy may be a green alternative to energy generation providing cheap, and environmentally friendly electricity, however, during the operation and decommissioning of nuclear power plants, waste is generated that must be handled according to appropriate safety guidelines.[4] The aim of radioactive waste management is to handle radioactive waste in a way that protects both human health and the environment, now and in the future, without placing an unreasonable burden on future generations.[5] There are numerous safety standards, guidelines and requirements internationally recommended by the International Atomic Energy Agency (IAEA), as well as individual national regulations for each country, regarding radiation protection and radioactive waste management.[5, 6]

In Hungary, according to the *Act CXVI of 1996 on Atomic Energy* the provision of the storage and final disposal of radioactive waste is a state duty, thus the Hungarian Atomic Energy Authority (HAEA) appointed the Public Limited Company for Radioactive Waste Management (PURAM) to carry out this duty.[2, 7] With their cooperation the *National Policy* and the *National Programme on the management of spent fuel and radioactive waste (2016)* were developed in Hungary, based on the principles required by the *Council Directive 2011/70/Euratom of 19 July 2011 establishing a Community framework for the responsible and safe management of spent fuel and radioactive waste.*[8-10]

Radioactive waste can be defined as materials that are either radioactive or contaminated with radioactivity and are no longer suitable for further use.[4] The main sources of radioactive waste in Hungary are the operation and future decommissioning of Paks NPP, the radioactive materials and ionizing radiation used in fields of medicine, agriculture and industry as well as the radioactive materials used and produced in the research and training reactors operating for research and education purposes.[11, 12] There are two reactors for the last purpose in Hungary: Research Reactor of the Hungarian Academy of Sciences Centre for Energy Research and the Training reactor of the Institute of Nuclear Techniques of the Budapest University of Technology and Economics.[2, 9, 10]

During the operation of nuclear power plants, numerous radioactive isotopes may be produced: a) from the fission of ^{235}U (fission products e.g.: ^{90}Sr, ^{99}Tc, ^{129}I, ^{137}Cs), b) from reactions involving ^{238}U (transuranium elements e.g.: ^{239}Pu, ^{241}Pu, ^{241}Am, ^{237}Np), and c) through the activation of the structural materials and environment of the nuclear reactor (e.g.: ^{3}H, ^{14}C, ^{36}Cl, ^{54}Mn, ^{55}Fe, ^{63}Ni, ^{60}Co, ^{93}Zr, ^{94}Nb, ^{110m}Ag).[13, 14]

These isotopes are part of radioactive waste, which can be classified according to a) the state of the matter (solid or liquid), b) the activity, and c) the lifetime of the radioactive isotopes. The *National Programme of Hungary on the management of spent fuel and radioactive waste (2016)* classifies the waste according to the half- lives and radioactivity of the isotopes considering the possible heat generation during their disposal.[9, 10] If the heat generation of the waste during disposal is negligible, the waste can be classified as short or long lived LLW (low-level waste) or ILW (intermediate-level waste).[9, 10] Short lived radioactive waste has a half-life of ≤30 years, and its long-lived alpha-emitting radionuclide concentration is limited.[9, 10] In the case of HLW (high-level waste), heat generation must be considered during its disposal. Based on the *MSZ 14344-1:2004 Standard*, 2 kW/m^3 is the critical heat generation limit above which radioactive waste must be treated as heat-generating and requires special consideration in temporary storage or final disposal.[9, 10] The management of the different waste types may differ due to their various characteristics.

The general waste management steps and the life cycle of radioactive waste after generation are shown in **Figure 1**.

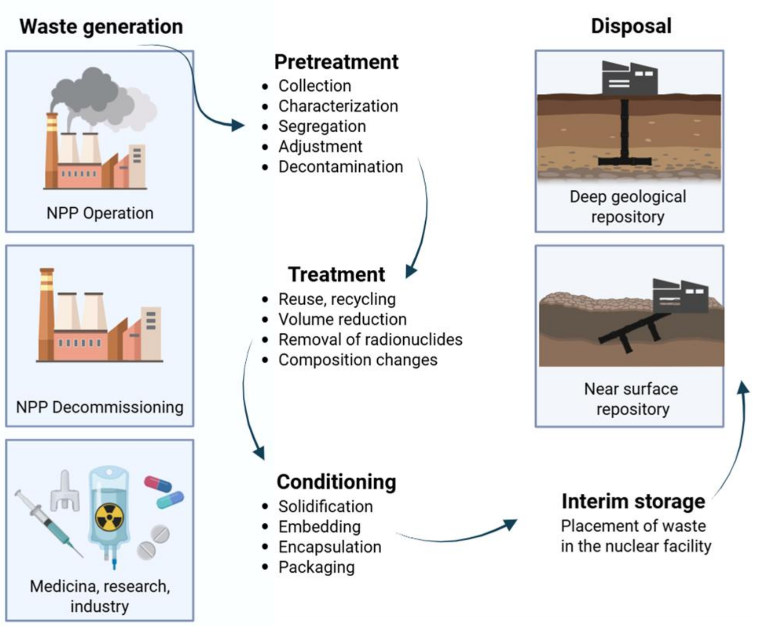

Figure 1.: Schematic representation of the life cycle of radioactive waste.

The generated waste may undergo different pretreatment steps to be categorized and separated for further processing.[12, 15] The waste is then transformed into waste packages suitable for transportation and storage/disposal through various conditioning processes, e.g.: solidification, embedding, or encapsulation.[12] Solidification of low and intermediate level liquid radioactive waste in cement, bitumen or glass are commonly used immobilization methods, while HLW might be vitrificated into glass matrix or embedded into metal matrix.[12, 15] After the temporary storage of the solidified waste packages, the final step of the radioactive waste management process is the disposal of the waste in a repository facility built according to multi- barrier concept, which ensures the long-term safe isolation of the waste from the biosphere.[12, 16-18]

In Hungary according to the *National Programme*, the largest amount of radioactive waste is generated during the operation of the four VVER440/213-type reactor units of the Paks NPP, where both solid and liquid waste are produced.[9, 10] The main sources of solid LLW and ILW waste are contaminated or activated protective garments, equipment, tools, pipelines, thermal insulation, etc. contaminated over the operation or maintenance of the NPP.[9, 10] These are collected selectively (e.g.: compactable, non-compactable) and stored in bags or steel drums (V~200 l) in the interim storage at the site of the NPP. [9, 10] Liquid radioactive waste is generated mainly during the treatment of water in the primary circuit, and the decontamination of rooms and equipment being listed in **Figure 2**. In small quantities, contaminated oil waste may generate.[9, 10] The aqueous based liquid waste of the primary circuit is collected in a special sewer system and is treated by filtration, sedimentation, and chemicals.[9, 10]

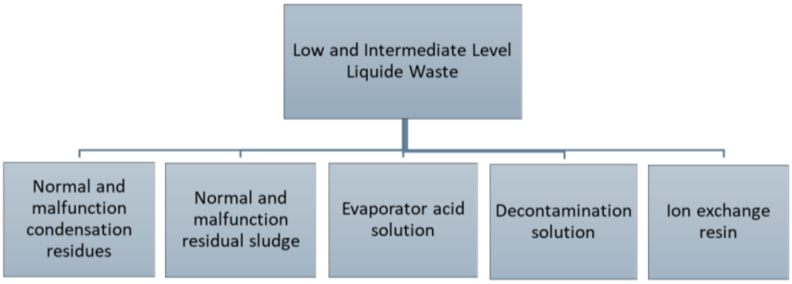

Figure 2.: Low and intermediate level liquid waste types generated in NPPs.

A decisive proportion of aqueous liquid waste is treated by liquid waste treatment technology which reduces its volume drastically resulting in evaporation residue which may be discharged after inspection.[9, 10] Liquid waste that cannot be treated with this technology (e.g.: operational condensation residue, sludge, decontamination solution, ion exchange resin) are solidified by cementation in steel drums. Relatively small amounts of HLW are generated annually in Paks NPP, which are interim stored in pipe wells.[9, 10] In 2003, there was an operational incident in the second unit of Paks

NPP, where a large amount of liquid waste was polluted with alpha radiation isotopes causing the production of malfunction waste types as shown in **Figure 2**. These were collected and stored separately.[2, 9, 10]

There are three facilities for the disposal/ interim storage of radioactive waste in Hungary coordinated by PURAM. These are the Radioactive Waste Treatment and Disposal Facility (RWDTF, near-surface repository for LLW, ILW, Püspökszilágyi), National Radioactive Waste Repository (NRWR, underground repository in a depth of 200-250 m for LLW, ILW, Bátaapáti), Spent Fuel Interim Storage Facility (SFISF for HLW, Paks).[2, 9, 10, 19] The LLW and ILW waste generated during the operation of Paks NPP is transported to the National Radioactive Waste Repository, where the solidified waste is stored and disposed of.[2, 9, 10, 19]

A deep geological repository for the disposal of high activity and long-lived radioactive waste and spent fuel will also be established, the site of which is under selection. In 2000, PURAM set up a formation-qualifying research program (screening) covering the entire territory of the country.[9, 10, 19] Based on the national screening, the Boda Claystone Formation (BCF) was found to be the most promising option.[20-23]

To ensure the long-term safety of the radioactive waste disposal facilities, the application of multiple engineered barriers and an appropriately chosen natural environment is required, which contain and isolate the waste from the biosphere.[1, 2] Regarding the multiple engineered barriers system, the individual components of the barrier system itself should retrain the migration of radionuclides, thus the possible damage of one barrier does not endanger the performance of the disposal system.[1, 2] The multiple barrier system contains at least six levels: *I)* the solidified waste form, *II)* the corrosion resistant metallic container/ drum, *III)* the cement/ concrete filling between the containers, *IV)* the concrete wall of the vaults, *V)* backfill materials (e.g. clays) and VI) the host rock of the repository.[2, 15, 16] The last one can be considered as a natural geological barrier (NGB), while the other levels are the engineered barrier system (EBS).[16]

The host rock (NGB) of the NRWR is the Mórágy granite formation, while the engineered barrier system of the repository consists of the following segments.[19, 24] The waste packages are disposed according to a new storage concept: four of the conditioned radioactive waste containing drums are placed in a thin-walled reinforced steel container and the space between the drums is filled with cemented liquid radioactive waste resulting in compact waste packages.[19, 25] These containers are placed in a reinforced concrete pit installed in a storage chamber of the facility, and the space between the containers is filled with inactive cement.[19] The chamber is filled in sections, and each section is separated by a reinforced concrete wall.[19] The space between the reinforced concrete containers and the cut wall within the storage chamber is filled with backfilling materials (concrete mixed with granolith).[9, 10] According to the closure concept of the NRWR, the servicing and approach cut system will also be filled with the same backfilling materials and at certain places sectionalizing plugs made from concrete and bentonite will be integrated.[9, 10, 24]

3.2. Cement in radioactive waste management

As can be seen from the previous chapter, cement plays a pivotal role in most repository design concepts.[26] It is part of the engineered barrier system and is an immobilization matrix for LLV and ILW. It can sorb radionuclides, inhibit steel corrosion by contributing to an alkaline near-field, influence microbial activity, and may inhibit the transport of radionuclides in the repository.[26] Immobilization of radioactive waste means the conversion of raw waste containing mobile contaminants into a solid and stable waste form.[27] Cementation is a widely used immobilization method for low and intermediate level waste.[27, 28]

There are numerous advantages of immobilization of radioactive waste by cementation:

- Cement is a cheap and available solid material, which can be handled easily at ambient temperatures.[27, 29]
- It can function as a diffusion barrier, can sorb radionuclides, and ensure the low solubility of several compounds due to its alkalinity.[27]
- It is suitable for the solidification of various waste types (e.g.: dry solids, sludges, condensation residue).[27]
- The cemented waste forms are stable and can be handled easily, while also the cementation method can be modified and improved for various waste types (e.g.: by the addition of pozzolans).[27, 29]

Hydraulic cement is an inorganic material, which is set and hardened upon interacting with water through hydration reactions resulting in a solid water-resistant product.[26-28, 30] Ordinary Portland cement (OPC) is one of the most common types of cement consisting of several anhydrous minerals.[28] This type of cement is produced by heating limestone with clay to about 1450 °C in a kiln; and the resulting clinker phases are then grounded and mixed with a small amount of gypsum (~2 %).[28] OPC consists of four main anhydrous clinker phases: 50–70 % tricalcium silicate (alite, $C_3S= 3CaO{\cdot}SiO_2$), 20–30 % dicalcium silicate (belite, $C_2S= 2CaO{\cdot}SiO_2$), 5–12 % tricalcium aluminate ($C_3A= 3CaO{\cdot}Al_2O_3$) and 5–12 % tetracalcium ferroaluminate ($C_4AF= 4CaO{\cdot}Al_2O_3{\cdot}Fe_2O_3$).[28, 31] The first two clinker phases form the silicate, while the last two mean the aluminous phases of Portland cement.[31] Gypsum ($C\$H_2=$

$CaSO_4 \cdot 2H_2O$) is added to the cement to control the rapid hydration of the C_3A phase.[31] There are two mains Portland cement types: white and grey cement. In grey cement the CaO ratio is lower (60-65%) compared to white cement (~70%), while its Fe_2O_3 content is higher (1%<).[31]

Among the clinker phases, the tricalcium aluminate (C_3A) and tricalcium silicate (C_3S) phases are the most important in terms of cement hydration.[31] The first is the most reactive phase of cement, which plays an important role during early hydration.[30] The hydration of C_3A, in the presence of sulfates (gypsum, $C\$H_2$) leads to the precipitation of ettringite (Aft, $C_6A\$_3H_{32}$), which can further develop to monosulfoaluminate (Afm, $C_4A\$H_{12}$), when the sulfate depletion point is reached:[30]

$$C_3A + 3C\$H_2 + 26H \rightarrow C_6A\$_3H_{32} \qquad (1)$$

$$2C_3A + C_6A\$_3H_{32} + 4\mathrm{H} \rightarrow 3C_4A\$H_{12} \qquad (2)$$

Even though C_3A is very reactive, the hydration process of Portland cement is mostly dominated by C_3S, the main clinker phase. As the tricalcium silicate reacts with water, amorphous CSH gel and crystalline portlandite (CH) precipitate:[30]

$$C_3S + (3 - x - n)H_2O \rightarrow C_x - S - H_n + (3 - x)CH \qquad (3)$$

where n represents the water to silica ratio in CSH and the CaO/ SiO_2 ratio alter between 1.2- 2.1.[30] The hydration of C_3S consists of 5 well-known stages, which will be discussed in more detail later in the *Results section*.

As a result of the hydration reaction various hydrate phases form, among which the crystalline portlandite (20-25%, CH= $Ca(OH)_2$) and amorphous calcium silicate hydrate (50-70%, CSH= $1.7CaO \cdot SiO_2 \cdot nH_2O$) are the major hydrate phases. In addition to these, calcium aluminoferrite trisulphate (Aft, $Ca_6(Al,Fe)_2(SO_4)_3(OH)_{12} \cdot 26H_2O$), calcium aluminoferrite monosulfate (Afm, $Ca_4(Al,Fe)_2(SO_4)(OH)_{12} \cdot 6H_2O$), hydrogarnet ($3CaO \cdot Al_2O_3 \cdot 6H_2O$) and hydrotalcite ($Mg_6Al_2(CO_3)\,(OH)_{16} \cdot 4(H_2O)$ are formed as minor phases.[28, 30] Besides these, calcite ($CaCO_3$) may form due to the carbonation of cement.

Cement acts as a chemical and physical barrier for the radionuclides since during cement hydration, hydrate phases suitable for the sorption of dissolved radionuclides and a porous structure that prevents their movement are formed.[3, 32, 33] The hydrate phases of the hardened cement provide various options for the sorption of dissolved radionuclides including surface/ bulk sorption, incorporation or solid solution formation and precipitation.[28, 33] The main hydrate phase, the CSH gel, has a high complex amorphous structure with a large specific surface area, which provides a high sorption capacity and allows the non-specific sorption of both cations and anions depending on the Ca/Si ratio of the gel.[28] Crystalline portlandite can strongly sorb metal ions (e.g.: Ni), and anions (e.g.: Cl^-, I^-) due to its layered structure and the numerous OH functional groups on its surface.[28] Aft phases, like ettringite, have an open structure with negatively charged surface presenting several possibilities for ion exchange/ substitution and adsorption processes (e.g.: for Sr^{2+}, Ni^{2+}, Cl^-, IO_3^-).[28] Afm phases, like monosulfoaluminate, allow ion exchange/ substitution processes and may sorb heavy di-, trivalent metal ions and halogens due to its irregular layered structure and unbalanced layer charge.[28] Afm phases have potential to sorb Cl^- by forming Friedel's salt.[28] In hydrogarnet the sorption may happen though ion substitution (e.g.: Al^{3+}– Cr^{3+}), while in the layered structure of hydrotalcite the incorporation of di- and trivalent ions may take place (e.g.: Ni^{2+}, Co^{2+}, Cr^{3+}, Cl^-).[28]

The precipitation of the hydrate phases results in the formation of a heterogeneous porous solid structure with pores in a large size range (from a few tenths of nanometers to micrometers). The CSH gel, as the main component of the hardened cement, determines its mesostructure. There are numerous models describing the mesoscale structure of the CSH gel, among which the most widespread ones are the colloidal model by Jennings and the continuous model by Feldman and Sereda.[34-36] The colloid model (CM-II) suggests that the CSH gel builds from approximately 4 - 5 nm sized globules, that may aggregate into high- or low- density phases called inner and outer CSH respectively.[34, 36] These globules are not compact but have a layer-like structure, which consists of defective CSH sheets like tobermorite and jennite.[34, 36] These sheets in the globules surround the smaller (<1 nm) intra- globular pores, while between the globules gel pores with dimensions of 1 - 12 nm are present.[34, 36] The continuous model describes the CSH gel as a disordered, continuous assembly of highly defective CSH sheets.[35, 36] These sheets are similar to the ones in the colloid model, but not only extend to the globules, but to the whole gel phase, having a crumpled nature and enclosing pores of different sizes.[35, 36] Beside the pores of the hydrate phase, larger capillary and air pores are also present in the cement structure.[35]

In the hardened cement structure water can be present in chemically (non-evaporable), and physically bound states, as well as can fill larger pores according to the Powers' model.[37, 38]

3.3. Characterization of cementitious waste forms

Modelling the potential migration of radionuclides from the repository is a complicated task, which requires the comprehensive characterization of each level of the multi-barrier system. During the characterization of solidified waste forms, it is essential to determine that: *I*) the hazardous radioactive constituents have been immobilized, *II*) the radionuclide content is known with sufficient accuracy and *III*) the waste forms meet all requirements regarding mechanical strength, leachability, durability and physical integrity.[15, 39]

The leaching resistance (radionuclide retention capacity) of cement is routinely tested by accelerated leaching methods, which allow the determination of the leached fractions of the radionuclides and their effective diffusion coefficients within the cement matrix.[40-46] Pore size and its distribution are the main basic indicators of porous materials, which highly influence the permeability, permeation rate, and retention performance of the material.[47] Although, the structural characterization of the cement matrix is somewhat complicated, due to the large size range of the pores and the non-evaporable water content of the CSH gel, the commonly used structural examination techniques (e.g. gas adsorption, mercury intrusion porosimetry, scanning electron microscopy) can generally provide information about the different parts of the heterogeneous structure.

A well-established method of pore size and volume determination is the mercury intrusion porosimetry (MIP), which can be used to detect pores in the size range of 3 nm - 1000 µm.[48-51] The basis of the method is the pressure-dependent intrusion of a non-wetting liquid, mercury, into the porous system.[48-51] The relationship between the pressure that forces the intrusion (P) and the pore size (d), which is described by the Washburn equation, with the assumptions of connected, cylindrical pores:

$$Pd = -4\gamma cos\theta \qquad (4)$$

where γ is the surface tension of mercury ($\gamma \sim 480$ mN/m) and θ is the contact angle between the pore walls and mercury ($\theta \sim 130°$).[48-51]

Gas adsorption is one of the most popular methods for determining the pore size distribution (in the range of $d \sim$ 2-50 nm or even lower) of micro- and mesoporous materials with large specific surface area.[47] The basis of this method is capillary condensation: first, the multilayer physisorption of gas on the pore wall occurs, then at high relative pressures, capillary condensation takes place.[47, 52] During the measurement, the quantity of the adsorbed gas is recorded as a function of the relative pressure of the gas, resulting in the adsorption and desorption branches of the isotherm.[52] Due to the distinct mechanism of the adsorption- desorption processes, a hysteresis may occur between the branches of the isotherm.[47, 52] The shape of the isotherm depends on the properties of the interacting substances as well as the adsorbent-adsorbate interactions and based on this the isotherms can be classified into six groups according to the IUPAC classification.[52-54] Adsorption models (e.g.: Langmuir- model, a Brunauer–Emmett–Teller (BET) model, Dubinin–Radushkevich- (DR) model, Barrett, Joyner and Halenda (BJH) model) can be used to obtain information about the size of the surface, the size and size distribution or volume of the pores.[52, 53, 55] The most used gas for this method is nitrogen.[47, 52]

Scanning Electron Microscopy (SEM) is a key technique for the microstructural characterization of porous materials in micro- nanometer size range, allowing the direct observation of the pore structure and the morphology of the sample.[56, 57] SEM uses a high energy electron beam, which reaches the sample causing the generation of backscattered electrons (BSE), secondary electrons (SE), and X-rays, among others.[56, 57] According to the detected signal different information about the sample could be observed: BSE gives information about the composition of the sample, while SE originates from the near-surface region of the sample and gives insight into the topography and morphology of the sample.[56, 57]

Most of the mentioned techniques provide information about the porous solid under vacuum conditions, however, from the viewpoint of the application of cementitious materials and other parts of the multiple barrier system, it is essential to characterize them in aqueous medium. Liquid-state nuclear magnetic resonance (NMR) methods may be used for this purpose, which can provide information about *I)* the pore structure in the whole micro-macro size range in the wet and dry samples[58-62], *II)* the connectivity of the pores[63-65] and *III)* the movement of water[60, 66, 67]within the material.

3.4. Nuclear Magnetic Resonance

3.4.1. Fundamentals of NMR

The basis of nuclear magnetic resonance methods is that the degenerate energy levels of atomic nuclei with a magnetic dipole moment (e.g.: ^{1}H, ^{2}H, ^{13}C, ^{15}N) split in magnetic field (Zeeman effect) and can be excited by electromagnetic radiation in the radio frequency range.[68-70] Generally, a large number of spins are present in NMR samples, and the vector sum of the individual nucleus results in the macroscopic magnetization (M) of the sample.[70] In static magnetic field the macroscopic magnetization aligns with B_0, however upon disturbance it can tilt from the equilibrium state into the transverse (x-y) plane and precess about B_0 with Larmor frequency (ω_L):

$$\omega_L = \gamma B_0 \qquad (5)$$

where γ is the gyromagnetic ratio of the nuclei ($\gamma \sim 2\pi \times 42.57$ MHz/T for ^{1}H).[71]

The macroscopic magnetization can be disturbed and rotated away from the equilibrium state (z plane) by a magnetic field (B_1) perpendicular to B_0 oscillating in resonance with the precession frequency (rf pulse).[70] As the precession of macroscopic magnetization is a rotational motion and the rf pulse is a rotating wave, it is conventional to study the change of the macroscopic magnetization in a rotating coordinate frame as **Figure 3** shows.[70]

If B_1 is turned on, the macroscopic magnetization rotates about B_1 in the x-y plane with a frequency (ω_1), and by applying B_1 in a pulsed fashion for a defined time interval (t_p), the magnetization can be rotated in the rotating coordinate frame around the different axes.[70]

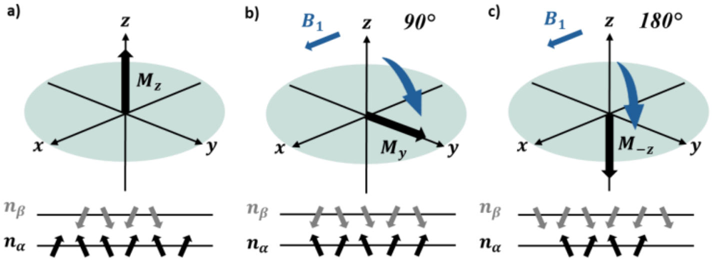

Figure 3.: In a rotating coordinate frame, the macroscopic magnetization (M) of a spin system **a)** exposed to static magnetic field (B_0), excited **b)** with 90° rf pulses and **c)** 180° rf pulses (B_1). The figures below show the population of the two spin states (n_α- higher energy state, n_β -lower energy state) of the spin ½ nucleus.

The most commonly used pulses are the 90° and 180° rf pulses; the former one rotates the magnetization to the y axis and converts M_z to M_y and balances out the population difference of the spin states (see in **Figure 3b**).[68, 70] While the later one inverts the magnetization to the $-z$ axis and swaps the population of the two spin states of the spin ½ nucleus (see in **Figure 3c**).[68, 70] After the excitation, the magnetization can return to its equilibrium state through two main relaxation processes as shown in **Figure 4**.

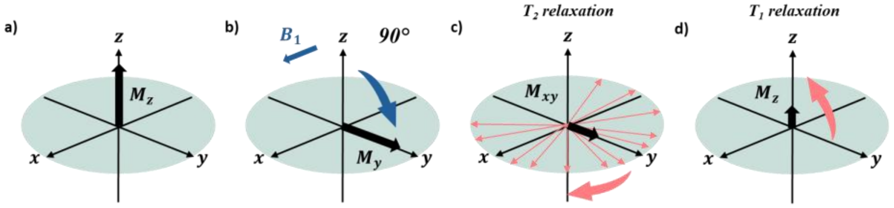

Figure 4.: In a rotating coordinate frame, the macroscopic magnetization (M) of a spin system **a)** exposed to static magnetic field and **b)** excited with 90° rf pulse (B_1). Return of M to the equilibrium after excitation through **c)** transverse and **e)** longitudinal relaxation.

- *Transverse or spin-spin relaxation* is an entropic relaxation process, which involves the dephasing of the coherent macroscopic magnetization in the x-y plane due to local magnetic disturbances owed to the quality of the magnet and the interactions (e.g.: dipole- dipole interaction) within the spin system (see in **Figure 4c**).[70-72] The phase coherence of M_y is lost in time (T_2 transverse relaxation time). Transverse magnetization conventionally decays exponentially: $M_{xy}(t) = M_z(0)exp^{-t/T_2}$.[70, 71]

- *Longitudinal or spin-lattice relaxation* is an enthalpic relaxation process, which involves an energy exchange between the spin system creating the macroscopic magnetization (*M*) and the lattice that does not participate in it.[68, 70] The T_1 longitudinal relaxation time is the time required for the spin system to recover the equilibrium population difference between the upper and lower spin states after the excitation (see in **Figure 4d**).[72] Longitudinal magnetization decays as: $M_z(t) = M_z(0)(1 - exp^{-t/T_1})$.[70]

These relaxation processes are sensitive to molecular motions which can cause fluctuations in local magnetic fields, such as the rotational diffusion of the molecules.[68, 73]The later motion can be characterized by the rotational correlation time (τ_c), which is the time required for the molecules to rotate 1 radian (~60°).[68] Short τ_c means rapid molecular motion. T_2 transverse relaxation time shows a steady decrease with increasing τ_c, meaning that the rapidly (freely) moving molecules relax slower.[74] In contrast, the T_1 longitudinal relaxation time shows a minimum (hyperbolic shape) with increasing τ_c, meaning that both the slow and rapidly moving molecules may have long T_1.[68, 71, 73, 74] This keys the difference, why it is better to characterize the porous structure of cement by measuring the T_2 transverse relaxation times.[71]

Other interactions can also vary the magnetic field, causing the enhanced dephasing and loss of the macroscopic magnetization (NMR signal), such as the magnet inhomogeneity, magnetic susceptibility differences within the sample and the electron- nuclear interactions.[71, 72] This latter one is especially relevant and strong in the case of cement, where dipolar interaction between the water protons and the unpaired electrons of paramagnetic impurities, like Fe^{3+}, can enhance the relaxation process.[71]

3.4.2. Characterization of the porous structure by NMR

The porous structure of materials can be indirectly characterized through the pore-filling liquid by NMR. The mentioned relaxation times are particularly useful parameters for the characterization of porous materials, since they are strongly dependent on the pore size, the distribution of the pore sizes, as well as the water content and the type of the material.[72] The relaxation times of fluids in porous media differ significantly from that in bulk fluids as expected from dependence of the T_1 and

T_2 relaxation times on the correlation time of molecular motions (τ_c).[75] Thus, water types with different 'mobility' can be distinguished based on their relaxation time constants.[76, 77] The relation between the T_1 and T_2 relaxation times and the pore sizes (surface to volume ratio, S/V) is defined in a two-site model with the assumption of fast-exchange between the sites.[72, 78-81] According to this model, the liquid can be present as a liquid layer on the surface of the solid or in the bulk phase, and rapid diffusion occurs between these liquid domains.[72, 78, 79] Therefore, the total relaxation process of the system can be described by the volume-weighted average of the relaxation rates ($1/T_2$) of the liquid domains with different mobility:

$$\frac{1}{T_2} = \frac{V_s}{V}\frac{1}{T_{2s}} + \frac{V_{bulk}}{V}\frac{1}{T_{2bulk}} \qquad (6)$$

where V_s and V_{bulk} are the volumes of the surface and the bulk liquid respectively and V is the total volume of the liquid. T_{2bulk} and T_{2s} are the characteristic relaxation time constants of water molecules in the bulk-like and surface regions, respectively, and T_2 is the observed apparent transverse relaxation time.[81] The surface to volume ratio of the pores can be calculated knowing the surface relaxivity (ξ) of the material as follows:

$$\frac{1}{T_2} = \xi\frac{S_p}{V_p} + \frac{1}{T_{2bulk}} \qquad (7)$$

where S_p is the surface and V_p is the volume of the pores.[72, 79, 80, 82, 83] Surface relaxivity reflects the strengths of the interactions between the pore surfaces and the mobile nuclear spins.[72, 84] When the geometry of the pores is known, S_p/V_p can be replaced by the pore geometry (e.g.: $3/r$ for spherical pores) and the pore size (r) can be calculated.[71, 72, 77]

The T_2 relaxation time of fluids confined in porous media may be measured using 90°- t_{echo}- 180°- t_{echo}- acquire spin echo sequences, such as the CPMG (Carr–Purcell–Meiboom–Gill) pulse sequence, which uses a train of 180° refocusing pulses after the initial 90° pulse.[71, 72, 79] It is advisable to keep the echo time (t_{echo}) between pulses short to avoid complications due to diffusion in the presence of local magnetic field gradients.[72] The T_1 relaxation time of liquids may be determined by using the inversion-recovery (IR) pulse sequence containing 180°- t_{inv}- 90°-acquire, where t_{inv} is a waiting time.[71, 72]

^{1}H NMR relaxometry has been greatly used for monitoring the hydration process and microstructure evolution and for characterizing the porous structure of cement since the late 20th century.[58, 61, 71, 74, 85-88] Blinc et al. were the first, who monitored the evolution of T_1 and T_2 of confined H_2O and D_2O over the hydration of cement and C_3S pastes.[89] Halperin et al. were the first who applied the above-mentioned fast exchange model in cement paste for the conversion of T_2 to size.[79] Several water domains can be distinguished in cement by their T_2 relaxation time constants, which are in good agreement with the mentioned water types in Section 3.2.[58, 88, 90-92]

With the combination of the mentioned two pulse sequences (CPMG, IR), the correlation between the two relaxation time constants (T_1 and T_2) can be studied, which addition to the pore structure characteristics, might shed light on the exchange processes of water molecules between the different pore types.[63-65, 93, 94] McDonald et al.[59, 64, 65] and Cadar et al.[63] both performed T_1–T_2 correlation experiments on cements and could distinguish the different water types within the solid material. McDonalds et al. found that the diagonal feature of the signals shifted to $T_1 = 4T_2$.[59]

Fast Field Cycling NMR relaxometry (FFC NMR) is another type of NMR relaxometry, where the longitudinal relaxation time (T_1) of the confined liquid is measured at various Larmor frequencies, therefore it is sensitive to a wide range of molecular mobilities and can provide useful information about the nano-scale dynamics of confined liquid molecules.[62, 95, 96] FFC NMR measurements on cementitious materials have been performed by Korb et al. [95, 97]as well as by Ardelean et al.[62, 96, 98, 99] Badea et al. followed the early hydration of cement pastes affected by silica fume and the curing temperature and could successfully apply the theory of Korb et al, detailed below in the *Results section.*[97] for the evaluation of the observed T_1 dispersion curves.[98, 99]

NMR cryoporometry is a non-invasive method that allows us to examine the size and geometry of pores.[100-102] This is a freezing-based method, in which the proton signal of the liquid phase is detected. The amount of the molten phase, and therefore the intensity of the signal, gradually changes during freezing and thawing. The correlation between the size of the confinement (r_p) and the freezing–melting point depression ($\Delta T_{m/f}$) can be described by the modified Gibbs-Thomson equation:

$$\Delta T_{m/f} = T_{m/f} - T_0 = -\frac{nK_c}{r_p} \qquad (8)$$

where T_0 is the phase transition temperature of the bulk liquid, $T_{m/f}$ is the melting and freezing point of the liquid in the pores, n is a factor correlated to the pore geometry and K_c is the cryoporometric constant of the liquid.[100-102]

Cryoporometry was successfully applied for cement-based mortar by Valckenborg et al., who revealed three different pore types.[103]

3.4.3. Diffusion of water in the porous structure

NMR diffusometry can be used to determine the self-diffusion (Brownian motion) coefficient of water, the value of which significantly decreases when molecules are confined within a porous system, and their movement is restricted.[104-108] The diffusion coefficient can most often be measured using a stimulated spin echo sequence with gradient pulses (PFG-NMR).[105, 109] The sample is magnetized in the longitudinal (z) plane for most of the measurement time, relaxing according to T_1, which in the case of samples with fast transverse relaxation time does not lead to signal loss due to relaxation. The diffusion coefficient (D_{obs}) can be determined from the measured signal intensity using the following equation:

$$I = I_0\, exp(-D_{obs}\gamma^2\delta^2G^2(\Delta - \delta/3)) \qquad (9)$$

where I_0 is the initial intensity, γ is the gyromagnetic ratio of the given nucleus, Δ is the diffusion time, while δ is the duration of the gradient pulse.[105, 109] The dependence of D_{obs} on Δ can provide information about the pore size in the 5-100 μm range and the permeability of the closed space that limits the diffusion processes.[105, 106] However, in several cases, like in grey cements, these methods are not suitable for studying the diffusion process, due to the Fe^{3+} content of cement, which accelerates both the T_1 and T_2 relaxation of water. The so-called H_2O–D_2O exchange diffusion technique, which Fleury et al. applied to cement, concrete, and mortar samples, is suitable for examining such systems.[66, 67]

4. Experimental methods

4.1. Materials

For the cementitious samples, grey Portland cement (CEM I 42.5 N, $d_{particle}$~ 5–30 µm) was purchased from Duna-Dráva Cement Ltd. Metakaolin (KM60, $d_{particle}$< 63 µm) consisted of 50-55% SiO_2, min. 40% Al_2O_3, max. 1.45% Fe_2O_3, 0.05-0.5 % CaO, 0.20-0.45 % MgO and max. 1.5% K_2O+Na_2O and was purchased from Keramost Plc. Fly ash (Microsit®10, $d_{particle}$~ 10 µm) was a PFA type anthracite ash (class F fly ash) with a composition of 52% SiO_2, 25% Al_2O_3, 7% Fe_2O_3, 0.5 % CaO, which was purchased from NEWCHEM GmbH.

The dry powders were mixed on one hand with deionized water (MilliQ), and on the other hand with a model solution prepared from isotope analogue model ions and complexing agents. Boric acid (H_3BO_3, a.r.), sodium hydroxide (NaOH, a.r.), potassium hydroxide (KOH, a.r.), potassium iodide (KI, a.r.), potassium chloride (KCl, a.r.), oxalic acid dihydrate ($C_2H_2O_4{\cdot}2H_2O$, a.r.), ethylenediaminetetraacetic acid disodium salt dihydrate ($Na_2EDTA{\cdot}2H_2O$, Puriss) were purchased from Molar. Nitric acid (HNO_3, 65 (m/m)%, a.r.) and citric acid monohydrate ($C_6H_8O_7{\cdot}H_2O$, Ph.Eur.) were purchased from VWR. Neodymium (III) nitrate hexahydrate ($Nd(NO_3)_3{\cdot}6H_2O$, 99.9%), cesium nitrate ($CsNO_3$, 99.9%) and ammonium perrhenate (NH_4ReO_4, 99.9%) were purchased from Sigma-Aldich. Nickel acetate ($Ni(CH_3COO)_2{\cdot}4H_2O$, at.) was purchased from Reanal. For the sample preparation, PVC tubes (d=0.6 cm) were used.

Ca-bentonite (Istenmezeje, Hungary, $d_{particle}$< 20 µm) consisted of 3.3% SiO_2, 18.7% Al_2O_3, 3% Fe_2O_3, 1.5% CaO and 3.5% MgO. Na- bentonite was prepared from Ca-bentonite by cation exchange in the Lajos Imre Isotope Laboratory, University of Debrecen.

The boreholes of Boda Claystone Formation (BCF) were received from Geochem Ltd., Geolog Ltd. and were taken from two depths, 665.45 m (BCF1) and 746.06 m (BCF2). The diameter of the borehole was ~6 cm, and the samples were packed into foil. To simulate the pore liquid of BCF samples, a model solution was prepared containing calcium chloride dihydrate ($CaCl_2{\cdot}2H_2O$, ≥99%), magnesium sulfate heptahydrate ($MgSO_4{\cdot}7H_2O$), potassium sulfate (K_2SO_4), sodium bicarbonate ($NaHCO_3$), disodium hydrogen phosphate dodecahydrate ($Na_2HPO_4{\cdot}12H_2O$) and sulfuric acid (ACS reagent, 95.0-98.0%) purchased from Sigma Aldrich and Merck.

For the H_2O- D_2O exchange diffusion measurements, heavy water (D_2O, 99.96 atom % D) and sodium hydroxide (NaOH, Reag. Ph. Eur.) were purchased from VWR.

For the ICP-MS measurements, nitric acid (HNO_3, 67%, NORMATOM®) was purchased from VWR, internal indium ICP-MS standard (200 µg/l In) was purchased from VWR. For the filtration of the leachates the 0.45 µm cellulose acetate filter membrane was purchased from Kipszer- Paraplan.

4.2. Sample preparation

Pure Portland cement samples were prepared by mixing Portland cement with deionized water in 0.4- 0.6 water-cement (*w/c*) ratios. After homogenization, the cement paste was poured into cylindrical PVC molds (*h*~ 2 cm, *d*= 0.6 cm) and cured for 28 days at 298±0.1 K, 100% RH (a beaker of water was placed next to the samples). The hardened cement samples were generally studied in cylindrical sample form by NMR in dry or water saturated states. For the dry tests, the samples were dried in an oven at 353 K for 7 days.

To study the effect of pozzolans, two sample series were prepared using Portland cement mixed with metakaolin and fly ash separately in 0, 10, 20 and 30 m/m% mass ratios (detailed in **Table 1**). The water-solid (*w/s*) ratio was 0.5 for each sample. The curing process of the cement composite paste is the same as described for pure Portland cement. To follow the hydration process of the cement composites, the samples were prepared in-situ before the measurements.

Table 1.: Composition and name of the prepared cement composites.

	Cement	**Mc10**	**Mc20**	**Mc30**	**Fc10**	**Fc20**	**Fc30**
Cement (m/m%)	100	90	80	70	90	80	70
Metakaolin (m/m%)	-	10	20	30	-	-	-
Fly ash (m/m%)	-	-	-	-	10	20	30
Water/solid ratio	0.5						

For studying the effect of the complexing agent content of model cemented waste packages, samples were prepared based on the recipe for the cementation of low- and intermediate-level waste (e.g.: condensation residues) at Paks NPP in Hungary, which was received with the permission of PURAM. Accordingly, 80 m/m% Portland cement and 20 m/m% metakaolin were mixed with a model solution, containing H_3BO_3, NaOH, KOH and HNO_3, in *w/s*=0.5 ratio. Radioactive isotopes (^{135}Cs, ^{59}Ni, ^{129}I, ^{36}Cl) were replaced by their inactive forms. In the case of non-replaceable isotopes, elements with similar chemical properties were used: technetium (^{99}Tc) was replaced with rhenium, while americium (^{241}Am) was modeled with neodymium. The composition of the model solution and the applied model ion concentrations are shown in **Table 2**. Complexing agents in different concentrations (0 – 20 g/l) were added to the solution in 1:1:1 mass ratio: citric acid, oxalic acid, Na_2-EDTA. The homogenized cement paste was cured as detailed above.

Samples for testing the long-term effect of the waste storage conditions were prepared in the same way in two sizes: small (*h*~ 2 cm, *d*= 0.6 cm) and large ones (*h*~ 2.8 cm, *d*= 2.8 cm).

Table 2.: Composition of the model solution used for the model waste packages.

Components		**Concentration (g/l)**
Model solution	H_3BO_3	190.02
	NaOH	131.22
	KOH	24.30
	HNO_3	31.5
Model ions	$Ni(CH_3COO)_2 \cdot 4\ H_2O$	1.3625
	$Nd(NO_3)_3 \cdot 6\ H_2O$	0.9802
	$CsNO_3$	0.4777
	KI	0.4204
	NH_4ReO_4	0.0519
	KCl	6.7547

(Source: PURAM)

The hardened cementitious samples were generally studied in cylindrical sample form by NMR in a water saturated state. For the SEM, low temperature nitrogen adsorption, MIP measurement, and for comparative NMR measurements, the cylindrical samples were crushed and powdered.

Ca- and Na-bentonite were used without any pretreatment, as received. For the NMR measurements, deionized water was added to the powdered samples.

From the two borehole samples of Boda Claystone Formation (BCF) cylinders (d ~ 7 mm) were drilled out using a rose-drill under water cooling. The core samples (BCF1 and BCF2) were examined in cylindrical monolith, powdered, and crushed forms, among which the monolith forms were the most promising. To mimic the pore liquid of BCF, a model solution was prepared according to **Table 3**. The pH of the solution was adjusted with sulfuric acid to the desired value of 8.1, which contributed to the sulfate concentration. For the dry tests, the samples were dried in air for several days and then in an oven at 378 K for 2 days. For the measurements in saturated state, the samples were immersed and soaked in the prepared model solution for 3 days, then vacuum was used to reach full saturation.

Table 3.: Composition of the model solution used to saturate the tested BAF samples.

Components	HCO_3^-	CO_3^{2-}	SO_4^{2-}	Cl^-	PO_4^{3-}	Ca^{2+}	K^+	Mg^{2+}	Na^+
Concentration (mg/dm^3)	717	<3	150	14	0.13	8.3	4.57	2.9	254

(Source: PURAM)

4.3. Structural characterization

4.3.1. 1D NMR Relaxometry

During the 1D NMR relaxometry measurements, the T_2 relaxation decays of water confined in the porous materials were recorded on a 20 MHz NMR instrument (Minispec mq20, Bruker, Germany) at room temperature (298 K) using the CPMG (Carr-Purcell-Meiboom-Gill) pulse sequence.[110] The specimens were placed into 10 mm wide glass NMR tubes. The 90° pulse length was optimized for the samples and varied between 1.8- 2.2 μs with 3dB pulse attenuation. The echo time was set to the lowest possible value of our device (t_{echo}= 0.08 ms) for each experiment to detect as much as possible of the fast-relaxing components. The number of echoes (n_{echo}) were adjusted to reach the complete attenuation of the relaxation processes. The relaxation delay (R_d) was optimized for the samples, according to the T_1 relaxation times determined using the inversion–recovery method, to detect all water domains in the samples. The receiver gain (*rg*) and the number of scans (*ns*) were adjusted to the samples to maximize the signal-noise ratio. These values are listed below for each sample type. The obtained exponential curves were inverse Laplace transformed (ILT) in the MERA (Multi Exponential Relaxation Analysis) program running under Matlab software.[111] This data evaluation method results in a T_2 distribution with the most characteristic relaxation times in the maxima. The presence of 4-5 relaxation domains in the T_2 time distributions was quite reliable and reproducible. These values were further confirmed by multi-exponential fitting based on the least squares' method with the OriginPro © program. Since this evaluation method is not sensitive to merged peaks and T_2 relaxation domains with low intensities, usually ILT was applied. However, ILT sometimes tends to add irrelevant relaxation domains to the initial and final part of the T_2 distribution curves, which was handled thoughtfully, by carrying out the transformation at several fitting parameters, and by applying the same parameter set for comparative distributions.

- The hardened Portland cement pastes with varying w/c ratios were studied in a fully water saturated state (R_d= 0.5 s, *rg* = 70 dB, *ns*= 128) to see the effect of the w/c ratio on the porous structure of cement. Among the samples, hardened cement paste with w/c=0.5 was investigated in more detail. It was measured in water saturated (R_d= 10 s, *rg* =73 dB, *ns*=32), quasi-dry (air-dry, R_d= 10 s, *rg* = 79 dB, *ns*=32), and oven-dried (R_d= 10 s, *rg* = 91 dB, *ns*=32) states to study the effect of drying on the porous structure of cement. The cement samples were parallelly studied in cylindrical monolith, crushed, and powdered forms. For the comparison of the water content of the samples, the measured signal intensities were adjusted regarding the receiver gains and were converted to weight values using a calibration curve. For calibration, the proton signal intensities of the increasing amount of water were measured with similar settings (see in **Figure 5**).

The porosity (φ) of the cement samples was deduced from the volume of the pores filled with water within the cement (V_p, considering the density of water at 298 K) and the volume of the cylindrical monolith (V_t):

$$\varphi = \frac{V_p}{V_t} \qquad (10)$$

The T_2 distribution curves were numerically integrated with the OriginPro® software to obtain cumulative curves, the maximum value of the relative scale of which was adjusted to the porosity.

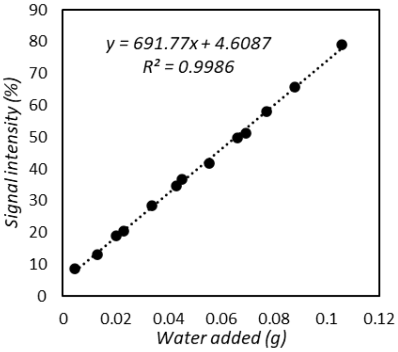

Figure 5.: Water calibration curve: the correlation between the proton signal intensity and the added water amount (R_d= 10 s, rg= 79 dB, ns=32).

- The curing process of Portland cement and the pozzolan composites (see in **Table 1**) was in-situ followed by NMR relaxometry. After the dry materials (cement/+ metakaolin/ +fly ash) were mixed with water, the paste was immediately poured into an NMR tube (10 mm). The T_2 relaxation decays were recorded at room temperature (298 K) for 48 hours (R_d= 5 s, rg = 61- 67dB, ns=16).
- To study the porous structure of the pozzolan composites (Mc10-30, Fc10-30, see in **Table 1**), the hardened cylindrical samples were soaked in deionized water for several days. After removing the samples from water, the remaining water droplets were wiped off from their surface, to detect only the water in the pore structure. The T_2 relaxation decay of the cement samples was measured as described above.
- For the pore structure characterization of the complexing agent containing model cemented waste packages, the cylindrical samples were soaked in deionized water (MilliQ) right before the measurement and were degassed using vacuum. This aimed to avoid the leaching of the introduced components and the structural changes

due to the possible dissolution of precipitated constituents, which could happen during a longer soaking time. The T_2 relaxation decay of the samples was measured with R_d= 5 s, *rg* = 73 dB, *ns*=64. For testing the long-term effect of the waste storage conditions, the cylindrical model waste packages were placed in the western ditch of the NRWR with the permission of PURAM. Their structural change was followed for 10 months by NMR relaxometry (R_d= 5 s, *rg* = 74 dB, *ns*=32).

- To identify the water types, present in the layered structure of Na- and Ca-bentonite at different water saturated states, samples with various water content were prepared 3-4 months in advance before the NMR relaxometry measurement to reach the equilibrium swollen state of the samples. The water content of Ca-bentonite samples varied between 1.5-2 g/g, while it increased from 2.5g/g to 8.5 g/g for the Na-bentonite sample. The suspensions were homogenized by mixing and the T_2 relaxation of the confined water was measured using the following settings: R_d= 1 s, *rg* = 58 dB, *ns*=32.
- To study the swelling behavior of Na- and Ca-bentonite, the dry powders were mixed with water directly before the measurements. The water content was 8.5 g/g for Na-bentonite and 2.2 g/g for Ca-bentonite. The swelling process was followed in-situ by repetitive CPMG measurements with similar settings for 48 hours.
- The two borehole samples of the Boda Claystone Formation (BCF) were studied in water saturated (model solution) and oven-dried states by NMR relaxometry to determine the so-called $T_{2cutt\text{-}off}$ value of the bound water content within the samples. The cylindrical samples were placed in a 10 mm glass NMR tube, and the relaxation process of water was followed (R_d= 10 s, *rg* = 59- 95 dB, *ns*=512). Due to the low water content of the samples, the decay curves of the samples were corrected with the NMR signal measured in an empty glass tube. The porosity of the borehole samples was determined by water calibration as was detailed in case of pure cement. To gain the $T_{2cutoff}$ value, the T_2 distribution curves were integrated, resulting in the cumulative curves of the samples in different states. The intersection points of the line drawn to the saturation value of the cumulative curves in the dry state and the cumulative curve belonging to the saturated sample gave the $T_{2cutoff}$ value.[112]

4.3.2. 2D NMR Relaxometry- T_1-T_2 correlation

For the T_1-T_2 NMR correlation relaxometry measurements the following hardened cylindrical cement samples were selected: pure Portland cement, the 20 m/m% pozzolan containing composites (Mc20 and Fc20), and the 5g/l and 20g/l complexing agent containing model waste packages.

The samples were soaked in deionized water (MilliQ) and measured on a 20 MHz NMR instrument (Minispec mq20, Bruker, Germany). The pulse sequence for this measurement was a modified IR (inversion- recovery) sequence, including a CPMG sequence after the 180° inverting pulse and inversion time (t_1). This way, the transverse (T_2) relaxation times were measured simultaneously, encoded into the longitudinal (T_1) relaxation measurement.[63] The correlation measurements were carried out in two steps to cover the entire relaxation time range: first to follow the fast-relaxing components the inversion time (t_1) in the T_1 measurement was varied between 0.05 ms and 50 ms, with an increment of 0.1 ms, to follow the relaxation in longer time range, t_1 was increased in 10 ms steps between 0.05 ms and 1000 ms. The parameters of the CPMG measurement were set similarly to 1D NMR relaxometry. This way, two 2D experimental datasets were obtained, which were merged. The two-dimensional Laplace invert of the merged 2D data matrix resulted in a T_1–T_2 correlation map, containing information about the correlation of the relaxation times. The Upen2DTool program, under MATLAB®, was used for the evaluation of the 2D data matrix.[113]

4.3.3. Fast Field Cycling NMR Relaxometry (FFC NMR)

The FFC NMR measurements were carried out at the Technical University of Cluj-Napoca within the framework of a collaboration with Prof. Dr. Ioan Ardelean. The first 5 hours of the early hydration process of pure Portland cement, Mc20 and Fc20 pastes were followed by measuring the frequency dependence of the longitudinal relaxation (T_1) time of water confined in the cement pastes. The samples were prepared in situ before the measurement, and were kept at 298 K. The measurements were performed with the fast field cycling technique using a FFC instrument (SMARtracer, Stelar SRL, Italy). The measuring concept of this technique is that the polarization and detection of nuclear spins take place at higher fields while the relaxation process happens at lower fields, which increases the sensitivity of detection. The longitudinal relaxation (T_1) measurements were carried out at different Larmor frequencies (10 kHz–10 MHz). One measurement consisted of the following three steps: a) polarization of the sample at higher field B_p for a duration t_p until it reaches saturation, b) relaxation of the nuclear spins over the relaxation time t_r at lower magnetic field (B_r), c) detection of the remaining relaxation process of the spins at higher detection field (B_d) by a 90°RF pulse. This measurement process was carried out eight times during the early hydration of the cementitious materials. The 3TM software package provided by Kogon and Faux was used for the evolution of the resulting dispersion curves.

4.3.4. NMR Diffusometry

The self-diffusion of water can be measured by DOSY NMR with a stimulated spin echo sequence using gradient pulses or by H_2O-D_2O exchange diffusion techniques.

- The high-field DOSY NMR measurement could be carried out only on the fully swollen Na-bentonite sample (8.5 g/g). The suspension was placed in a 5 mm glass NMR tube. The self-diffusion of water was studied at 298 K, on a Bruker Avance II 500 NMR spectrometer, using stimulated spin echo pulse sequence containing bipolar gradient pulses (BIPLED) to decrease eddy currents.[105] The diffusion time (Δ) varied between 10- 70 ms, while the length of the gradient pulse (δ) was 2 ms. In one experiment, all parameters were kept constant except for the pulse gradient strength (G), which was increased in 32 square distant steps from 0 to 33 G/cm. The gradient was calibrated for HDO.[114] The spectra were transformed with MestReNova 9.0 software. The diffusion coefficients were determined from the fittings of the obtained echo intensity (I) as a function of $\left(\gamma^2\delta^2G^2(\Delta-\delta/3)\right)$ according to **Equation 9**.
- The diffusion of water in the following samples was followed by H_2O-D_2O exchange diffusion: pure Portland cement, the pozzolan containing composites (Mc10-30 and Fc10-30), the 5g/l and 20g/l complexing agent containing model waste packages and one borehole samples (BCF2). These samples were not suitable for the DOSY NMR measurements, due to their high magnetic impurity and fast- relaxing bound water content. In this case, strictly cylindrical sample geometry was essential, thus hardened cylindric cementitious samples and the cylindrical drilled BCF2 sample of 15 mm length and 7 mm diameter were used. The cementitious cylinders were saturated with deionized water, while the BCF2 sample was saturated with a model solution (see in **Table 3**). Afterwards, the H_2O saturated samples were placed at least tenfold ($\alpha = 10$) excess of D_2O immediately before the measurement, the pD of which was previously adjusted to the pH of the soaking water (pD~10-13, depending on the sample), using a concentrated NaOD solution. The NMR measurement was performed on a 20 MHz NMR instrument (Minispec mq20, Bruker, Germany) at room temperature (298 K). The intensity change of water protons within the sample was recorded as a function of time by FID sequence (R_d= 0.5 s, ns=512). The application of such low R_d was necessary to detect mainly the water inside the cement matrix and reduce the signal of the external liquid, which was around 18%. The exchange process was followed every 5 minutes for 4-7 days depending on the sample. The resulting intensity values were corrected, normalized, and the time dependence of the values were fitted with the mathematical model derived by J. Crank.[115]

4.3.5. NMR Cryoporometry

The pore structure of the crushed Portland cement (*w/c*= 0.48) was studied by NMR cryoporometry using cyclohexane as a test liquid. The sample was prepared 3 days before the measurement in a 5 mm glass NMR tube. The cryoporometry measurements were performed on a Bruker Avance II 360 MHz NMR instrument with a QNP direct probe. The probe-head was cooled with dried air by a BCU-05 cooling unit. A spin-echo sequence was used for the measurement with an echo time of 8-10 ms, to eliminate the broad signal of the frozen liquid. Temperature was calibrated according to the temperature-dependent chemical shifts of neat methanol.[116] The frozen sample was melted and frozen in several steps in the temperature range 276-280 K. The proton spectrum of the molten liquid was recorded at each temperature and was transformed with MestreNova9.0 software. The system-specific freezing and melting curves resulted from the change of the integrated intensity changes of the proton signals as a function of temperature, from which the pore sizes were calculated using **Equation 8**.[101] The pore size distribution was obtained by numerical derivation.

4.3.6. Scanning electron microscopic imagining (SEM)

The SEM measurements were carried out at the HUN-REN Institute for Nuclear Research within the framework of a collaboration with Dr. Attila Csík. The surface morphology of pure Portland cement, the pozzolan composites (Mc10-30, Fc10-30) and the complexing agent containing model waste packages (0-20 g/l) was characterized by a dual beam scanning electron microscope type Thermo Fisher Scientific-Scios 2 (FIB-SEM, Waltham, MA, USA), equipped with Bruker Quantax Energy Dispersive X-ray system (EDS) for composition analysis. The microscope operated at low accelerating voltage (~5 keV) and current (~0.1 nA) to avoid the charge accumulation. Applying such low energy allowed the investigation of the surface morphology of insulating samples without coating them with a gold layer.

4.3.7. Low temperature nitrogen adsorption

The micro- and mesoporous structure of pure Portland cement and the pozzolan composites (Mc10-30, Fc10-30) were studied by low temperature nitrogen adsorption within the framework of a collaboration with Prof. Dr. Krisztina László from the Budapest University of Technology and Economics. The powdered samples were evacuated at 383 K for 24 hours before the measurement. The nitrogen adsorption isotherms were recorded by a NOVA 2000 (Quantachrome) automatic analyzer at 77 K. The primary adsorption data was evaluated by the Quantachrome software

ASiQwin version 3.0 and the apparent specific area, the pore size distribution and the pore volume of the cementitious samples were determined.

4.3.8. Mercury Intrusion Porosimetry (MIP)

The porous structure of pure Portland cement was studied by mercury intrusion porosimetry within the framework of a collaboration with Dr. Cedric Gommes and Dr. Léonard Alexandre from the University of Liege. The experiments were performed on a sample with cylindrical geometry with height of ~1-1.5 cm and diameter of ~ 0.6 cm. The cement sample was previously vacuum-dried, then measured with Quantachrome Poremaster 60 in a pressure range of 0.009 MPa – 400 MPa (the examined size range was ~160 μm – 3.6 nm). Calibrated penetrometers were used for the porosity measurements, which allowed the calculation of the apparent volume and density of cement. The size distribution of pure cement was calculated using the Washburn equation (**Equation 4**), with the assumptions of connected, cylindrical pores.

4.4. Leaching studies

4.4.1. Accelerated Leaching Test

The leaching tests of the complexing agent containing model waste packages were performed in accordance with the standard accelerated leaching test method (ASTM C 1308-08)[117] developed for diffusive emissions from solidified wastes, with the goal of following the diffusion of selected ions from the complexing agent containing model waste packages. Pure Portland cement was used for comparison and as background. The hardened cement specimens were soaked in the amount of distilled water ($V_{leachant}=10*A_{specimen}$) specified in the standard for 11 days. The leaching experiment was carried out in a thermostatic cabinet with precisely set and controlled humidity and temperature values ($T\sim$ 298 K). The leachant was replaced after 2, 5, 17, 24, 48, 72, 96, 120, 144, 168, 192, 216, 240, 264 hours.

4.4.2. Inductively coupled plasma mass spectrometry (ICP-MS)

Among the introduced model ions, the release of ^{133}Cs, ^{60}Ni and ^{185}Re was investigated. The quantitative determination of the dissolved model ions was performed by inductively coupled plasma mass spectrometry at Isotoptech Ltd. A portion of the leachates was taken for elemental analysis and preserved with HNO_3. Before the elemental analysis, the solutions were filtered through a 0.45 μm cellulose acetate filter membrane. The amount of leached ^{133}Cs, ^{60}Ni and ^{185}Re was determined using an Agilent 7500 ICP-MS instrument. As an internal standard, 200 µg/l In solution was used, which was mixed on-line with the sample before nebulization. The following ions were detected: ^{60}Ni$^+$, ^{133}Cs$^+$, ^{185}Re$^+$. The measured intensities were corrected with the inner standard and the values for pure Portland cement (without additives). Knowing the amount of model ions introduced during sample preparation, the incremental (*IFL*) and cumulative (*CFL*) leached fractions were determined as a function of the concentration of the complexing agents. The effective diffusion coefficients of the model ions were calculated according to the ASTM C 1308-08 standard[117] by fitting the leaching curves with the least squares method using OriginPro © and Microsoft Excel Solver software.

4.4.3. High- field NMR

To qualitatively identify the dissolved organic content of the leachates, the model waste package samples prepared with the two extreme values of the complexing agent concentration range (5 g/l and 20 g/l) were soaked in excess distilled water ($V \sim 20$ ml). The leachates were lyophilized, and the remaining solid was dissolved in D_2O and intruded into 5 mm glass NMR tubes. The 1D and 2D ^{1}H and ^{13}C NMR experiments were performed at 298 K on a Bruker DRX 400 NMR and a Bruker Avance II 500 NMR spectrometer using standard pulse programs (^{1}H, ^{13}C, DOSY, COSY, HSQC) provided with the spectrometer. The measured 1D and 2D spectra were processed by MestreNova9.0 software.

5. Results

5.1. Binders for radioactive waste immobilization

5.1.1. Portland cement

Effect of the water-cement ratio

Portland cement was invented more than 200 years ago, and since then it has been an indispensable part of human life. [118] During this time, numerous research has been conducted, highlighting that one of the most important factors influencing the properties of cement is the water -cement ratio (*w/c*).[39, 119, 120] This parameter represents the ratio of the weight of water to the weight of dry cement powder used for mixing. As cement encounters water, hydration reactions occur, resulting in the precipitation of the above-mentioned hydration products (see in the *Introduction*). Based on Powers' empirical model the added water is consumed (chemically bound water in gel solid) or bound (physically bound water as gel water) by the precipitated hydration products, and the remaining liquid increases the porosity of the hardened cement (capillary water).[37, 38, 121-123] At the end of the hydration, the amount of chemically and physically bound water is 0.23 g/g cement and 0.19 g/g cement, respectively, based on Powers' water vapor sorption measurements.[37, 38, 122] Thus, above *w/c*= 0.42 (0.23+0.19), the cement hydration process can be considered unimpeded and complete.[122] In practice, usually *w/c*= 0.3 - 0.7 ratios are used depending on the composition of the solid phase.[39, 71, 120, 121]

The effect of the *w/c* ratio on the Portland cement used for the experiments in my research was also investigated by NMR relaxometry.[71, 87, 124] **Figure 6a** shows the resulted T_2 transversal relaxation time constants of water confined in hardened cement paste samples prepared with *w/c*= 0.40 – 0.60 ratios with 0.02 increments. Three water domains can be distinguished with the applied short relaxation delay time: two of them can be assigned to chemically bound in the gel solid (T_{2ab} < 1 ms) and the third one to the physically bound gel water (T_{2c} = 1.5 - 3.5 ms). With increasing water-cement ratios, a plateau can be observed around *w/c*= 0.45-0.55, suggesting an optimal mixing ratio for Porland cement. Similar increasing trends were found by Pop et al. in water saturated grey cement and by Bede and Ardelean in cyclohexane saturated white OPC.[87, 124] From the obtained water-cement ratio range, *w/c* =0.5 was selected for preparing further cement samples.

Based on Powers' empirical model, the phase distribution of a Portland cement paste with w/c =0.5 was estimated over the hydration process and is shown in **Figure 6b**. The relative volume fractions of the phases (V_i) were calculated based on the work of Jensen and Hansen, knowing the density of cement (ρ_c= 3150 kg/m^3) and water

(ρ_w= 1000 kg/m^3), and their mixing ratio (w/c).[122] The model concludes the volume fractions at complete hydration (α = 1) as follows: 0.59 for gel solid, 0.23 for gel water, 0.10 for the capillary water, and 0.08 for the pores formed due to the chemical shrinkage.

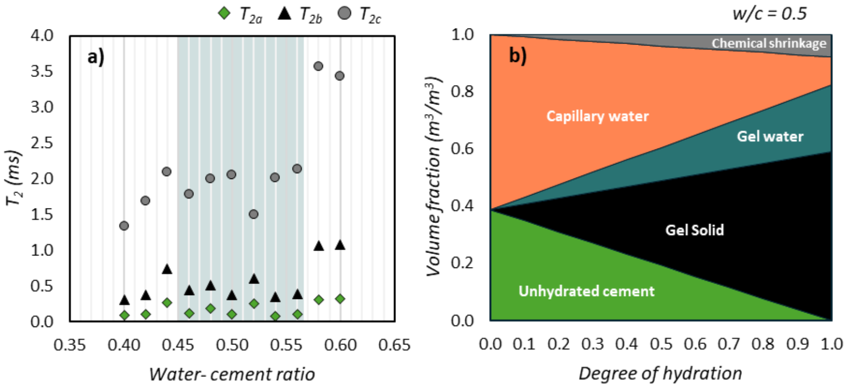

Figure 6. a) Effect of the water- cement ratio on the transversal relaxation of water confined in the CSH gel. (R_d = 0.5 s) Different colors indicate water chemically bound in gel solid (T_{2a}, green, diamond and T_{2b}, black, triangle) and physically bound in gel water (T_{2b}, grey, circle). **b)** The phase distribution of hardening Portland cement pastes with w/c = 0.5 according to the Powers' empirical model.

Considering the amount of chemically and physically bound water in the gel phase (0.23 g/g cement and 0.19 g/g cement respectively), the relative ratio of them can be calculated. Using this ratio, the volume fraction of the chemically bound water can be specified within the gel solid phase. Therefore, the hardened Portland cement consists of 59% gel (31% solid and 28% chemically bound water), 23% gel water, 10% capillary water, and 8% water filling larger spaces.

Porous structure of Portland cement

Several models exist describing the porous structure of the main cement hydrate phase, the CSH gel.[34-36] The most used one for the interpretation of NMR relaxometry results is the continuous model by Feldman and Sereda.[35 58, 60, 125, 126]According to this model the CSH gel is a disordered, continuous assembly of highly defective CSH sheets and four pore types can be distinguished within the solid matrix: intra CSH sheet pores (d = 0.5-1.8 nm), inter CSH gel pores (d = 2-10 nm), capillary pores (d = 20/50 nm-600 nm) and air pores (µm to mm size).[58, 88, 95] A schematic representation of the porous structure of hardened cement paste is shown in **Figure 7**.

The water types determined by the Powers' model may be assigned to the listed pore types as: gel water may fill the intra CSH sheet pores and inter CSH gel pores, while the other two may fill the larger capillary and air pores. With this assignment, we can compare the pore ratios obtained from NMR relaxometry measurements with the calculated values. With the application of NMR relaxometry one can gain insight into the pore structure of a hardened cement binder, since the T_2 transverse relaxation time of water is highly sensitive to molecular motions and thus to the size of the confining space on nanometer-scale.[72] This enables the calculation of the size of the water saturated pores according to **Equation 7**.[72, 79, 80, 82, 83]

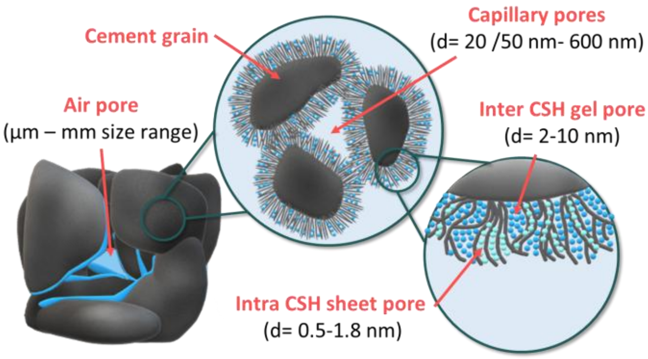

Figure 7. Schematic representation of the porous structure of cement

One of the most critical parts of obtaining pore sizes from relaxation times is the lack of knowledge of an exact surface relaxivity parameter, which reflects the strengths of the interactions between the pore surfaces and the mobile nuclear spins.[72, 84] Commonly two methods are used for the determination of surface relaxivity: one is by calculating ξ according to **Equation 7** from independently measured S/V ratios, resulting from mercury porosimetry or nitrogen adsorption.[82, 127-129] The other is by drying the cement sample to monolayer coverage and measuring the T_2 relaxation time of the remaining water.[86, 130, 131] Then ξ can be calculated knowing the thickness of one water molecule (λ = 0.28 nm)[86]:

$$\xi = \frac{\lambda}{T_{2s}} \qquad (11)$$

where T_{2s} is the measured transversal relaxation time constant of monolayer water.[80, 82, 83] Since cement is a heterogenous matrix, the determination of an exact value may be complicated by the presence of numerous inorganic phases. Dalas et al. determined the surface relaxivity of cement hydrates and found that the ξ of ettringite was remarkably high (~ 26−52 nm/ms) compared to other phases, while ξ ~ 2.2−6.9 nm/ms values were found for CSH gel.[130] Bryar et al. suggested that in heterogenous multicomponent systems, such as cement, the observable surface relaxivity is the weighted average of the inherent relaxivities of the individual components.[131, 132] In the literature, we can find values for the surface relaxivity of cement that range within wide limits: 3.73 nm/ms[86] has been found for white Portland cement stone, 1.88 nm/ms[133] for white cement mortar, while 1 nm/ms[103] for mortar. For the estimation of the pore size distribution of our hardened Portland cement paste, ξ = 1.88 nm/ms[133] was used in the calculations, with the assumption of planar pores ($S/V = 2/d$), where d means the thickness between the planar pores.[131]

In this *Section* the T_2 relaxation time constants of the specimen are converted to pore size values to compare different structural characterization techniques. **Figure 8a** shows the pore size distribution curve of the hardened Portland cement paste, where five different relaxation domains can be separated and assigned to the related pore types as follows: intra CSH sheet pores ($d < 2$ *nm*), inter CSH gel pores ($2\ nm < d < 20\ nm$) and capillary pores ($20\ nm < d$). Since the peak intensities of the distribution are proportional to the water amount of the given type, the quantitative contributions of the pores to the solid matrix can be obtained. By careful calibration (see in **Figure 5**) the areas under the peaks can be matched to the exact amount of water confined in given pores. Thus, the porosity of the examined cement sample was φ = 0.35. Dividing the porosity among the pore types, and calculating the volume fraction of the solid, the following volume ratios were obtained: the studied hardened Portland cement consisted of 65% solid gel, 17% intra CSH sheet pores, 14% inter CSH gel pores, 4% capillary and air pores. NMR relaxometry is less sensitive to larger capillary pores ($d \geq 0.1$ μm), since the saturation of these pores is difficult to implement and the effect of the pore walls is less dominant.[71] Thus, NMR relaxometry underestimates the presence of larger pores. Comparing the ratio of intra CSH sheet and inter CSH gel pores resulted from NMR relaxometry (0.17 /0.14 ~ 1.2) with the one calculated based on Powers' model (0.55 /0.45 ~ 1.2), the proportion of them are identical, confirming the identification of the pores by NMR.

Although NMR relaxometry may not be the most suitable method to characterize macropores, there is an alternative NMR technique sensitive to larger pores (up to several hundred nm) called NMR cryoporometry.[101, 102] As it was discussed earlier, the method is based on the fact that confinements with various geometries and sizes differently affect the freezing–melting process of the filling liquid. The hardened Portland cement paste was saturated with cyclohexane, a non-polar liquid, and the signal intensity of the proton spectra of the molten liquid was recorded between 276 – 280 K. The resulting melting and freezing curves are shown in **Figure 8b** with different colors. The lack of melting-point depression suggested slit-like pore geometry, as expected based on the models describing the structure of cement.[34, 35]

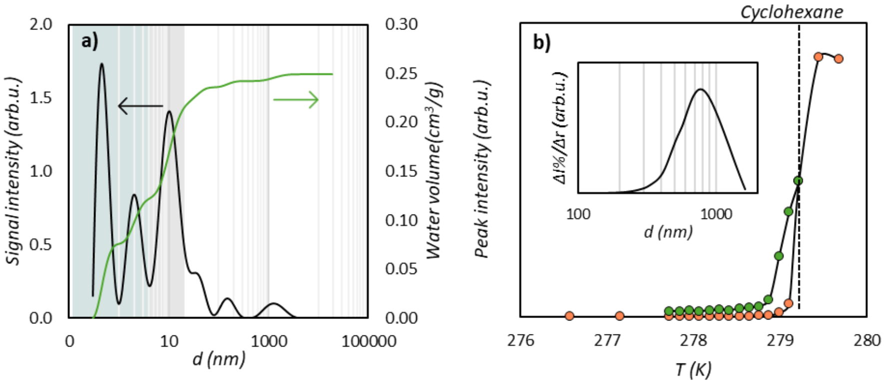

Figure 8. a) The pore size distribution (black) and cumulative pore volume distribution (green) curves of Portland cement (*w/c*=0.5) from NMR relaxometry. The intervals with different colors indicate the assignment of the relaxation domains to pore types: intra CSH sheet pores (blue), inter CSH gel pores (gray), and capillary pores (no color). **b)** Melting (orange) and freezing (green) curves of Portland cement (*w/c*=0.48) and the calculated pore size distribution curve (inset). The dashed line stands for the bulk transition temperature of cyclohexane (T_0).

The size of the pores ($d= 2r_p$) was calculated according to **Equation 8** (K_c = 96 nm K for cyclohexane[101]), where n= 1 was used because of the slit-like geometry.[100] The calculated pore size distribution is shown as an inset in **Figure 8b** and reveals a wide range of pore sizes with a maximum around d~ 800 nm. These pores may be attributed to the larger capillary pores or air pores less visible with NMR relaxometry. Here, it is important to highlight that the calculated pore sizes are close to the upper detection limit of NMR cryoporometry; however, the presence of freezing-point depression confirms the applicability of the method for cement characterization. The examination of smaller pores ($d \geq$ 2nm) may be possible with this technique; however, the short relaxation time of water in the CSH gel hinders their detection.

To support these NMR results, other conventional characterization techniques were used to study the structure of hardened Portland cement paste in the framework of collaborations. The mercury intrusion porosimetry (MIP) measurement was carried out on a similar cement sample. MIP is a well-established method of pore size and volume determination, where the applied intrusion pressure of mercury is inversely proportional to the pore size.[48, 51, 134] However, the accuracy of MIP data is controversial for cementitious materials because of the possible microstructural damages of the samples during the pretreatment (drying) and during the measurement due to the applied pressure.[135] Also, when interpreting the results, we must consider that the method provides information about a simplified system (containing pores with continuous cylindrical geometry).[135, 136] With these considerations, we can use this method to supplement NMR results. The resulting intrusion curve (intruded volume - pressure) of the cement sample was converted to a cumulative pore volume distribution curve according to the Washburn equation (**Equation 4**), which curve is shown in **Figure 9** (with green color), The maximum of this curve indicates the volume of pores accessible for mercury (~ 0.22 cm^3/g). By converting the mercury intrusion curve to logarithmic differential pore volume curves, the pore size distribution (**Figure 9**, black curve) of cement was obtained.

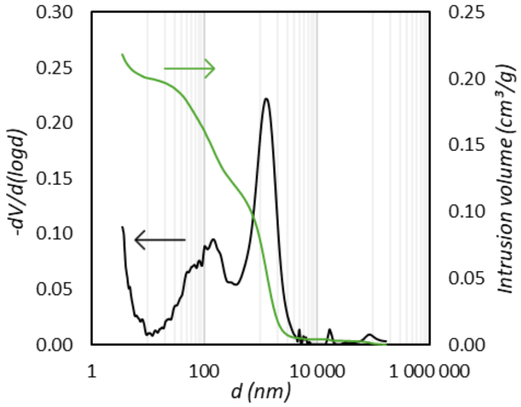

Figure 9. The pore size distribution (black) and cumulative pore volume distribution (green) curves of Portland cement (*w/c*=0.52) from mercury intrusion porosimetry.

With the MIP method, the size of large capillary pores, air pores, and microcracks of several hundred nanometers can be determined with great certainty. The few nanometer-sized pores in the CSH gel, which largely contribute to the pore structure of cement, are less visible with this technique.[85] In the hardened Portland cement paste mainly the d_1 ~ 160 ± 100 nm and d_2 ~ 1350 ± 530 nm sized pores dominate the macroporous structure. The size of the small capillary pores is well comparable with the one calculated from the T_2 relaxation time distribution curve. Although the two methods calculate the pore size based on different geometries, the obtained results nicely complement each other.

The other frequently used porosimetry technique is the low temperature nitrogen adsorption, which was also used for the pore structure characterization of Portland cement. In contrast with MIP, nitrogen adsorption is sensitive to the micro- and mesostructure ($d \leq 2$- 50 nm) of a solid material.[52, 55] The resulted N_2 sorption isotherm is shown in **Figure 10a**, and according to IUPAC, it can be categorized as *IVa* – II transition type with an *H3*-like hysteresis loop.[54] Materials that have predominantly micro- and mesopores beside macropores fall into this category.[54, 137] The *H3*-like hysteresis loop refers to a porous structure consisting of non-rigid aggregates of plate-like particles (e.g., certain clays), or to the presence of incompletely filled macropores.[54]

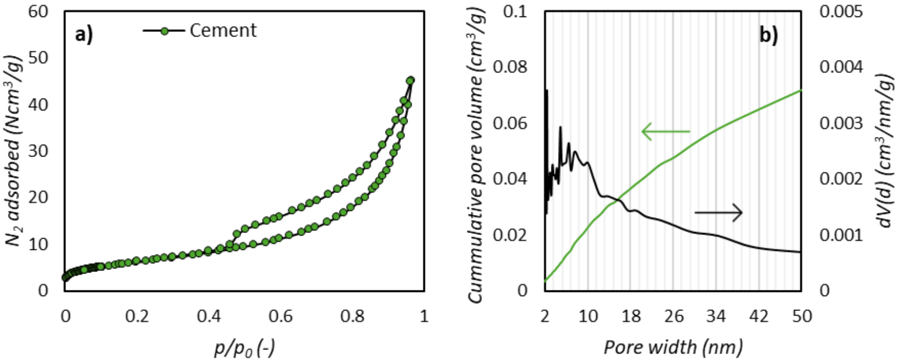

Figure 10. a) Low temperature adsorption isotherm of Portland cement (*w/c*= 0.5). **b)** The derived cumulative pore volume (green) and pore size distributions (black) of Portland cement.

The pore volume ($V_{0.95}$ = 0.057 cm^3/g) of the cement sample was estimated from the isotherm at p/p_0 = 0.95, with the assumption of the pores being saturated with nitrogen. The micropore volume (V_{micro} = 0.0081 cm^3/g) was determined from the Dubinin–Radushkevich (DR) plot of the adsorption curve.[138] The difference between the two volumes ($V_{0.95} - V_{micro}$) was the volume of the mesopores (V_{meso} = 0.049 cm^3/g). The size distribution (see in **Figure 10b**) of the mesopores was also obtained from the adsorption branch using the Barrett, Joyner, and Halenda (BJH) model.[139] The resulting pore size distribution is wide over the examined size range, with a maximum of around 7 nm. This pore size value is in good agreement with the size of the inter CSH gel pores found by NMR relaxometry. The last parameter derived from the adsorption isotherm is the apparent surface area (S_{BET} = 23 m^2/g) of pores in the cement specimen, which was calculated using the Brunauer–Emmett–Teller (BET) model.[140] This apparent surface area is slightly lower than the ones found in literature for hardened cement pastes (S_{BET} > 50 m^2/g).[28, 141] This may be attributed to the presence of porous regions being inaccessible for gas, like narrow pore entrances, closed pores formed due to the thermal damage of the hydration products or water-filled pores.[141, 142]

To compare the presented structural characterization methods, the resulting pore size distributions are summarized in **Figure 11**. The combination of these methods allows the determination of the pore sizes in cement in the full range of sizes.

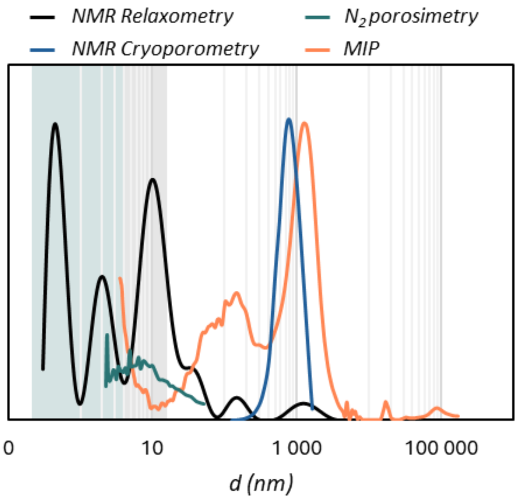

Figure 11. Comparison of pore size distributions of Portland cement resulted from different characterization methods. The intervals with different colors indicate the different pore types in cement: intra CSH sheet pores (blue), inter CSH gel pores (gray) and capillary pores (no color).

It is clearly visible that NMR cryoporometry and MIP mainly give information about the macroporous structure (capillary and air pores), while NMR relaxometry and nitrogen adsorption shed light on the meso- and microstructure of cement (pores in the CSH gel). Furthermore, NMR relaxometry may detect closed, small water filled pores (e.g. intra CSH sheet pores), which are not "seen" by the other techniques.

It is important to note that NMR relaxometry is less sensitive to larger pores, underestimating their presence and without an exact surface relaxivity value, the pore sizes are well approximated estimates. However, with these considerations it is a well applicable technique for the comprehensive characterization of the micro- and mesostructure of the main hydrate phase, the CSH gel.

Effect of the sample form

During my PhD research, I used low-field NMR techniques, mainly NMR relaxometry, to study the structure of cementitious materials. In the following, it is shown how the pretreatment of the sample influences the relaxometric results, thereby defining an appropriate sample preparation procedure for further studies. First, the pore structure of three hardened cement pastes with different forms (cylindrical, crushed, and pulverized) were tested, and the effect of the sample form was investigated. The samples were fully saturated with water to make the pores "visible"; the resulting pore size distributions are shown in **Figure 12**. The sample preparation did not affect significantly the bound water in the intra CSH sheet pores (1st peak), but the ratio of the second and third peaks, which can be assigned to the mobile water in the intra CSH sheet pores (2nd peak) and inter CSH gel pores (3rd peak). Pulverization decreased the contribution of the gel pores as well as affected the macropores, while crushing mainly changed the larger capillary and air pores. Based on this, we found the cylindrical sample shape to be the most reliable and reproducible, thus this type of sample was used in the research, as also recommended by McDonald et al.[71]

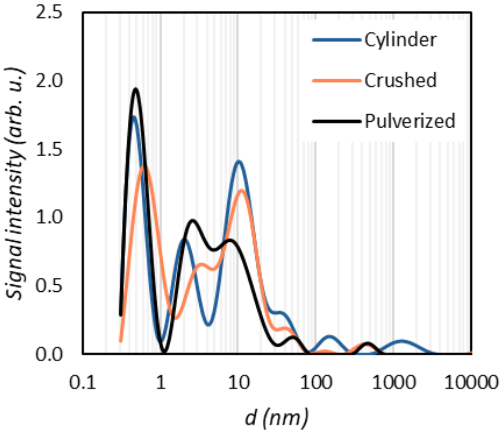

Figure 12. Comparison of pore size distributions of Portland cement with different sample forms: cylindrical, crushed and pulverized.

Water content of cement

After that, the sensitivity of the method was further tested by following the drying induced changes within the cylindrical cement sample. These tests were not only useful from the point of view of examining the applicability of the method but also shed light on the structure-forming effect of drying, the external effect that occurs during the application of the binder. This provided a good basis for interpreting the studies under real conditions.

Cement as a colloid system is sensitive to drying, which may result in the irreversible and reversible shrinkage of the solid matrix.[34, 143-145] Drying shrinkage refers to shrinkage of cement caused by moisture loss, which can lead to formation of cracks due to the induced tensile stresses at the surface and compressive stresses in the bulk.[143] Drying shrinkage is not the only type of shrinkage that cement can go through (e.g. thermal, autogenous, chemical or carbonation shrinkage), but here this phenomenon is investigated.[143] Since the specific surface area of OPC is relatively high (S~ 80-280 m^2/g), the shrinkage of cement is highly influenced by surface effects, like the capillary effect, surface adsorption, Bangham effect, or the disjoining pressure effects.[143] Also, the presence of osmotic pressure should not be neglected, since the pore solution contains ions as well.[143] As these phenomena appear upon drying, the structure of the hydration products slightly changes. The microstructure of the CSH gel is particularly sensitive to the relative humidity and can evolve after long-term drying.[146-148] NMR relaxometry is an outstanding method to study the microstructural changes of CSH over drying.[86, 144, 149-152]

The cement samples were studied in water saturated, quasi- and oven-dried states. **Figure 13a** shows the proton signal intensity decay during the relaxation measurement of the three specimens. The initial signal intensity indicated the different water contents of the samples, which were quantified by calibration (see in **Figure 5**), as discussed above. The inverse Laplace transform of the decay curve resulted in the pore size distributions of the cement (see in **Figure 13b**) after converting the T_2 relaxation time constants to size values (**Equation 7**). The water loss due to drying is observable both on the size distribution curves and on the cumulative pore volume distributions (see in **Figure 13c**) obtained from the integral of the size distributions weighted by water content.

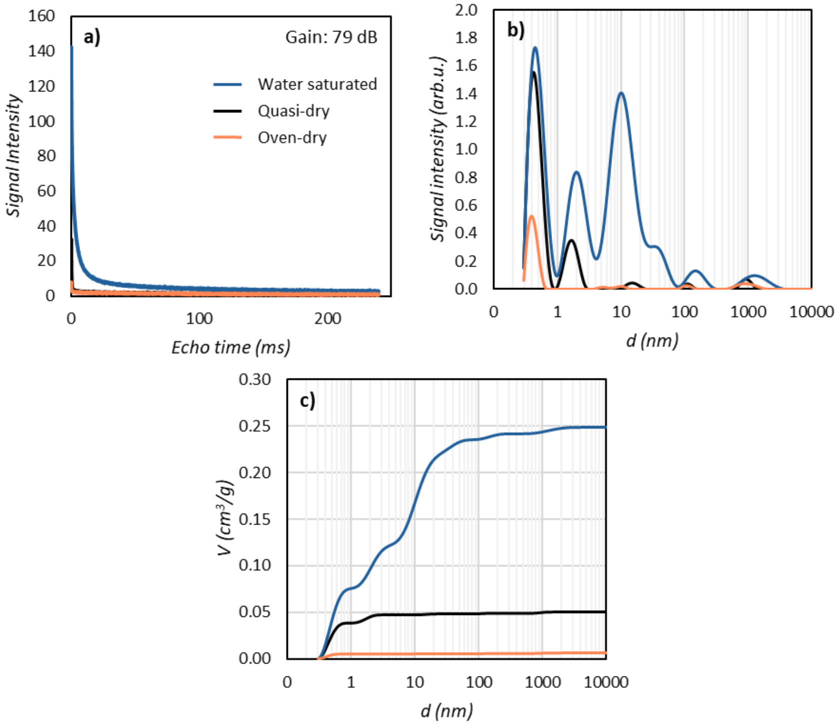

Figure 13. a) Primary data resulted from NMR relaxometry: water signal intensity as a function of the applied echo time. **b)** Pore size distributions and **c)** cumulative pore volume distributions of cylindrical Portland cement at various levels of water saturation.

Comparing the size distribution curves of cement in various conditions (see in **Figure 13b**), it is visible that the area of the peaks significantly decreased with drying. In addition, the first peak assigned to the CSH sheet pores shifted slightly to smaller size values, indicating the possible shrinkage of the CSH gel. Contrary the second peak shifted to larger size values (form ~ 2 nm to 5 nm). Similar trends were observed by Igami et al. and Gajewicz et al., who explained it with the re-arrangement of the nano-scale porosity between fine and coarser spaces in cement gel over drying.[144, 149] The changes of the first peak may also be assigned to the shrinkage of the CSH gel according to Maillet et al., who summarized the possible alterations of the relaxation domains in porous materials.[153] The remaining water signal in larger pores may be owned to water in closed pores, inclusions.

Overall, we also confirmed that NMR relaxometry is a sufficiently sensitive method to test the drying induced changes of cement, thus the structure of the binder in real condition can be monitored with it. The investigation of the effect of drying was not only suitable for testing the sensitivity of the method but also showed the structural influencing effects that may be introduced by the sample preparation of other characterization methods, which should also be considered when interpreting the results together.

5.1.2. Pozzolanic effect of metakaolin and fly ash

When conditioning radioactive waste, enhancing the sorption properties of binders is essential. This can be accomplished through the use of various additives, such as artificial silicates.[3] However, these additives can significantly affect the mineral composition of the cement and, consequently, alter its pore structure, including the size and distribution of the pores.

Degefa et al. investigated the impact of metakaolin and fly ash on the mineral composition of cement using machine learning algorithms.[154] Both additives are rich in silicon and aluminum and can participate in pozzolanic reactions during Portland cement hydration. The study found that metakaolin mainly increased the proportion of CSH gel, whereas fly ash promoted the formation of aluminum-containing phases; and both of them reduced the presence of portlandite and ettringite.[154] The addition of such materials is advantageous for radioactive waste management, as they not only increase the amount of sorbing phases but also reduce the permeability of the binder. These properties are closely linked to the pore structure of the materials, which can be effectively analyzed using conventional characterization techniques (e.g. N_2 porosimetry, SEM) as well as with less common liquid- phase NMR (Nuclear Magnetic Resonance) methods.[59, 60, 62, 63, 66, 155, 156]

The aim of this chapter of my PhD research was to comprehensively describe the effects of two pozzolanic materials - metakaolin and fly ash - and their concentrations on the early hydration, structural development, and hardened pore structure of Portland cement. A novel combination of the previously mentioned NMR methods, scanning electron microscopy (SEM), and nitrogen porosimetry was employed. The selected water-solid and additive ratios are considered suitable for current radioactive waste management standards.[157] The early hydration processes in the pozzolan-containing cement composites were monitored using low-field NMR relaxometry. The pore structure of the hardened materials was investigated in both dry and wet states: SEM imaging and nitrogen porosimetry were used for dry samples, while various liquid-phase NMR techniques were applied to wet samples. Additionally, 2D T_1-T_2 correlation NMR relaxometry and H_2O-D_2O exchange diffusion measurements were performed to assess the permeability of the pore network. The overall goal was to gain a detailed understanding of how these two pozzolans affect the composites' pore structure and their interaction with water, which are essential factors in the long-term safe disposal of radioactive waste.

Effect of pozzolans on the early hydration of cement by T_2 relaxation

When the dry cement clinker phases come into contact with water, a series of complex chemical reactions occur, involving the partial or complete dissolution of the clinker phases and the formation of new hydration products as described earlier in the *Literature overview*.[30, 31] Among the clinker phases, C_3S, the main clinker phase dominates the hydration process of Portland cement, which transforms into amorphous CSH gel and crystalline portlandite during the process. [30, 31] The hydration process of C_3S is typically divided into five well-defined stages: initial dissolution (*I*), induction (*II*), acceleration (*III*), deceleration (*IV*), and slow hydration periods (*V*).[30, 62, 158-160] The precipitation of hydration products reduces the size of the water-filled voids, thereby changing the confinement and mobility of water molecules, which can be easily monitored by NMR relaxometry.[60, 62, 124, 156, 161-163]

The early hydration of pure Portland cement and six cement composites − containing 10–30 w/w% metakaolin (Mc10-30) and fly ash (Fc10-30) − was monitored by measuring the evolution of T_2 relaxation of water over a two-day period (see in **Figure A1-2** in the *Appendix*). **Figure 14** shows the obtained T_2 values (a-c) and corresponding amplitudes (d-f) over time for pure Portland cement paste, Mc10 and Fc10 composites. Four water domains with diverse "mobility" could be distinguished within the specimens. The fourth, less certain water domain (with T_{2d} decreasing from 200 ms to 12 ms) contributes less than 1% and is not shown in Figure 10. This domain may be associated with large capillary pores.[58, 62, 92] The water domain with T_{2c} = 8 - 1.5 ms is attributed to water that initially fills smaller capillary pores and subsequently transforms into inter CSH gel pores as hydration progresses and CSH gel precipitates. Water domains with shorter T_2 relaxation times (T_{2a} ~ 0.10 - 0.13 ms and T_{2b}~2 ms - 0.5 ms) correspond to water filling intra CSH sheet pores of varying sizes, with their associated signal amplitudes ($A_{a\text{-}b}$) increasing as the CSH gel forms.

Comparing the relaxation times related to the intra CSH sheet pores in cement, Mc10 and Fc10 (see in **Figure 14**), it is observable that the value of $T_{2a\text{-}b}$ does not differ significantly, while their amplitudes ($A_{a\text{-}b}$) are more prevalent in the case of Fc10. The most notable change in T_2 and amplitude during hydration takes place in the third water domain, where the initial value of T_{2c} is shorter for Fc10 (T_{2c} = 6.4 ms), than for pure cement (T_{2c} = 7.9 ms) or for Mc10 (T_{2c} = 8.9 ms). The evolution of this relaxation domain over the hydration process is also more prolonged for the fly ash containing sample compared to the others.

The change in the obtained T_2 relaxation times can be divided into distinct sections, that reflects the above-mentioned five stages (*I-V*) of the hydration process. In the first several minutes (<15 min), the rapid dissolution the most reactive clinker phase (C_3A) takes place resulting the precipitation of ettringite, entailing the sudden reduction in the size of the confinements and the dissolution of magnetic impurities. [30, 60, 62, 156] Parallelly, the hydration of C_4AF occurs, increasing the concentration of paramagnetic ions.[30] These processes in the *initial dissolution (I)* period quickly and drastically decrease the value of T_2 and are difficult to follow by NMR.

After the fast dissolution of C_3A and C_4AF clinker phases, the hydration of cement slows down and stagnates in the *induction (II)* period. Among the numerous theories explaining this phenomenon, dissolution control and protective membrane models are the most widespread ones.[159, 160] The dissolution control theory assumes that the supersaturation of the pore solution with calcium and silicate is necessary for the formation of portlandite, which afterwards drives the precipitation of the CSH gel.[62, 159, 160] The protective membrane model explains it by the formation of a coating layer on the surface of the cement grains, which prolongs the supersaturation by hindering the exchange of water between the gel and the bulk.[159, 160] Since no noteworthy structural changes occur in this period, the observed T_2 relaxation times stagnate.

As the supersaturation of the pore solution is reached, the massive precipitation of portlandite and CSH gel commences in the acceleration period (*III*). Also, the formation of monosulfoaluminate from ettringite begins simultaneously.[30] These entail the size decrease of the confinements and affecting significantly the T_2 relaxation time, as well as the amplitudes of the most bound water domains in the CSH gel ($A_{a\text{-}b}$, see in **Figure 14d-f**).

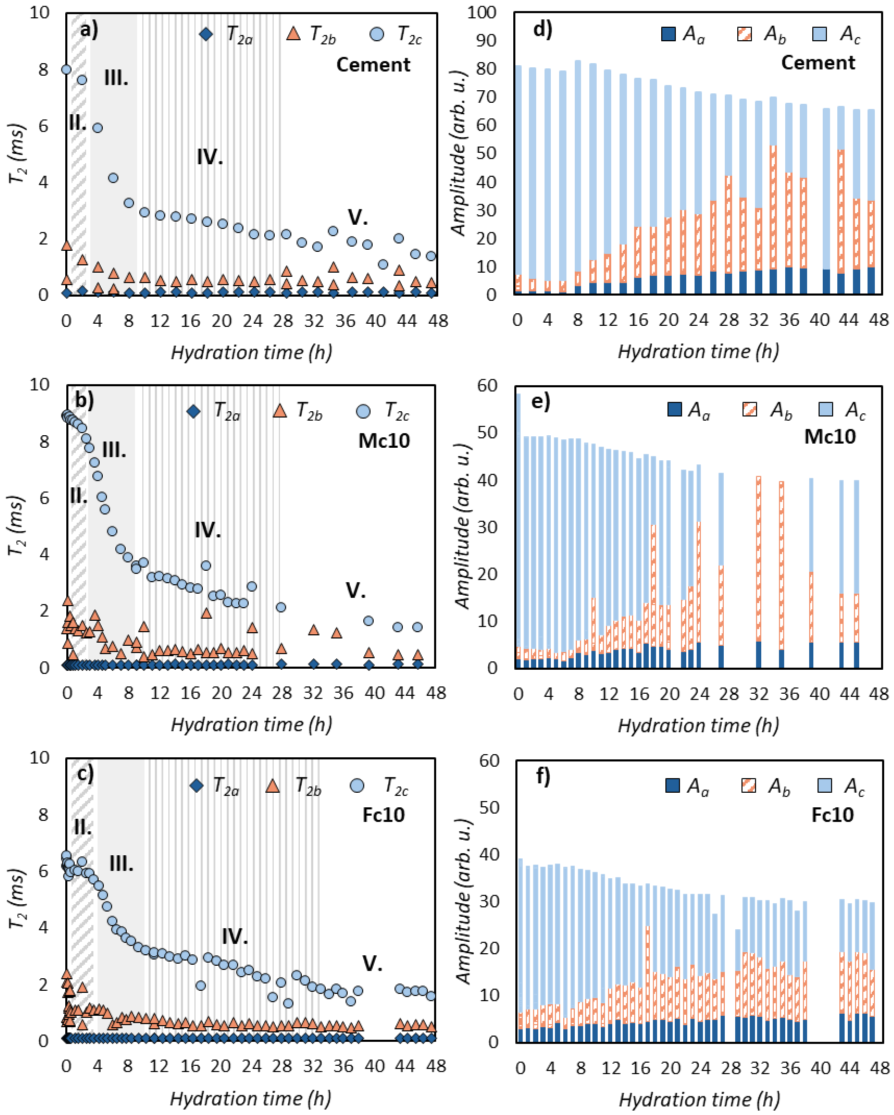

Figure 14. T_2 relaxation time constants over time for **a)** pure Portland cement, **b)** 10% metakaolin and **c)** 10% fly ash containing composites during the hydration process. Water domains in different confinements are color coded: intra CSH sheet (T_{2a}, dark blue, diamond), inter CSH gel (T_{2b}, orange, triangle) and smaller capillary pores (T_{2c}, light blue, circle). The five stages of the hydration process are indicated in Roman numerals. **d-f)** The amplitude changes of the listed water domains over time, with the same color codes.

The process slows down in the following periods – in the *deceleration (IV)* and *slow hydration (V)* periods – since the diffusion of water in the densifying matrix becomes hindered.

Water is a reaction partner for cement during the hydration process, thus its amount decreases over time, as is reflected by the change of the total amplitude of water (see in **Figure 14d-f**). With the addition of pozzolans, the hydration process may slightly alter from pure Portland cement, because the active silica and alumina content of the additives also participate in the chemical reactions.[156, 164, 165]

For the comprehensive and insightful understanding of the effects of pozzolans on the early hydration of cement, the amplitude weighted T_2 relaxation times ($\overline{T_2}$) were calculated based on [166]:

$$\overline{T_2} = \frac{\sum_a^i A_i \times T_{2i}}{\sum_a^i A_i} \qquad (12)$$

where A_i is the amplitude, T_{2i} is the transverse relaxation time constant of the i-th water domain ($i=a$-d) at t hydration time. The decrease of $\overline{T_2}$ over the early hydration of pure Portland cement and the cement composites is shown in **Figure 15**, mainly reflecting the change of T_{2c}.

The advantage of using $\overline{T_2}$ is, that the changes in the system during hydration are better emphasized as weighting the relaxation times smooths the uncertainties resulting from the Laplace inversion. Comparing the change of $\overline{T_2}$ over time, for the different cement specimens, the first notable difference between them is the initial value of $\overline{T_2}$: the relaxation of water is outstandingly faster in the fly ash composites ($\overline{T_2} \sim 2.2 - 5.2$ ms), compared to pure Portland cement ($\overline{T_2} \sim 7.4$ ms) and the metakaolin containing ones ($\overline{T_2} \sim 8.2$ ms). Considering **Equation 7** the enhanced relaxation of water may be owned either to the smaller size of the confinement or to the disparate surface properties of the solid (surface relaxivity – ξ). The surface relaxivity of a solid may depend on *a)* the presence of magnetic susceptibility variations or paramagnetic impurities in the material, and *b)* the wettability of the surface, which influences fluid-solid interactions. The iron content of the solid is considered as paramagnetic impurity due to the paramagnetic moment of Fe^{3+} ions. The iron content of fly ash is higher compared to metakaolin, as the composition of the additives suggests.

According to several studies, pozzolans act as chemically inert fillers during early hydration and only affect the later stages through pozzolanic reactions.[156, 164, 167] However, the second difference is how the pozzolans affect the speed of the process and the length of each period. In the case of metakaolin, the difference is mostly found in the deceleration (*IV*) period, where the moderate precipitation of CSH gel and monosulfoaluminate occurs. Based on the calculations of Degefa et al., the excess alumina and silica introduced by the pozzolans, partially incorporate into the CSH gel and lead to the formation of CASH (calcium-alumino-silicate hydrate) gel alongside the CSH gel in the hardened cement.[154] The formation of aluminate-containing hydration products (such as monosulfoaluminate, hydrogarnet, hydrotalcite) is also enhanced by the presence of pozzolans.[154] The rate of the declaration period, thus the speed of precipitation, highly depends on the concentration of metakaolin as the slope of the curves suggests in **Figure 15b**. The other periods of the hydration of the metakaolin composites are like those of pure cement (see in **Figure 15a**).

In contrast, the presence of fly ash influences the whole hydration process. This additive prolonged the duration of the induction period (*II*) and decreased the speed (slope) of the acceleration (*III*) and deceleration (*IV*) periods as shown in **Figure 15c**. These deviations from pure cement become more noticeable with increasing fly ash concentration.

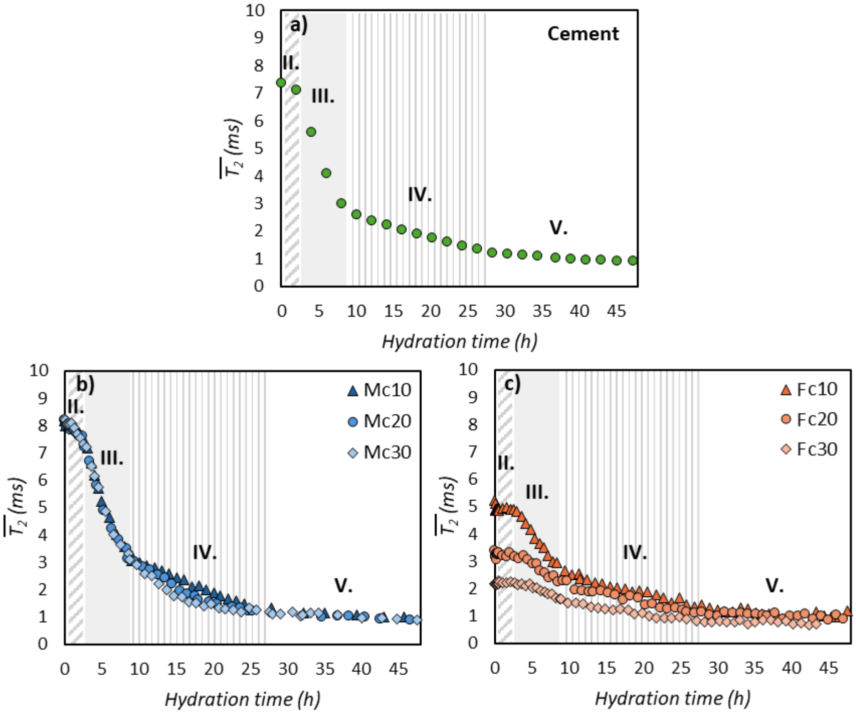

Figure 15. Change of the weighted T_2 relaxation time ($\overline{T_2}$) over the early hydration process for **a)** pure Portland cement, **b)** 10 - 30% metakaolin containing and **c)** 10 - 30% fly ash containing cement composites. The stages of cement hydration are marked according to pure Portland cement.

Two pozzolans, with similar composition but different effects, what could be the reason? It can be explained by their dissimilar pozzolanic activity.[168]

- Metakaolin is a synthetic, amorphous aluminosilicate having higher active, easily releasable alumina and silica content, which may take place in the accelerated formation of C(A)SH gel and other aluminum containing minor phases in the presence of portlandite ($Ca(OH)_2$).[167, 169-171] Thereby, metakaolin is able to participate in the initial periods of cement hydration and exerts its catalyzing effect, also confirmed by the higher cumulative heat evolution found in isothermal calorimetry studies.[172, 173]

- Fly ash also participates in the same reactions as metakaolin, only delayed; in the initial stages it acts as an inert filler material.[156, 169] The lower initial reactivity of fly ash may be owed to its higher inactive alumina and silica content, since it is an industrial byproduct. [167, 169, 170] The hindered early hydration of the fly ash composites can be explained by the filler or dilution effect, meaning that the spherical fly ash particles as inert fillers may increase the apparent water-cement ratio (by replacing cement) and may adsorb the dissolved ions (e.g. Ca^{2+}).[156, 165, 170] These lead to the slower supersaturation of the pore solution and the hindered precipitation of the hydration products.[156, 165, 170]
- In addition to these, the available porosity of cements is another influencing parameter regarding the pozzolanic activity of the additive.[168] Available porosity refers to the porosity of cement, which can be filled with hydration products.[168] This limiting factor may have a more crucial role in the case of fly ash compared to metakaolin, since the later one exerts its pozzolanic effect during the initial periods of the hydration. As the pozzolanic activity of fly ash takes effect in later stages, the refining pores may restrain the growth of hydrates.[168]

Effect of pozzolans on the early hydration of cement by FFC NMR

To better understand the effects of the pozzolans on the early hydration of cement as well as to gain information about the surface evolution of the materials and the dynamics of the confined water molecules, FFC NMR measurements were performed. The first 5 hours (*I-III.* periods) of the early hydration of Portland cement, Mc20 and Fc20 samples were followed by recording the frequency dependent T_1 (longitudinal) relaxation of confined water molecules. Contrary to the CPMG measurement, which is sensitive to the presence of numerous water types, the FFC NMR measurements result in an average T_1 value. This T_1 relaxation time is mainly dominated by the water confined in capillary pores, likewise the presented weighted T_2 values (see in **Figure 15**).[62, 99] **Figure 16** shows the T_1 relaxation dispersion curves of the three samples over the first 5 hours of the hydration process. Similar dispersion curves have been found for gray cement in other studies as well. [90, 95, 98, 99] The above detailed diverse pozzolanic properties of metakaolin and fly ash are also observable on the evolution of the dispersion curves over time. The evolution of the curves is faster for Mc20 and slower for Fc20 compared to Portland cement.

During the FFC NMR measurements, the T_1 relaxation process is measured at several Larmor frequencies (0.01 - 10 MHz), therefore it is sensitive to a wider range of molecular mobilities compared to a single frequency.[62] The resulting dispersion curves may be explained by employing theoretical models which can describe the relaxation process and provide useful information about the nano-scale dynamics of confined water molecules. One can find a variety of theoretical models in literature describing the frequency dependence of T_1 in a porous medium. These models can be classified into two broad categories according to Faux et al.: the Korb models, which assumes that the relaxation process is dominated by the presence of paramagnetic impurities, and the bulk-mediated surface diffusion (BMSD) models, that suppose a non-Fickian surface diffusion of water at pore surfaces. [174]

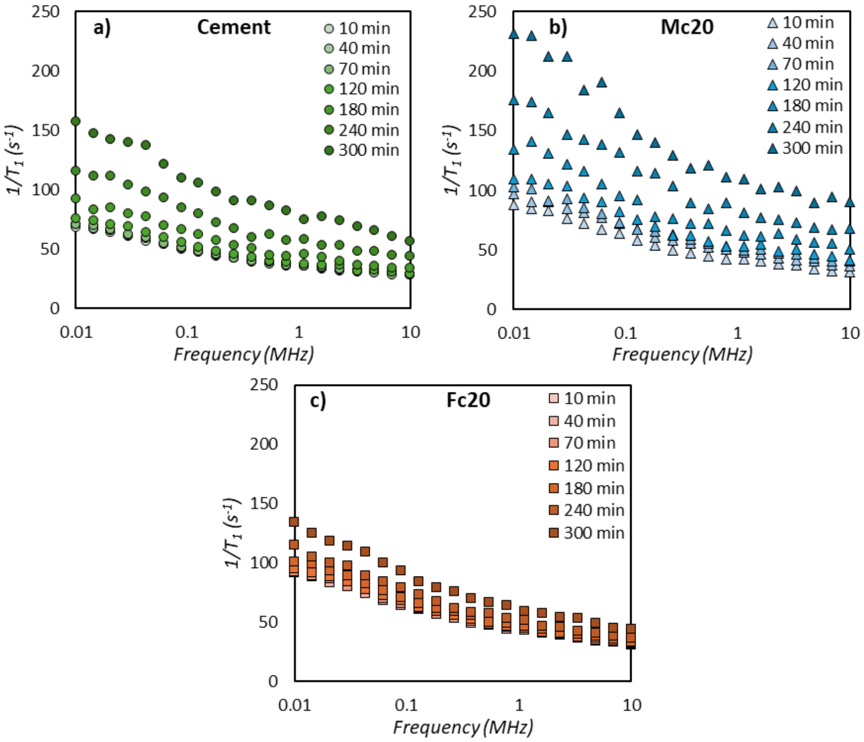

Figure 16. The T_1 relaxation dispersion curves of **a)** Portland cement, **b)** 20% metakaolin and **c)** 20% fly ash containing cement composites over the early hydration process. The curves show the progress of time from bottom to top.

In the present work we used the *3-Tau* model created by Faux et al. and to our best knowledge this is the first time to apply the *3-Tau* model to investigate the effect of pozzolans during the early hydration of cement.[174-176] According to this model, water is present within the porous solid containing paramagnetic impurities (e.g. Fe^{3+}): a) in the surface layer with the thickness of one water molecule ($\delta = 0.27$ nm) and b) in the bulk-like state as **Figure 17** shows.[62, 174, 176] The thermally modulated dipolar interactions between the water proton spins and the spin of the unpaired electron of

Fe^{3+} within the solid phase dominate mainly the longitudinal relaxation of confined water.[62, 174-176]

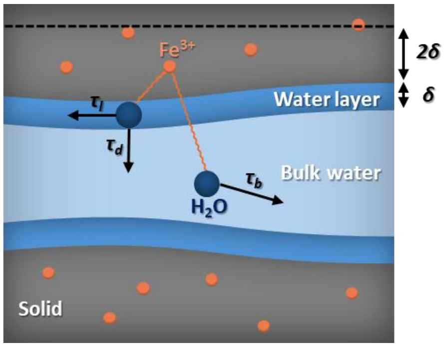

Figure 17. Schematic representation of the interactions considered in the 3-Tau model.[62, 175]

In this three-phase system (see in **Figure 17**) three types of water movement can be distinguished:

I. Water may diffuse in the bulk phase with a characteristic diffusion correlation time constant (τ_b) defined by the bulk water diffusion coefficient (D_b) as: $D_b = {\delta^2}/{6\tau_b}$ where δ is the thickness of a "layer" of water.[62, 174-176]

II. Water can also diffuse in the surface water layer, parallel to the surface with characteristic diffusion time correlation constant (τ_l) defined as: $D_l = {\delta^2}/{6\tau_l}$ where D_l is the diffusion coefficient of water in the surface layer with δ thickness.[62, 174-176]

III. Water molecules may also adsorb- desorb on the solid surface, which process can be described by the desorption time (τ_d) referring to the time water molecules spend on the surface before desorption with the assumption of the molecules desorb as $exp\left(-{t}/{\tau_d}\right)$.[62, 174-176] The value of τ_d depends on the strength of the solid surface-water interaction and increases proportionally to the strength of the interaction.[62]

These displacements of water molecules modulate the dipolar interaction between the electronic spins of the paramagnetic ions (Fe^{3+}) and the nuclear spins of water.[62, 174-176] Thus, the three defined time constants (*3-Tau:* τ_b, τ_l, τ_d) may strongly influence the longitudinal relaxation process (T_1) of confined water:

$$\frac{1}{T_1(\omega)} = f\left(\tau_l, \tau_b, \tau_d, N_{para}, \frac{S\delta}{V}\right) \qquad (13)$$

where N_{para} is the number density of the paramagnetic ions within 2δ depth in the solid matrix and $S\delta/V$ is the ratio between the volume of the surface layer (S – surface area) and the pore volume (*V*).[62, 174-176] With the assumption of planar pore geometry, the size of the planar pores can be calculated from $S\delta/V$.[62] The following parameters were extracted from the evaluation of the dispersion curves: τ_b – bulk diffusion time, τ_l – surface diffusion time, τ_d – desorption time, N_{para} – number density of the paramagnetic ions, $S\delta/V$ – surface layer volume to pore volume.[176] After a few iterations, it was clear that the value of τ_b can be kept constant ($\tau_b = 23.7$ ps), which is slightly longer than that of pure water ($\tau_b = 5.3$ ps).[62, 176] This may be explained by the presence of dissolved ions in cement pastes or the appearance of a second hydration layer. [62, 176] **Figure A3** in the *Appendix* shows a fitted dispersion curve, while the further curves were evaluated with the same settings.

The first part of the dispersion curves at low frequencies (~10^{-2} - 10^{-1} MHz) was sensitive to τ_l and the S/V ratio. The latter had a greater impact on the initial part of the curve. This influence can be seen in the changes of the T_2 relaxation time during the early hydration, since the value of T_2 also highly depends on the S/V (see in **Figure 14**). The effect of additives is interpreted based on the changes found in the extracted and derived parameters.

The variation of τ_d and τ_l over the cement hydration in the different cement composites indicates the pozzolanic effect of the additives compared to pure cement, as **Figure 18** shows. While both τ_d (from 5.62 µs to 0.67 µs) and τ_l (from 0.49 µs to 0.1 µs) show a quasi-decrease for pure cement, their values slowly increase or stagnate for Mc20 and Fc20. τ_l is sensitive to the slope of the dispersion curve, which does not change significantly until 70 min for Mc20 and 180 min for Fc20 (see in **Figure 16**), thus the value of τ_l stagnates.

The diversion between cement and the composites can be explained by the difference in the weight of the dissolution and precipitation processes in the early hydration, or by the dissimilar size and reactive surface area of the solid particles.[177] The concentration of the ions in the pore solution and the area of the solid- solution interface highly affects the rate of the dissolution and precipitation processes.[177] The dissolution of C_3S slows down, as the concentration of the solvated ion increases, and when the concentration of Ca^{2+} ions in solution is high enough, the precipitation of portlandite, then CSH begins.[62, 177] Since the substitution of cement with pozzolans increases the *w/c* ratio, meaning the amount of water available for cement hydration increases, the supersaturation of the pore solution, thus the precipitation of hydration products is prolonged.[177]

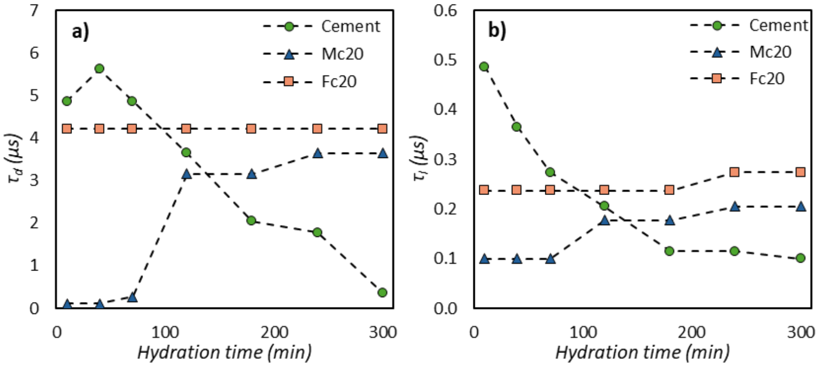

Figure 18. a) Desorption time (τ_d) and **b)** surface diffusion time(τ_l) of water during the early hydration of the studied samples: Portland cement (green circle), Mc20 (blue triangle) and Fc20 (orange cube).

Another parameter affecting τ_d and τ_l is the heat evolution during the early hydration of the cementitious materials, since it affects the temperature of the solid surface, thus the rate of desorption.[177, 178] Frías et al. found that the hydration heat sightly increased during the first hours of the hydration for metakaolin blended mortars compared to pure cement, while it proportionally decreased with increasing degree of substitution for the fly ash blends due to the filler/ dilution effect also seen by Moghaddam et al.[155, 179] Although, this process is more complex, since beyond the heat evolution the quality and also the area of the solid surface changes.

In summary, the change in τ_d for pure cement over time can be explicated as: in the initial dissolution period (*I*) τ_d slightly increases (from 4.87 µs to 5.62 µs) as the rate of dissolution decreases, then after the supersaturation of the pore solution, the heat released by the precipitation of the hydration products decreases τ_d. For Mc20 and Fc20, similar changes occur, but with a time delay, depending on the length of the induction period affected by the pozzolans. The initial value of τ_d and τ_l (at $t = 10$ min) is lower for the composites compared to cement, which may be owned to the higher heat evolution during the early hydration, shortening the time water molecules stay adsorbed to the surface and in the surface layer. The comparison of τ_d and τ_l of the three samples at $t = 300$ min gives information about the strength of the interaction between the solid surface and the water molecules. Both time constants show a similar trend, the strength of the water- solid interaction increases as: cement < Mc20 < Fc20, indicating that the fly ash composite strongly bounds water.

The diffusion coefficients (D_l) of water in the surface layer calculated from τ_l are summarized in **Table 4**. A similar order of magnitude value was found by Rusu et al. in white OPC paste: $D_l = 5.06 \times 10^{-14}$ m^2/s.[62] In case of pure cement, the weakening water- solid interaction is also observable in the increasing D_l values over time.

Table 4.: Diffusion coefficients of water in the surface water layer over the early hydration of the cementitious samples.

D_l (m^2/s) ^{a}							
t_h (min) ^{b}	10	40	70	120	180	240	300
Cement	2.49E-14	3.33E-14	4.43E-14	5.93E-14	1.06E-13	1.06E-13	1.22E-13
Mc20	1.22E-13	1.22E-13	1.22E-13	6.83E-14	6.83E-14	5.93E-14	5.93E-14
Fc20	5.13E-14	5.13E-14	5.13E-14	5.13E-14	5.13E-14	4.43E-14	4.43E-14

^{a} Surface diffusion coefficient. ^{b} Hydration time.

The number density of paramagnetic ions (N_{para}) in the three samples over the early hydration (shown in **Figure 19a**) also showed the dissimilar effect of pozzolans: a) on the initial value of N_{para} and b*)* on the time when N_{para} begins to increase, thus the end of the induction period (*II*) of cement hydration.

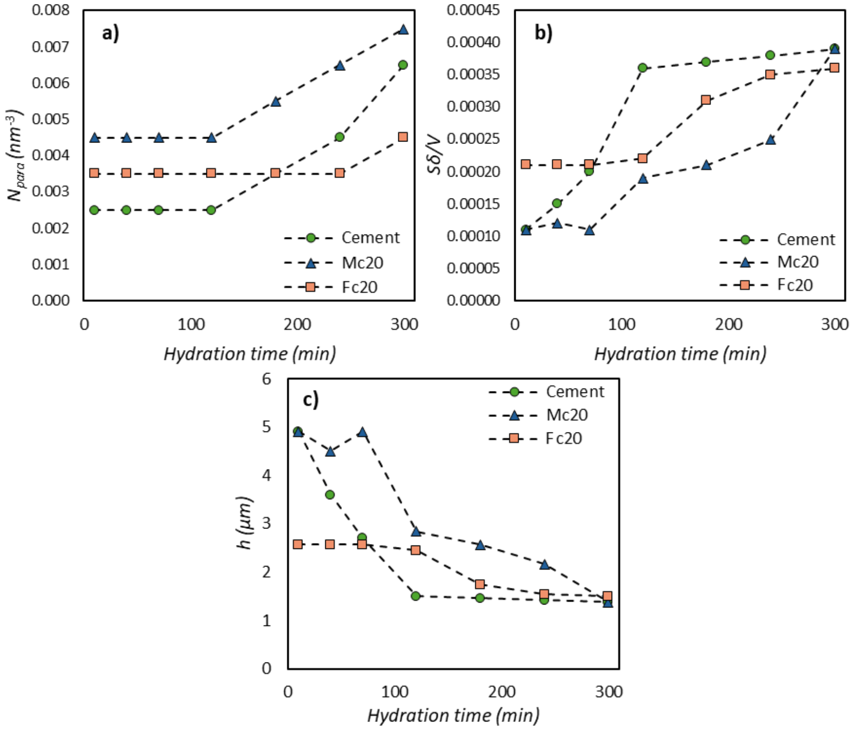

Figure 19. The change of **a)** the number density of the paramagnetic ions (N_{para}), **b)** the surface layer volume to pore volume (*Sδ/V*) and **c)** the size of the planar pores (*h*) during early hydration. The samples investigated are indicated in the legend.

In this period, the formation of a protective membrane/ layer of hydration products on the surface of the cement grains hinders the interaction of bulk water and anhydrous cement. The thickness of the protective membrane inversely influences the strengths of the interaction and the perceptible effective ion density according to Rusu et al.[62]

Considering the three investigated samples, the thickness of the protective layer is the highest for pure cement ($N_{para} = 2.5 \times 10^{-3}$ spins/nm^3) and the lowest for the metakaolin containing sample ($N_{para} = 4.5 \times 10^{-3}$ spins/nm^3). As the induction period ends and the protective layer ruptures, the precipitation of CSH begins, increasing the perceptible effective ion density.

The last fitted parameters are the surface layer volume to pore volume ratio ($S\delta/V$) and the derived size of the assumed planar pores (h) shown in **Figure 19b-c**. The precipitation of the hydration products involves the formation of new surfaces and the filling of available, micrometer sized pore spaces decreasing its volume and size. The speed of these processes increased as: Fc20 < Mc20 < cement, as expected based on the pozzolanic properties of the additives.

Effect of pozzolans on the hardened pore structure

During the hydration process various hydration products precipitate and form a heterogenous solid matrix, which has two significant roles in radioactive waste management: a) hydration products as sorbing minerals can immobilize radionuclides and b) the solid matrix can hinder the diffusion of both the radionuclides and water molecules.[28] In the following, the structural characterization of the hardened cement composites and the structure- modifying effect of the metakaolin and fly ash will be described in detail. Both samples were investigated in dry state by SEM and N_2 gas porosimetry and in aqueous environment by 1D and 2D NMR relaxometry. The SEM images show the macroscopic structure of the studied cement samples (see in **Figure 20**). As detailed previously, the mineral composition of the hardened material is highly influenced by the degree of substitution of cement with pozzolans: the amount of portlandite and ettringite decreases, while that of the CSH gel and the other aluminum containing minor phases increase.[154, 180] Among these minerals, the spite-like calcium- silicate hydrate (CSH), the needle-like ettringite (E) and the plate-like shaped portlandite (CH) can be observed with high certainty on **Figure 20**. The contribution of CSH gel increases, while that of ettringite slightly decreases as the pozzolan content increases. The structural compactness of the composites with high pozzolan content increased, due to the formation of excess hydration products in the pozzolanic reactions. The highest compactness is observable in the Mc20 sample. In case of the fly ash composites spherical, micro-sized (1-6 µm) fly ash particles (FA) can be observed, the surface of which is covered with thin layers of hydration products.[180] These particles increased the heterogeneity and the macroporous features of the solid matrix. Overall, in the metakaolin composites a more homogeneous and contiguous solid matrix formed compared to the fly ash composites, where more macroscopic voids were visible.

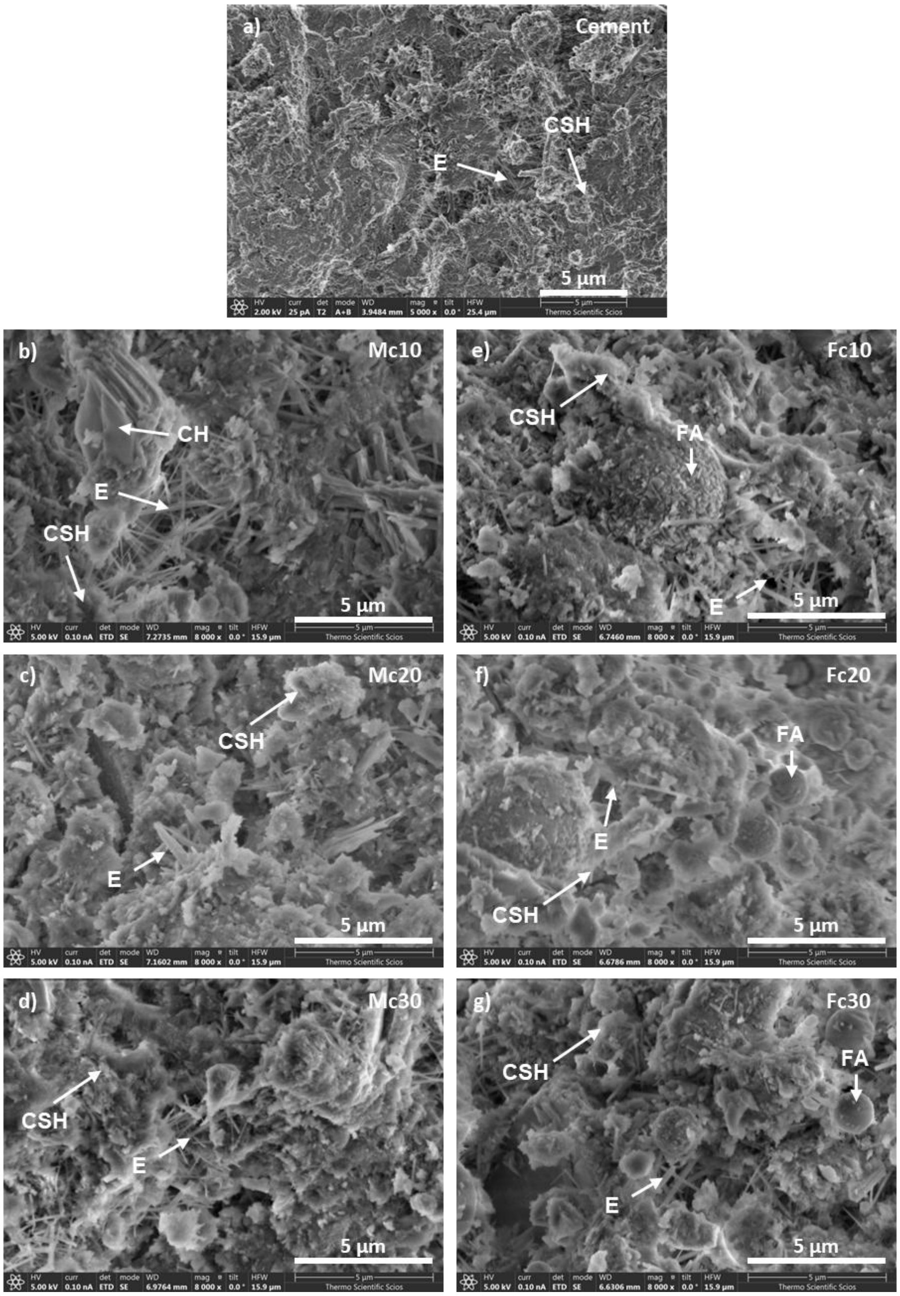

Figure 20. Scanning electron microscopy images of **a)** pure Portland cement, 10-30% **b-d)** metakaolin and **e-g)** fly ash containing cement composites showing the characteristic hydration products and the remaining pozzolanic additives. (CSH- calcium silicate hydrate, CH- portlandite, E- ettringite, FA- fly ash).

The micro- and mesoscale structure of the cement composite samples was studied in dry state by N_2 porosimetry and compared to pure cement, the N_2 sorption isotherm of which was detailed in *Section 5.1.1.* The N_2 sorption isotherms of the composite samples are shown in **Figure 21.a, b**, and can be classified similarly to cement as *IVa* – II transition type with an *H3* like hysteresis loop. [54] The increase in the pozzolan content of the composite decreased the detectable pore volume, indicated by the downward shift of the isotherms.

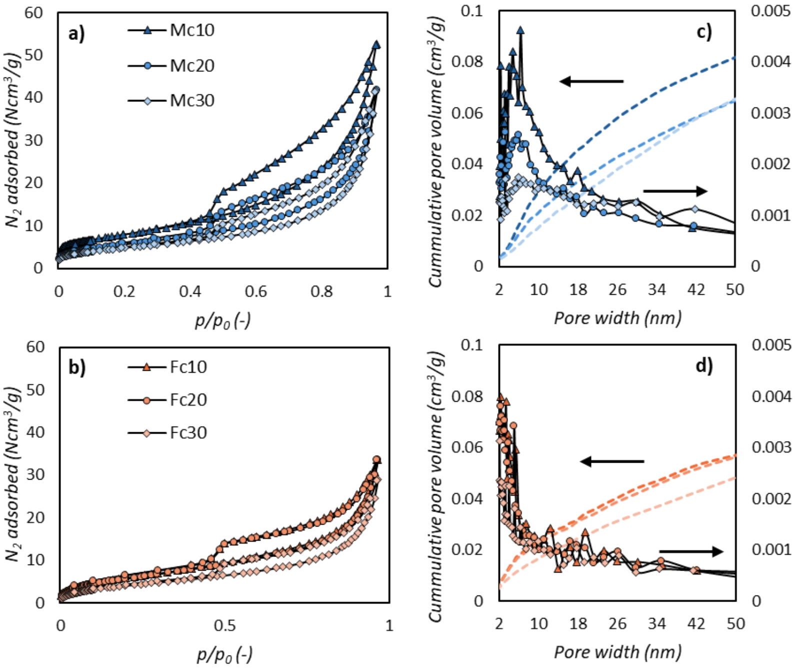

Figure 21. Low temperature nitrogen adsorption isotherms of **a)** 10-30% metakaolin and **b)** 10-30% fly ash cement composites. The derived cumulative pore volumes (left axis, dashed line) and pore size distributions (right axis, symbol and line) of **c)** the metakaolin and **d)** fly ash composites.

The parameters extracted from the various models fitted on the isotherms are summarized in **Table 5** alongside the data of pure cement. In the case of metakaolin composites the determined "total", micro- and meso- pore volumes show a decreasing trend with increasing metakaolin substitution in comparison to pure cement. This change reflects the macroscale compactness observed on the SEM images. In the case of fly composites, only the micropore volume decreases with increasing fly ash content. The mesopore volume shows a slight increase, causing the increase of the "total" pore volume as well.

Table 5.: Surface areas and pore volumes of Portland cement and the pozzolan containing composites deduced from nitrogen absorption.

Sample	S_{BET} *(m²/g)* [a]	V_{micro} *(cm³/g)* [b]	$V_{0.95}$ *(cm³/g)* [c]	V_{meso} *(cm³/g)* [d]
Cement	23	0.0081	0.057	0.049
Mc10	29	0.0108	0.068	0.057
Mc20	21	0.0070	0.050	0.043
Mc30	18	0.0061	0.049	0.043
Fc10	23	0.0073	0.034	0.027
Fc20	22	0.0072	0.042	0.035
Fc30	16	0.0055	0.043	0.038

[a] Surface area from BET model., [b] Micropore volume from DR plot., [c] Pore volume at p/p_0 = 0.95., [d] Mesopore volume ($V_{0.95} - V_{micro}$).

The surface area of the samples, except for Mc10, decreases with the degree of pozzolan substitution compared to cement. Both the $V_{0.95}$ and the S_{BET} are the lowest in the fly ash composites. The dissimilarities may be owed to the different pozzolan activities of the additives, which cause the formation of CSH gel to various extents, where pores with non-evaporable water are present inaccessible to nitrogen gas. The pore size distribution (see in **Figure 21c, d**) resulted from the fitting of the adsorption branch of the isotherm (BJH model) is reliable in the mesopore size range (2 nm < d < 50nm). For the metakaolin composites, the maximum of the pore size distributions is d ~7 nm, similar to pure cement, with a wide distribution over the mesopore size range. Contrary, in fly ash composites the d~ 2 nm sized pores dominate, with a narrow size distribution, showing the superiority of the micropores and small mesopores.

Henceforward, the micro-, meso- and macroporous structure of the cement samples were studied in aqueous state by 1D and 2D NMR relaxometry, since the knowledge of the wet pore structure and the behavior of cement composites in aqueous environment is indispensable from the viewpoint of the intended application.[3] In the 1D NMR relaxometry measurement, the porous structure was studied through the T_2 transverse relaxation process of confined water, as described earlier (see in *Section 5.1.1).* The resulting T_2 relaxation time distribution curves of the pozzolan containing cement composites are shown in **Figure 22b** and were compared to pure cement as a reference (see in **Figure 22a**).

The characteristic pore types in cement could be assigned to each water domain as follows: *1.* bound water in the intra CSH layer pores ($T_2 < 1$ ms, marked with blue on **Figure 22a,b**), *2.* slightly more mobile water in the inter CSH gel pores (1 ms < T_2 < 5 ms, marked with orange) and *3.* mobile water in capillary pores with various sizes ($T_2 > 5$ ms). The pore types were identified based on the relaxation time ranges estimated from the characteristic pore sizes known from literature. [58, 88, 95]

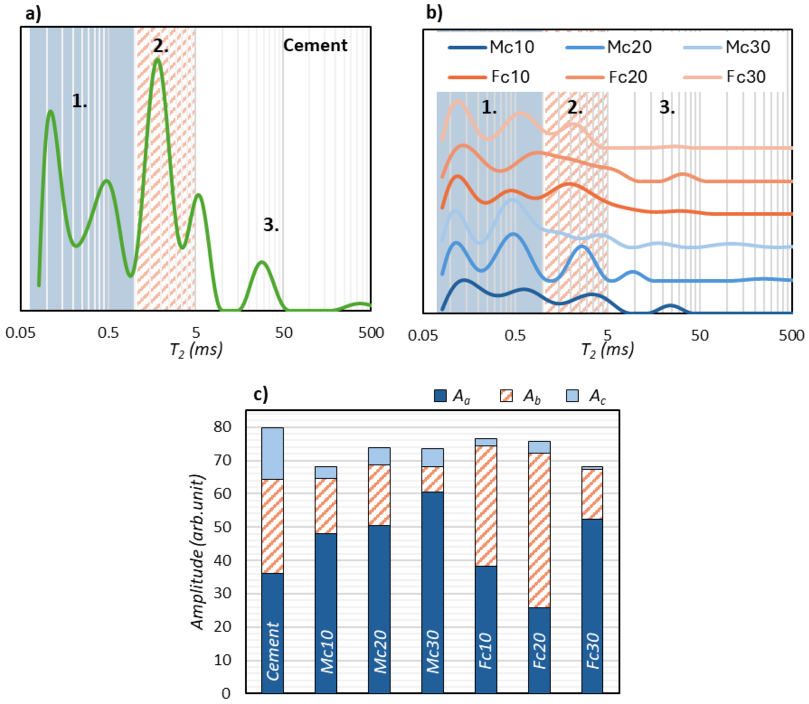

Figure 22. T_2 relaxation time distribution in **a)** pure Portland cement and **b)** 10-30% metakaolin (Mc10-30, blue) and fly ash (Fc10-30, orange) containing cement composites with the identified pore types (1- intra CSH sheet pore, 2- inter CSH gel pore, 3- capillary pore). **c)** The effect of pozzolans on the amplitude of water in different pores.

Comparing the T_2 distributions of the pozzolan substituted composites and pure cement, two minor differences can be observed: *a)* the contribution of bound water types somewhat increases and *b)* the presence of the pozzolans caused the merging of some of the relaxation domains characteristic for cement (see in **Figure 22a, b**). The first one is more prominent in the change of the amplitudes of the T_2 peaks assigned to the pores, as **Figure 22c** shows. The addition of metakaolin (Mc10-30) increased the contribution of the CSH sheet and gel pores (A_{a-b}), while the ratio of capillary pores (A_c) decreased from 15% to 5% in the case of Mc10-30 compared to pure cement.

Fly ash (Fc10-30) increased the influence of the CHS sheet and gel pore to a slightly greater extent than metakaolin. However, while in case of the Mc series mainly the contribution of the CSH sheet pores increased, fly ash influenced mostly the CSH gel pores. The ratio of capillary pores decreased to ~ 2% for Fc10 and Fc30. It has to be noted that this method is less sensitive to large capillary pores, due to the low influence of the pore wall, thus it may underestimate the presence of large pores.

The T_2 distribution shows that the additives do not affect significantly the size of the pore, but rather their ratios. This was also observable on the 2D T_1-T_2 relaxation correlation maps, as shown in **Figure 23**, which provides information on the exchange processes between the individual water types and the permeability of the pores.[59, 63, 65] Based on the rotational correlation time (τ_c) dependence of the T_1 and T_2 relaxation times, the two relaxation processes can remarkably differ for chemically or physically bound hydrogens and hydrogens in more mobile water filling small pores. According to McDonald et al., the T_1 relaxation time is long (> 100 ms), but T_2 is short (~ 0.01 ms) for chemically bound water in the CSH sheet pores.[59] While for the CSH gel pores, where water movements are less hindered, and the relaxing effect of the surface is not negligible, both relaxation time constants are short. The effect of the surface is decreased by increasing pore sizes, which prolongs the T_1 and T_2 relaxation of water in the capillary pores.[59, 63]

The diagonal of the 2D correlation maps shows the water domains (signed with numbers in Figure **23**) identified on the 1D T_2 distributions (Figure **22**) reflecting the pore types of cement. The position of the peaks is similar for pure cement and the metakaolin composite, while it shifts to shorter relaxation times for the fly ash composite. The intensity of the peaks assigned to the CSH gel, especially for Fc20, is enhanced by the presence of pozzolans.

The additional information which can be obtained from the T_1-T_2 correlation maps is the location of the diagonal peaks compared to the principal diagonal ($T_1 = T_2$) marked with solid line in **Figure 23**. In the case of pure cement and Mc20, the diagonal features of the peaks slightly shift to $T_1 = 2T_2$ (dashed line), and to $T_1 = 4T_2$ (dotted line) in the case of Fc20. McDonald et al. also found such features in cementitious materials and interpreted them by the different surface diffusion correlation (τ_m) and surface residence times (τ_s) of water in the solid according to the surface diffusion model of relaxation.[59, 64, 65] For $T_1=2T_2$ the ratio of these time constants is $\tau_m/\tau_s \approx 10^{-2}$, while it is $\tau_m/\tau_s \approx 10^{-4}$ for $T_1=4T_2$. The reciprocal value of them (τ_s/τ_m) indicates the "affinity" of the surface to the solvent.[59, 181] Similarly to the

τ_d and τ_l values found by FFC NMR, here τ_s and τ_m also refer to a strong interaction between the water molecules and Fc20.

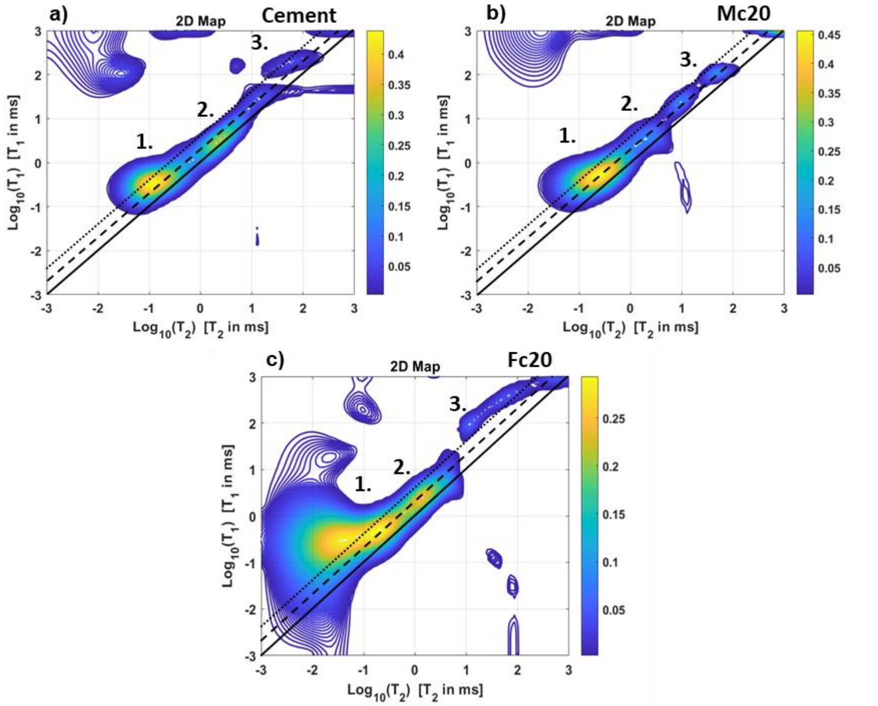

Figure 23. 2D T_1-T_2 relaxation correlation maps of **a)** pure Portland cement, **b)** 20% metakaolin (Mc20) and **c)** 20% fly ash (Fc20) containing cement composites with the characteristic pore types in the diagonal (1- intra CSH sheet pore, 2- inter CSH gel pore, 3- capillary pore). The dashed ($T_1=2T_2$) and dotted ($T_1=4T_2$) lines show the shifted principal diagonal.

The extent of the separation of the peaks indicates the permeability between water domains; in Mc20 the peaks are more separated, compared to the other samples, meaning that water is found in different environments and the pore structure is less open.[59, 94] Peaks are also visible away from the principal diagonal (off- diagonal peaks), which can be construed in two ways:

- if there is a great difference between the relaxation times ($T_1 >> T_2$) the off-diagonal peak can be ascribed to hydrogens in a solid-like environment, chemically bound in the CSH gel.[59]
- if the difference is smaller ($T_1 > T_2$), and the off- diagonal cross peak appears in the 2D T_2-T_2 correlation maps as well, then chemical exchange takes place between the pore types.[59, 65]

McDonald et al. assigned the cross peaks in the upper left corner of the 2D T_1-T_2 correlation maps to the chemical exchange between the CSH gel pores (1,2) and the capillary pores (3).[59, 64, 65] Based on this, the cross peaks found in our case were also considered as results of exchange processes and it is clearly visible that the addition of the pozzolans reduced them.

Effect of pozzolans on restricted diffusion of water in cement

After the comprehensive structural characterization of pozzolan containing cement composites, the diffusion of water was followed within the solid matrices. Knowing how the solid structure inhibits the diffusion of water is essential regarding radioactive waste management, since it determines the leaching of radionuclides from the waste forms. The self- diffusion of liquids in porous materials is commonly measured by PGSE NMR, using gradient pulses, however, if the T_1 and T_2 relaxation processes of confined water are significantly accelerated (e.g. due to the presence of magnetic inhomogeneities or small pore sizes), it is not applicable. The so-called H_2O–D_2O exchange diffusion technique can be suitable for testing such materials, since it follows the H_2O proton signal decrease within the solid as it exchanges with D_2O.[60, 66, 67] The proton signal intensity decay curves are shown in **Figure 24**.

If we compare the exponential intensity decay curves, two conspicuous differences are observable: *I*) the decay process itself (course of the curve) and *II*) the residual signal intensity.

I. The pozzolan substitution significantly influenced the rate of water signal decay, while in pure cement the water signal intensity decreased to ~23% of the initial value in 24 hours, that of the metakaolin composites decreased to Mc10: 23%, Mc20: 52%, Mc30: 41% (see in **Figure 24**, indicated with dashed line). Thus, at high metakaolin content (20-30%), the water signal intensity change is slower. For the fly ash composites, the water signal intensity decay curve completely subsided until 24 hours, and intensities reached a stable value: Fc10: 31%, Fc20: 34%, Fc30: 57% of the initial value. The diffusion process is more elongated for the metakaolin series (Mc20-30) compared to the other two, and the degree of elongation depends highly on the metakaolin content indicating the increasingly inhibited movement of water due to the precipitation of additional hydration products.
II. The addition of pozzolans also affected the residual signal intensity at the end of the diffusion process. It is especially visible in the case of fly ash composites, and the amount of it increases with the degree of substitution. The residual signal intensity can be attributed to the bound, non- or very slowly diffusing water within the sample. The high contribution of strongly bound water in the

fly ash series was already seen on the 1D T_2 distributions and on the 2D T_1-T_2 correlation map of Fc20.

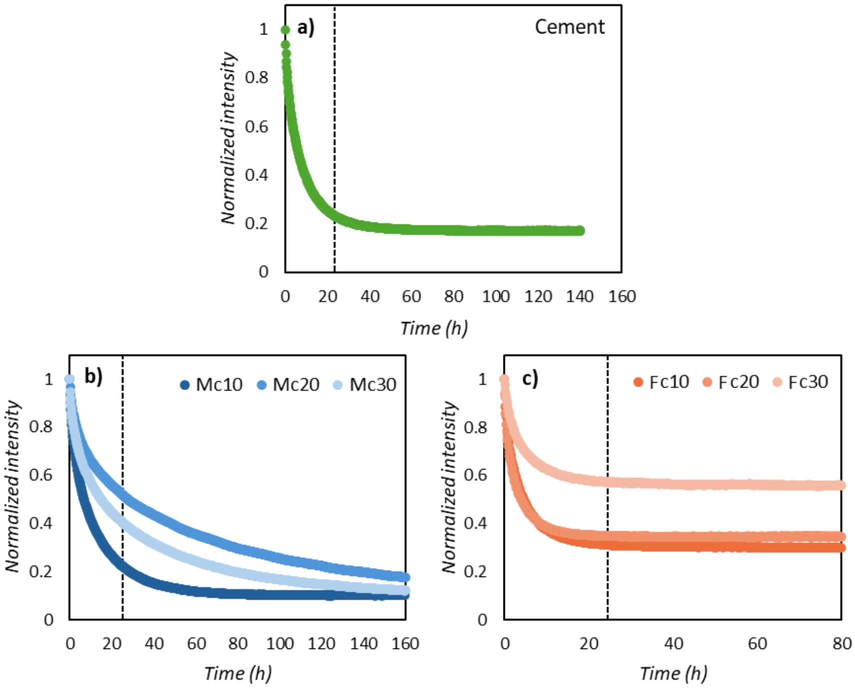

Figure 24. The normalized intensity of the proton signal over time in **a)** pure Portland cement, **b)** 10-30% metakaolin and **c)** 10-30% fly ash containing cement composites. The dashed line indicates $t = 24$ h, where the samples were compared.

The diffusion coefficients of water were determined by fitting the obtained decay curves with the mathematical model derived by J. Crank[115], which includes the diffusion processes in an infinite cylinder (C_{cyl}) and in a plane sheet (C_{ps}), as the product of two exponentials:

$$C^* = \frac{M(t)-M(t=\infty)}{M(t=0)-M(t=\infty)} = C_{ps}C_{cyl} \tag{14}$$

$$C_{ps} = \sum_{n=0}^{\infty} \frac{2\alpha(1+\alpha)}{1+\alpha+\alpha^2 p_n^2} exp\left(-D_p p_n^2 \frac{t}{l^2}\right) \tag{15}$$

$$C_{cyl} = \sum_{n=0}^{\infty} \frac{4\alpha(1+\alpha)}{4+4\alpha+\alpha^2 p_n^2} exp\left(-D_p p_n^2 \frac{t}{r^2}\right) \tag{16}$$

where C^* is the change in the concentration of light water, M is the measured signal intensity, α is the volume ratio of heavy to light water, D_p is the diffusion coefficient of water, p_n is the square root of the error function, r and l are the radius and length of the cylinder respectively, while t is the duration of the measurement.[66, 115] The best fittings were achieved by using the product of two (cement) and three exponential sums (pozzolan containing ones). The determined diffusion coefficients with their errors (less than 10%) are shown in **Figure 25** and are numerically summarized in **Table A1** in the *Appendix*.

All the determined diffusion coefficients were much lower than the value assigned to free water (D= 2.3 × 10^{-9} m^2/s)[114] referring to strongly restricted water diffusion processes. The following diffusion coefficients of water were found in pure Portland cement: D_1= 1.0 × 10^{-10} m^2/s and D_2= 3.6 × 10^{-12} m^2/s. Comparable values were observed by Fleury et al. for pure cement.[67] The faster diffusion (D_1) may take place in the larger capillary pores, while the slower diffusion (D_2) may be contributed to the swollen CSH gel, in which water movement is restricted.

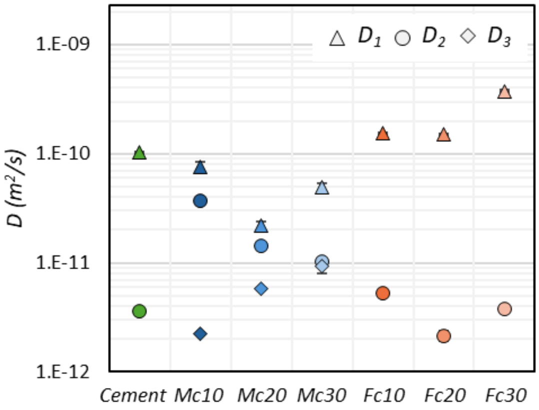

Figure 25. The self- diffusion coefficients (D_{1-3}) of water in pure Portland cement (green), 10-30% metakaolin (blue) and 10-30% fly ash (orange) containing composites. The errors of the fitted D values are also indicated.

In the metakaolin composites three diffusion coefficients could be differentiated: $D_{1,2}$ = 1.0 × 10^{-11} - 7.5 × 10^{-11} m^2/s and D_3 = 2.2 × 10^{-12} – 9.4 × 10^{-12} m^2/s. Comparing the diffusion coefficient of water in the capillary pores in pure cement and the metakaolin composites, it is observable that water diffuses an order of magnitude slower in the composite samples. In the fly ash composites, also two restricted water diffusion processes could be distinguished: D_1 = 1.5 × 10^{-10} – 3.7 × 10^{-10} m^2/s and D_2 = 2.2 × 10^{-12} – 5.3 × 10^{-12} m^2/s. The diffusion of water in the fly ash composites is similar to that in pure cement, however due to the presence of macro voids seen on the SEM images the diffusion in the capillary pores is less restricted. Based on the derived diffusion coefficients, the 20% metakaolin substitution of cement seems to be the most promising composition from the viewpoint of water mobility.

Regarding the aimed application of the cement matrix, the substitution of cement with 20% metakaolin resulted in the most promising binder for the long-term safe disposal of radioactive waste. Thus, we continued working with that composite and investigated how the model radioactive liquid waste affects the solid matrix, which will be presented in *Section 5.2.1*.

5.2. The impact of real waste management conditions

5.2.1. Effect of complexing agents

The aim of radioactive waste solidification is to immobilize the hazardous radionuclides and to minimize their potential for migration and dispersion in the environment.[3] During the cementation of LLW and ILW, the hydrate phases of cement are capable of the sorption of radionuclides, while its porous structure restricts their migration, rendering cement to a chemical and physical barrier.[3, 32, 33] However, the composition and porous structure, thus the retention capacity of cement for certain radionuclides is highly sensitive to any form of added components and their interaction with cement.[3, 182] Beyond organic compounds and acids (e.g. hydroxycarboxylic acids, carbohydrates, phosphonates), several inorganic substances (e.g. borates, phosphates and other salts) can retard the hydration process and/or pore structure formation of cement.[3, 32, 182-184] These compounds are present in low and intermediate-level liquid radioactive waste (LLW and ILW) as radionuclides and chelating/ complexing agents.

In this section, the investigation of the leachability and structure of cemented model waste packages will be presented, which were prepared based on the recipe for the cementation of LLW and ILW waste at Paks NPP in Hungary, with the permission of PURAM. The model waste packages simulated the real solidified radioactive waste forms, containing complexing agents at various concentrations (0-20 g/l) and isotope analogue model ions.

The aim of this chapter of my PhD research was to determine the effect of the complexing agent content on the leachability of the model waste packages (regarding: ^{60}Ni, ^{133}Cs, ^{185}Re, organic carbon), as well as to study their effect on the structure of the cement. Furthermore, since small size samples, suitable for the NMR experiments, were used in our work, the effect of the sample size was also studied by the comparison of our leachability results with previous experiments carried out on larger samples.

To examine the leaching behavior of Cs, Ni and Re from the waste packages, accelerated leaching tests were performed according to ASTM C 1308-08 Standard, and the model ion content of the leachates were analyzed by ICP MS.[117] The organic carbon content of the leachates in case of the 5 and 20 g/l complexing agent containing samples were studied by HF- NMR methods. To investigate the structure and permeability of the model waste packages, the above-mentioned (*Section 5.1.2*) techniques were used (SEM, NMR relaxometry, 2D T_1-T_2 correlation NMR relaxometry, H_2O-D_2O exchange diffusion measurements). The overall goal was to thoroughly evaluate the leaching behavior and permeability of potentially usable waste packages and to propose an applicable complexing agent concentration range for the long-term performance of the waste packages.

Leachability of the model waste packages- Leaching of ^{133}Cs, ^{60}Ni and ^{185}Re

The effect of complexing agent concentration on the leaching behavior of Cs, Ni, and Re from cylindrical, 20% metakaolin containing cemented model waste packages was investigated. The leaching of the model ions from the small sized samples was carried out based on the ASTM C 1308-08 Standard and was compared to previous results on samples with larger size.[117] The incremental fraction leached (*IFL*) values of each model ion were determined from the ratio of the amount of model ions in the leachates determined by ICP-MS analysis (ia_n) and the amount of model ions introduced during sample preparation (iA_0).[117] The cumulative fraction leached (*CFL*) resulted from summing the IFL values for each release time interval (*j*) as follows:[117]

$$CFL_j = \frac{\sum_{n=1}^{j} ia_n}{iA_0} = \sum_{n=1}^{j} IFL_j \qquad (17)$$

The calculated CFL values of Cs, Ni, and Re as a function of the leaching time (*t*) are shown in **Figure 26** on the same scale for comparability. After the prompt release of the model ions, the leaching process slows down, and the change of the CFL values over time shows saturation-like curves.

Comparing the resulting leaching curves, two main differences may be observed: *I)* the retention capacity of cement for the model ions and *II)* the impact of the complexing agents on the leaching process.

I) Regarding the retention capacity of the cement matrix for the model ions, the obtained CFL values of the three model ions were compared at the end point of the leaching process. The following trend was found relating to the leachability of the model ions: cesium> rhenium> nickel. During the leaching experiment almost 30-40% of the introduced cesium, 6-17% of rhenium and <2% of nickel leached out of the cemented matrix. A similar trend was found previously in the case of large sized samples, but for the small probes the leaching was enhanced due to the large *S/V* ratio of the cylinders. This tendency may be explained by the different behavior of the ion in cementitious environments and their interaction with the sorbing minerals of cement. One of the most cumbersome radionuclides to immobilize is cesium, which is soluble in the alkaline cementitious environment.[28, 185-187] Cesium occurs as Cs^+ in aqueous solutions; as an alkali metal it is less prone to sorb on the cement hydrates and has a low tendency for complex formation. [28, 186, 188, 189] Among the cement hydrates CSH tends to sorb cesium through ion exchange-type process; however, its efficiency highly depends on the presence and concentration of competing ions (Na, K, and Ca) and the charge of the interlayer CSH surface (Ca/Si ratio).[28, 187] Bagosi and Csetényi studied the sorption of cesium in hydrated cementitious assemblages through its distribution ratios (R_d).[188] They found that R_d increased with increasing Ca/Al ratio and decreased parallel with decreasing Si/Ca and Al/ Si ratios.[188] Thus, increasing the aluminum content of the CSH gel, e.g. by using aluminum-rich pozzolans, may enhance the sorption of cesium.[164, 187] Technetium, here modeled with rhenium, is a redox sensitive element, which is present as soluble TcO_4^- or Tc(IV) in cementitious environments, and the latter tends to form complexes.[28, 190, 191] The highly soluble oxo-anionic form of technetium may substitute sulfate in the sulphate- aluminate minerals of cement (Afm, Aft).[28, 192-194] These processes result in a lower leachability of technetium. Contrary to the former two, nickel forms low aqueous soluble nickel-aluminum layered double hydroxides (Ni-Al LDH) in the alkaline environment, and potentially also bound to chelating and complexing agents, leading to low leachability.[28, 195, 196]

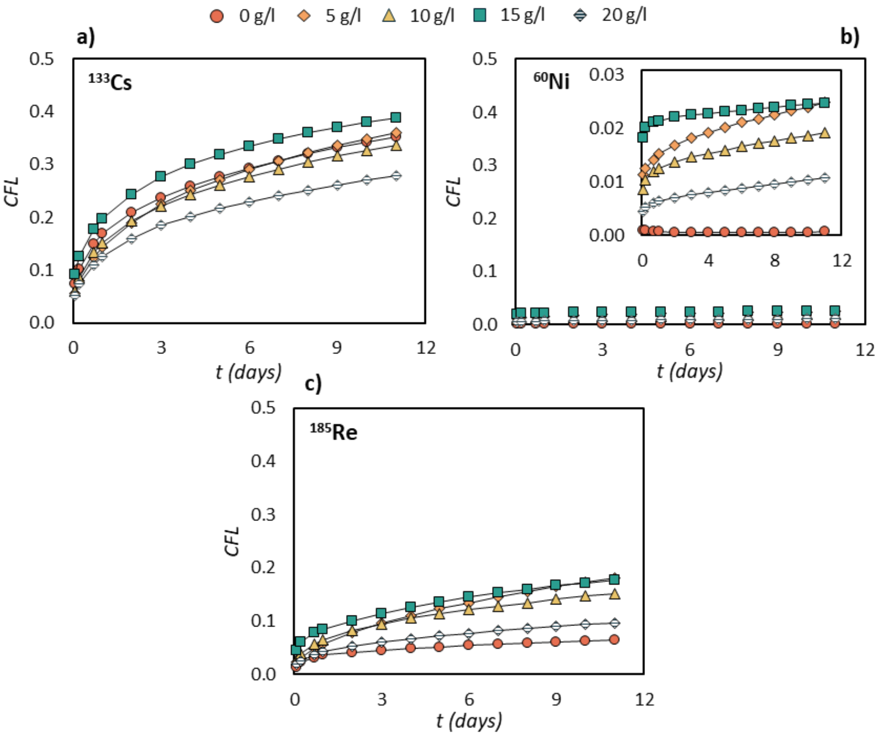

Figure 26. The obtained cumulative fraction leached (*CFL*) values in case of **a)** cesium, **b)** nickel and **c)** rhenium (technetium analogue) from the small sized model cemented waste packages. The complexing agent concentration varied between the samples (0-20 g/l), which is marked with different symbols and colors. The inserted figure serves to enlarge the curves in case of nickel. The solid line connecting the points is only to guide the eye.

II) The chelating/ complexing agent content of the liquid radioactive waste, particularly multidentate ligands, has a great effect on the immobilization of radionuclides. The impact of the total concentration of complexing agents (0-20 g/l, shown in **Figure 26** with different colors and symbols) was compared regarding the course and the end point of the curves. The first observation was that complexing agents not only affected the leaching of model ions prone to complex formation (Ni, Re), but also the release of cesium. The second observation was that the leachability of the ions did not change proportionally with the complexing agent concentration but followed more or less this trend: 0 and 20 g/l < 10 g/l < 5 and 15 g/l, meaning that at certain concentrations the leaching process is facilitated. According to Lövgren, the complexing agents may influence the sorption of radionuclides through the combined effect of the following enhancing and suppressing processes: a) formation of complexes in aqueous solution, b) formation of ternary complexes at the water/solid interface, c) competition for sorption sites, d) favorable change of solid surface charge for ion sorption, e) precipitation at the water/ solid interface.[197] Smillie and Glasser studied the possible interactions between Portland cement and complexing agents, namely oxalic acid, citric acid, and Na_2-EDTA.[198] They found that the quantity of solved oxalic acid and citric acid decreased in the pore water of cement, the former one possibly due to its transformation to low soluble calcium oxalate monohydrate.[198] It was also found that cement did not affect EDTA under these circumstances.[198] According to Guidone et al., citrate adsorbs quite strongly to the Afm and Aft hydration products in highly alkaline environments (pH= 13.2).[199] In summary, at certain concentrations (5 and 15 g/l) the combined enhancing and suppressing effects of complexing agents can result in enhanced model ion leaching processes.

The complexity of the single model ion leaching processes and the mutual influence of the ions on each other's leaching was studied by the fitting of the leaching curves with the following first- order kinetic equation by Nemes et al.:

$$X_e - X_t = Ae^{-kt} \qquad (18)$$

where X_e and X_t are the ratio of bound/leached ions in equilibrium and at t time respectively, A is a constant, k is the rate constant.[200] The fitted rate constants (k) and their errors (σ) are summarized in **Table A2** in the *Appendix*. The value of k varied between 0.21 - 0.31 day^{-1} at 298 K and showed no clear trend regarding the complexing agent concentration. The fit of the leaching curves to first-order kinetics showed that the leaching of the different model ions was dominated by their own solubility and the presence of the other ions did not affect significantly their leaching process.

According to the ASTM C1308-08 standard, if the leaching process of the model ion is mostly driven by mass diffusion, the effective diffusion coefficient of the ion can be derived from the fittings of the leaching curves with different models.[117] The effective diffusion coefficient (D_e) indicates the diffusivity of the model radionuclides influenced by the porous structure of the solid matrix and the possible interactions with the solid (e.g. adsorption, tortuosity of the matrix).[201, 202] Two models are usually used to extract D_e:

I. If $CFL<0.2$, then the solid matrix is considered as a semi- infinite medium and D_e can be calculated knowing the volume (V) and the surface area (S) of the cylindrical probe:[117]

$$CFL = \frac{\sum a_n}{A_0} = 2\frac{S}{V}\left[\frac{D_e t}{\pi}\right]^{1/2} \qquad (19)$$

II. If $CFL>0.2$, then the matrix is considered as a finite medium, and the depletion of the solid material due to leaching must be considered.[117, 203] In this case the following model defined by Pescatore can be used, which defines the time dependence of CFL by a double series expression:[204]

$$CFL = \frac{\sum a_n}{A_0} = 1 - \frac{32}{\pi^2}\, S_p(t) S_c(t) \qquad (20)$$

where S_p and S_c describe the diffusion process from the plane sheet and the cylinder.

Both models were used for the determination of effective diffusion coefficients of the model ions, and the fitted D_e values with the relative errors of the fittings (E_{R2}) are summarized in **Table A3-5** in the *Appendix*. If $E_{R2} \leq 0.5\%$, it means that the model precisely represents the data set according to the ASTM C1308-08 standard.[117] Contrary to the previously measured leaching experiment carried out on larger samples, the finite model better fitted the leaching curves of the small sized samples for each model ions and complexing agent concentrations. The determined D_e by the finite model in the small sized samples are shown in **Figure 27** and are compared to the ones previously determined in the large samples by the semi-infinite model. In the small probes, the D_e coefficients were in good agreement with the ones in the large probes and showed a quasi-decrease with increasing complexing agent concentration.

In the case of ^{133}Cs, the D_e varied between $1.3 \times 10^{-15} - 1.5 \times 10^{-13}$ m^2/s (*Appendix*, **Table A3**), indicating a highly restricted model ion diffusion compared to bulk water ($D = 2.3 \times 10^{-9}$ m^2/s).[114] Similar or somewhat higher diffusion coefficient values were found for cesium in Ordinary Portland cement: $D_e \sim 1.7\times 10^{-11} - 5.9\times 10^{-12}$ m^2/s, belite-rich cement: $D_e \sim 2.68\times 10^{-11} - 5.82\times 10^{-15}$ m^2/s, in zeolite- cement blends: $D_e \sim 5.7\times 10^{-12}$ m^2/s and also in EDTA containing cemented waste form: $D_e \sim 1.0\times 10^{-11} - 2.3\times 10^{-12}$ m^2/s.[42, 203, 205, 206] Two diffusion processes could be distinguished with the finite model for cesium: a quasi-fast ($D_e \sim 8.5 \times 10^{-14} - 1.5 \times 10^{-13}$ m^2/s) and a slow ($D_e \sim 1.3 \times 10^{-15} - 5.1 \times 10^{-15}$ m^2/s) one.

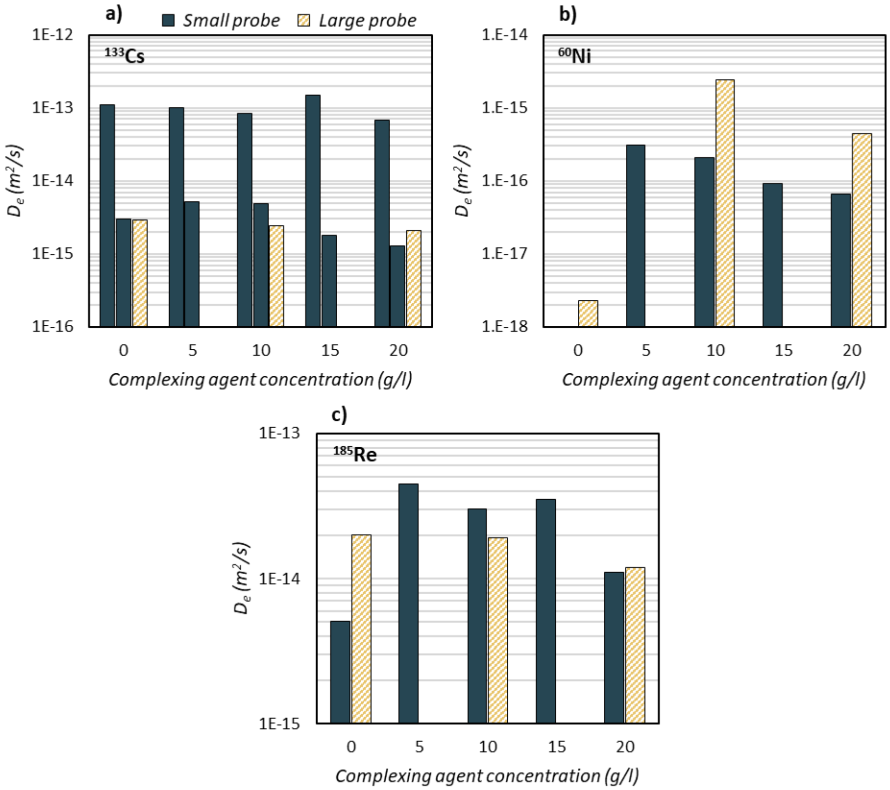

Figure 27. The determined effective diffusion coefficients (D_e) of **a)** cesium, **b)** nickel and **c)** rhenium (technetium analogue) from the small (green, full) and large (yellow, striped) sized model cemented waste packages.

The presence of a faster cesium diffusion may be explained on one hand by the high surface-to-volume ratio or the "skin effect" meaning a more pronounced leaching process from the surface of the small sized samples.[207] On the other hand, it can be interpreted by the presence of unbound ions, which may diffuse faster assumed by Zhu et al., who studied the leaching of cesium from alkali-activated cements and also found two distinct diffusion processes.[208] We found a slight decrease of the D_e values with increasing complexing agent concentration and a similar decrease was described in case of EDTA by Goo et al. They explained it by the possible competition between cesium and other metal-EDTA complexes and by the formation of a carbonated barrier induced by EDTA, which slowed down the diffusion of the ion.[42]

Contrary to cesium, only one diffusion process dominated the leaching of nickel and rhenium. In the case of ^{60}Ni, D_e varied in the range of $6.6 \times 10^{-17} - 3.1 \times 10^{-16}$ m^2/s (**Figure 27b** and **Table A4** in the *Appendix*) in the small sized samples with also a decreasing trend regarding the complexing agent concentration. Song et al. found D_e values of similar magnitude for nickel studying the leaching of different heavy metals from cemented sewage sludge. The diffusivity of nickel at pH 10 changed during the leaching process: it decreased from $D_e \sim 1.3 \times 10^{-16}$ m^2/s to $D_e \sim 7.8 \times 10^{-19}$ m^2/s after two days.[209] The determined effective diffusion coefficients of ^{185}Re (modeling technetium) changed between $5.1 \times 10^{-15} - 4.5 \times 10^{-14}$ m^2/s (**Figure 27c** and **Table A5** in the *Appendix*). Bourchy et al. compared the observed diffusivity (D_{obs}) of technetium over the history of cementitious waste forms developed for the application at the Hanford mission; the value of D_{obs} varied between $1\times 10^{-19} - 3\times 10^{-12}$ m^2/s.[190] The determined D_e values in our experiments fit well this range.

The decreasing trend in D_e with increasing complexing agent concentration, observed for all the three model ions, may be explained by the complex formation of the ions, the competition with other metals, the obstructing effect of the macromolecules (e.g. free complexing agents) or by a potential complexing agent-induced retardation barrier (e.g. calcite).[42]

Leachability of the model waste packages- Leaching of complexing agents

During nuclear decontamination operations complexing/chelating agents are usually used, since they can form strong and selective complexes with radionuclides.[210] Thus, these compounds are unavoidable components of liquid radioactive waste. However, despite cementation, the complexing agents may facilitate the migration of radionuclides from the repository, which could be possibly prevented by different pretreatment processes (e.g.: degradation), which in our case did not happen.[210] In the following, the characterization and identification of the organic compound content of the leachates in the case of 5 g/l and 20 g/l complexing agent containing samples will be presented through the results of the HF-NMR measurements (^1H-NMR, DOSY, HMBC, HSQC). The leachate of the samples was lyophilized and dissolved in D_2O to enhance the detectability of the organic compounds. As mentioned above, citrate and oxalate mainly precipitate or adsorb inside the cement structure, while EDTA may leach out in the form of metal complexes.[198, 199] Based on these, the presence of EDTA, and perhaps citrate complexes were expected in the leachate. As the carboxyl proton of oxalic acid rapidly exchanged with deuterium or hydrogen in HOD, it had no detectable proton signal. These were not the only source of organic compounds, since Ni was added in its acetate form, so we had to take it into account as well. The chemical structures of the used complexing agents are shown in the *Appendix* (see in **Figure A4**).

Figure 27 shows the ^{1}H NMR spectrum of the leachate of the 5 g/l sample. The complexity of the spectrum implies that numerous forms of EDTA- and citrate-complexes or their derivatives might be present in the leachate. Several peaks can be observed between 3 and 4 ppm, coupling to carbons with chemical shifts between 60 - 85 ppm (HSQC spectrum, see **Figure A5** in the *Appendix*). At first glance, these protons might be methylene groups close to the nitrogen atoms and the carboxyl groups of EDTA (marked with blue). The high intensity peak at δ= 1.8 ppm can be assigned to the methyl group of acetate ions (marked with red) deriving from the added Ni-acetate. Further high intensity ^{1}H peaks appear at lower chemical shifts in the form of triplets, or quartets; some of them show scalar coupling in the COSY spectrum (see **Figure A6** in the *Appendix*) with protons from the 3-4 ppm region. Some of them are spin systems of several protons. Furthermore, high-intensity peaks can be observed in the aromatic region (see in **Figure 28b**) around 7.3 ppm, belonging to aromatic protons or protons attached to carbon involved in a double bond. These observations point far beyond the expected simple complexes; thus, the explanation needs deeper insight into the chemistry of metal complexes and the potential interactions in the cementitious environment.

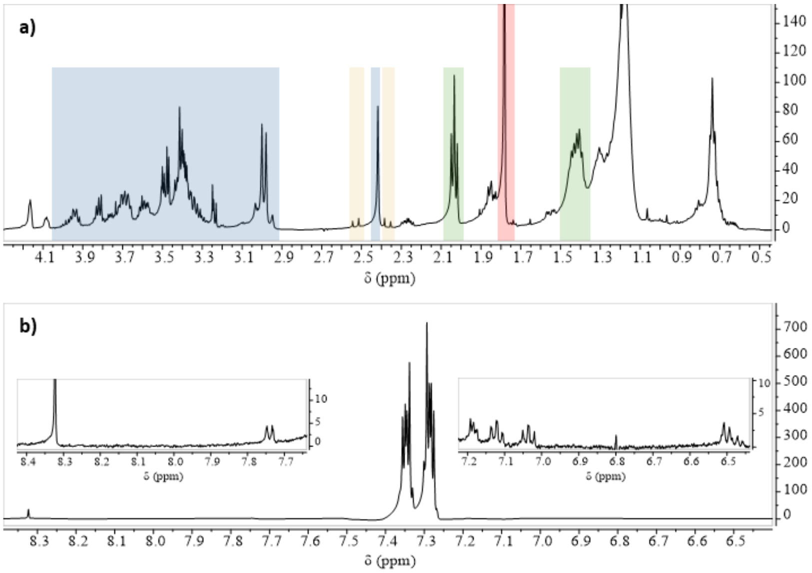

Figure 28. a) The aliphatic and **b)** the aromatic part of the ^{1}H-NMR spectrum of the organic compounds leached out of the 5 g/l complexing agent containing model cemented waste package (500 MHz, 298 K, *ns*=64). The different colors indicate the identified compounds.

First, we searched for the two NMR-detectable complexing agents and their possible metal complexes, and were able to identify and exclude several of them as follows:

- ***EDTA:***

It is well known that pH > 7, EDTA acts as a Lewis base having 6 potential binding sites: two tertiary amino groups, donating two pairs of electrons to a metal ion, and four carboxylates.[210, 211] With these sites, EDTA can form cage-like complexes with metals in 1:1 mole ratio.

Free EDTA typically shows two singlet peaks: acetate-methylene protons ($-N-CH_2-COO^-$, δ= 3.67 ppm) and methylene protons in the backbone($-N-CH_2-CH_2-N-$, δ= 3.28 ppm), however the complex formation of EDTA with metal ions as well as the pH may shift or split these singlet peaks.[211-213] Hafer et al. studied the effect of divalent metal cations (e.g.: Mg, Ca, Sr, Ba) as well as the effect of pH on the chemical shift and coupling of EDTA by ^{1}H NMR spectroscopy and found that increasing pH shifts the proton signal of EDTA to lower ppm values.[212] They also found that upon complex formation the signal of the acetate-methylene protons shifted to δ= 3.08- 3.55 ppm and in some cases their signal split to AB patterns due to the restricted rotation of the acetate-methylene groups, while the backbone- methylene protons remained singlet peaks (δ= 2.48- 3.14 ppm).[212]

These changes are also visible in **Figure 28a** as well, where the singlet peaks of the acetate-methylene protons of EDTA split to an AB quartet ($-N-CH_AH_B-COO^-$, $\delta\sim$ 2.9-3.1 ppm, marked with blue in **Figure 28a**) due to the long-lived metal- N bond, and both these and the backbone- methylene signal ($\delta\sim$ 2.4 ppm) shifted to lower ppm with the alkaline pH of the cementitious environment.[212] As calcium is a main component of Portland cement, it is evident that these peaks belong to the Ca-EDTA complex, being present in the leachate. In the cemented model waste packages, numerous cations are present from both the cement, the metakaolin and the model waste (e.g.: Na^+, K^+, Cs^+, Mg^{2+}, Ca^{2+}, Ni^{2+}, Fe^{3+}, Al^{3+}, Nd^{3+}), thus multifarious EDTA complexes can form. According to literature, K and Fe do not form chelate with EDTA, while Mg-EDTA could be found at 3.2 ppm and 2.7 ppm.[211, 214] The high pH of our leachate could shift these peaks; however, our system contains only a small percentage of Mg (mainly from metakaolin), thus the presence of pure Mg-EDTA complex might be unsignificant as well.

Aluminum is also readily form complexes with EDTA; $Al(EDTA)^-$ at lower pH, $Al(EDTA)(OH)_2^-$ above pH= 7 (pK= 5.8), while above pH= 10 $Al(OH)_4^-$ appears.[215] In the presence of Na^+ and K^+ ions, being both added to the cement in the model solution, the formation of NaAl(EDTA) and KAl(EDTA) multinuclear complexes is possible. These complexes show similar AB quartets and a singlet in the ^{1}H NMR spectra, the width and chemical shift of which strongly depend on the pH and the temperature.[215] According to Jószai et al., these proton signals are in the chemical shift range of ~3-4 ppm, being in good agreement with the ^1H NMR spectrum of the leachate, crowded with peaks in this ppm region (see in **Figure 28**).[215] They observed broad signals for the KAl(EDTA) complex above neutral pH, which can be an explanation for the increased baseline in the proton spectrum below the split signals.[215]

Both Nd and Ni can form stabile complexes with EDTA. In the case of nickel, all the four oxygens and both nitrogen atoms of the EDTA participate in the complex formation.[216] It should be present in the leachate in our case, similarly to Co-EDTA found migrating from the intermediate-level liquid waste disposal pits in USA.[210, 217] Co^{60} migration is widely studied in the presence of EDTA, and an accelerated leaching is described by the soluble Co–EDTA complex.[42, 218] For Nd, it forms stable complexes just like all the trivalent rare earth metals. Furthermore, in the presence of high citrate concentration a mixed complex might form as well (it was found for HEDTA, where one carboxyl is replaced by hydroxyl).[219, 220] Both Nd and Ni are paramagnetic atoms and able to shift the ^1H NMR signals to extreme ppm values: Nd shifts the signals to negative ppm range, while for Ni-complexes, ^1H signals might occur from -30 to 70 ppm.[221, 222] The Nd-EDTA-complex might behave as a paramagnetic shift reagent; thus, other complexes might appear at different chemical shifts compared to the literature.[221] However, none of these extremities can be observed in our spectrum which was also recorded with a ca. 70 ppm spectral window.

Overall, these metal-EDTA complexes may be present in leachate of the 5 g/l complexing agent containing sample and may appear as the peaks between δ= 3-4 ppm in the ^1H NMR spectrum, which moves together based on the DOSY spectrum (see in **Figure A8)**.

- ***Citrate:***

Similarly to EDTA, citrate also may form complexes with the cations present in the model waste package sample. The non-exchangeable protons of the methylene groups of citric acid usually can be found around δ =2 -3 ppm as AB doublet.[223] In the cementitious environment it seems to be evident that Ca-citrate is present in the leachate. Gácsi et al. studied the Ca-citrate system under hyperalkaline conditions, and described a complex with $CaCitH^{2-}$ composition, where the alcoholate and two neighboring carboxylate groups are involved in the complex formation.[223] In the presence of Na, also $NaCit^{2-}$ and Na_2Cit^- ion pairs are present competing with the calcium complexation.[223] This Ca-citrate complex can be observed in the ^1H spectrum of the leachate as an AB doublet between δ =2.4 -2.6 ppm (see in **Figure 28a**, marked with yellow).

It is also known that Fe and Al, both present in the cement, form multinuclear complexes with citrate, resulting in a more complex pattern in the ^1H NMR spectrum. Bodor et al. presented a complex study for the interpretation of the NMR signals of Al-citrate complexes at different pH values.[224] Above pH≈ 8 and at low citrate concentration, the complex with $Al_3(H_{-1}Cit)_3(OH)_4^{7-}$ composition is exclusively present.[224] The high symmetry of this complex results in only two chemical environments for CH_2 protons, resulting in two AB doublets in the NMR spectrum.[224] At pH< 9 the $Al_3(H_{-1}Cit)_3OH(H_2O)^{4-}$ complex appears with a rather complicated pattern between 2.5 and 2.9 ppm with overlapping signals.[224] Basically, we do not have any signals in this chemical shift region of the ^1H spectrum of the leachate, but we can keep this in mind, as the paramagnetic ions present in the solution and the higher pH can cause the shift of the peaks.

The COSY spectrum of the leachate reveals several cross-peaks due to the scalar coupling between the protons bound to adjacent carbons (see in the *Appendix*, **Figure A6**). In the case of citrate, the geminal protons of the CH_2 groups appear as two doublets, as it was shown for the Ca-citrate complex. However, no similar groups of peaks can be observed in the spectrum, in contrast to the numerous COSY cross-peaks. This can be owned to further geminal protons, which are not equivalent due to the complexes formed by the EDTA or the citric acid, but the spectrum reveals spin systems of even five different protons in a quite wide chemical shift range as well, which needs further explanation.

For this reason, the dehydration and decarboxylation reactions of citric acid should be recalled. The dehydration of citric acid is often studied at high temperatures ($T\sim$ 140-160°C) in the presence of a catalyst.[225] At lower temperatures, the same process might take place over a longer time range. In the reaction, aconitic acid is formed in the first step, while aconitic anhydride by further dehydration.[225, 226] For the dehydration the -OH group must be protonated, thus several studies describe this process in acidic medium, however, the protonation constant (p*K*a) of the -OH in citric acid is above 14, meaning that in the basic medium of the cement paste this condition should also be fulfilled.[227, 228] Interestingly, this reaction can also take place in the presence of a heterogeneous catalyst like zeolite or aluminum ions, thus one can draw the conclusion that the components of the cement having similar aluminol groups might also catalyze the dehydration.[225, 229] Decarboxylation is also possible in the cementitious environment, due to the formation of $CaCO_3$ phases, enhanced by the EDTA. [42] The products of these reactions can be a wide range of carboxylic acids, which might also participate in chelating the metals ions present, making the ^1H spectrum more complex and the assignation more difficult.[225, 229] More probable is the presence of glutaric acid, with a triplet at δ =2.03 ppm, and a multiple at δ =1.42 ppm (see in **Figure 28**, marked with green), showing the expected COSY and ^{13}C -^{1}H HSQC and HMBC cross-peaks (see in the *Appendix*, **Figure A5-7).** These signals also show similar diffusivity in the DOSY spectrum (see in **Figure A8)**. An option can be the formation of crotonic acid (δ~ 7 ppm, 6.5ppm and 1.2 ppm) and propane-1,2,3-tricarboxylic acid (δ ~2.3 ppm), which can even form complex mixed complexes, but we cannot identify them on the ^{1}H spectrum. The multistep dehydration of citric acid may involve ring closure reactions resulting in the formation of aconitic anhydrides, the decarboxylation of which may redound the formation of itaconic anhydride or citraconic anhydride.[226] The presence of these compounds in the leachate may explain the signals appearing at aromatic part of the ^{1}H-NMR spectrum (δ> 6.5 ppm, see in **Figure 28b**) without any coupled peak in the aliphatic region.

Compared to the 5 g/l sample, the ^{1}H NMR spectrum of the more concentrated 20 g/l sample is similar, but the intensity of the identified components differs (see in **Figure 29**).

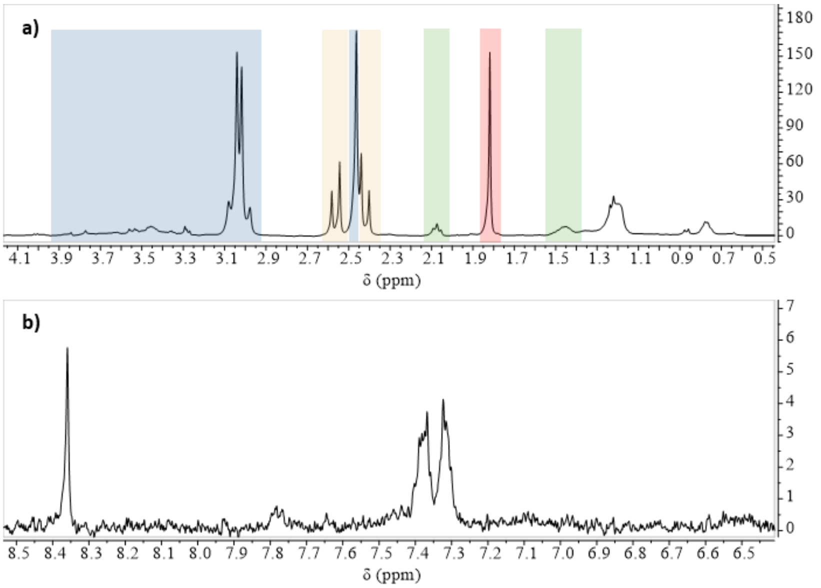

Figure 29. a) The aliphatic and **b)** the aromatic part of the ^{1}H-NMR spectrum of the organic compounds leached from the 20 g/l complexing agent containing model cemented waste package (500 MHz, 298 K, *ns*=64). The different colors indicate the identified compounds.

In this case, the peaks of the Ca-EDTA (δ= 2.4 ppm and around 3 ppm, marked with blue) and Ca-citrate (δ =2.4 -2.6 ppm, marked with yellow) are more enhanced compared to the acetate signal (marked with red), which was added to both samples in equal amounts. This is not surprising, since complexing agents present in large quantities can form the most complexes with calcium, the dominant cation in cement, thus suppressing the signal of other complexes. Thus, in such an elaborate, multicomponent system, various and multinuclear metal complexes as well as new compounds containing double bonds and rings may form. To the best of our knowledge this phenomenon hasn't been observed yet, however, detailed identification needs further investigations.

From the viewpoint of long-term safe disposal of complexing agents containing radioactive waste, it is essential to know how organic compounds behave in the alkaline cementitious environment and in which form they may leach out to the biosphere. It was shown in this section that the complexing agents leach out mainly in the form of metal complexes as well as transform by chemical reactions. The increased complexing agent concentration caused the greater leaching of calcium complexes, in addition to other metal complexes, which may also result in the retardation of cement hydration.

Effect of complexing agents on the diffusivity of water

The diffusion of water in the cemented model waste packages was followed with H_2O–D_2O exchange diffusion technique in case of the 5 g/l and the 20 g/l complexing agent concentrations, the same way as described in *Section 5.1.2*. The obtained proton signal intensity decays are shown in **Figure 30**, where the decays measured in pure cement and the 20% metakaolin composite are also represented for comparison.

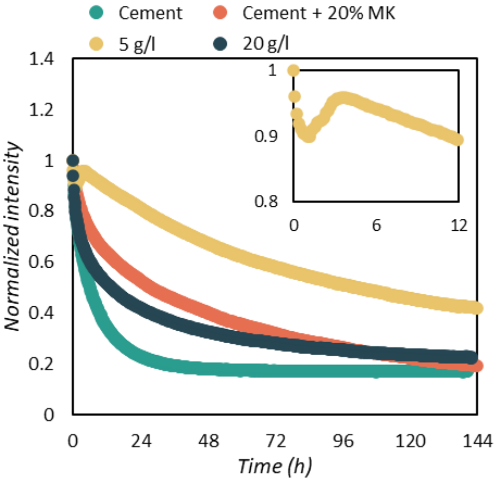

Figure 30. The normalized intensity of the proton signal over time in cemented model waste packages with 5 g/l (yellow) and 20 g/l (dark blue) complexing agent content. For comparison, the curves of pure cement (green) and the 20% metakaolin containing composite (orange) are also presented. The inserted figure is a magnification of the initial section of the curve obtained for the 5 g/l complexing agent content sample.

Three differences can be observed between the curves:

I. *The decay process itself*: the concentration of complexing agents affected the rate of the proton signal decay. In the case of 20 g/l concentration, the decay curve is similar to that of the 20% metakaolin containing composite (the base solid matrix), while in the case of 5 g/l concentration, the decay is prolonged, indicating the restriction of water diffusion.

II. *The residual signal intensity*: this can be assigned to the bound, non- or slowly diffusing water in the solid. After 144 hours, the residual signal intensity is ~20% of the initial value for the 20 g/l probe, similarly to the metakaolin composite, while it only decreased to around 40% in the 5 g/l probe. This also refers to a less permeable pore structure of a more hindered water movement in the 5 g/l model waste package.

III. *The initial part of the decay curves*: a reproducible anomaly was found in the decay curve of the 5 g/l probe over the first hours of the measurement (see in **Figure 30**, inset). The reproducibility of this refers to a real phenomenon, which may be associated with the dissolution and diffusion of some proton containing components (e.g. complexing agents/ complexes) that contribute to the measured proton signal. After the initial fast water diffusion from the surface of the probes, the dissolution of some components increases the signal intensity and reduces the diffusivity prolonging the intensity decay.

The obtained signal decays were fitted with the mathematical model derived by J. Crank.[115] The presence of complexing agents also made the fitting process slightly more difficult by increasing the detectable proton content of the system. For this reason, it became necessary to modify the value of the α and the related parameter (p_n) indicating the volume ratio of D_2O to H_2O. Thus, it should be noted that we did not measure only the diffusion of water. The decay curves were best fitted with the assumption of three diffusion processes, and all the determined diffusion coefficients indicated a strong restriction, meaning that $D < D_{bulk} = 2.3 \times 10^{-9}$ m^2/s.[114] As expected, in the 5 g/l probe the water diffusion was slower ($D_1 = 1.2 \times 10^{-13}$, $D_2 = 2.6 \times 10^{-13}$ m^2/s and $D_3 = 4.8 \times 10^{-12}$ m^2/s), than in the 20 g/l sample ($D_1 = 5.2 \times 10^{-12}$, $D_2 = 6.6 \times 10^{-12}$ m^2/s and $D_3 = 3.6 \times 10^{-11}$ m^2/s) similar to that of the 20% metakaolin containing base matrix. The slower diffusion processes ($D_{1,2}$) may be assigned to restricted movement of water in smaller pores (e.g. in the CSH gel) and the presence of slowly moving components (e.g. metal-complexes seen in the ^{1}H- NMR spectra). While the faster diffusion process may take place in the large capillary pores of the cement matrix. The one-order-of-magnitude difference of D in the two samples indicates a more restricted water diffusion in case of 5 g/l concentration probably caused by the lower permeability of the cement matrix.

Porous structure of the cemented modal waste packages

So far, the effects of the complexing agents on the retention capacity of cement have been analyzed, and from here we change the perspective to the porous structure. The effect of the model radioactive waste (model ions and complexing agents) on the porous structure of solid cementitious matrix was studied in dry state through SEM images, while it was characterized in aqueous states by 1D and 2D NMR relaxometry.

One of the most direct techniques to examine the macroporous structure of cementitious materials is SEM, which not only shows pores but also precipitated hydration products (see in **Figure 31**).

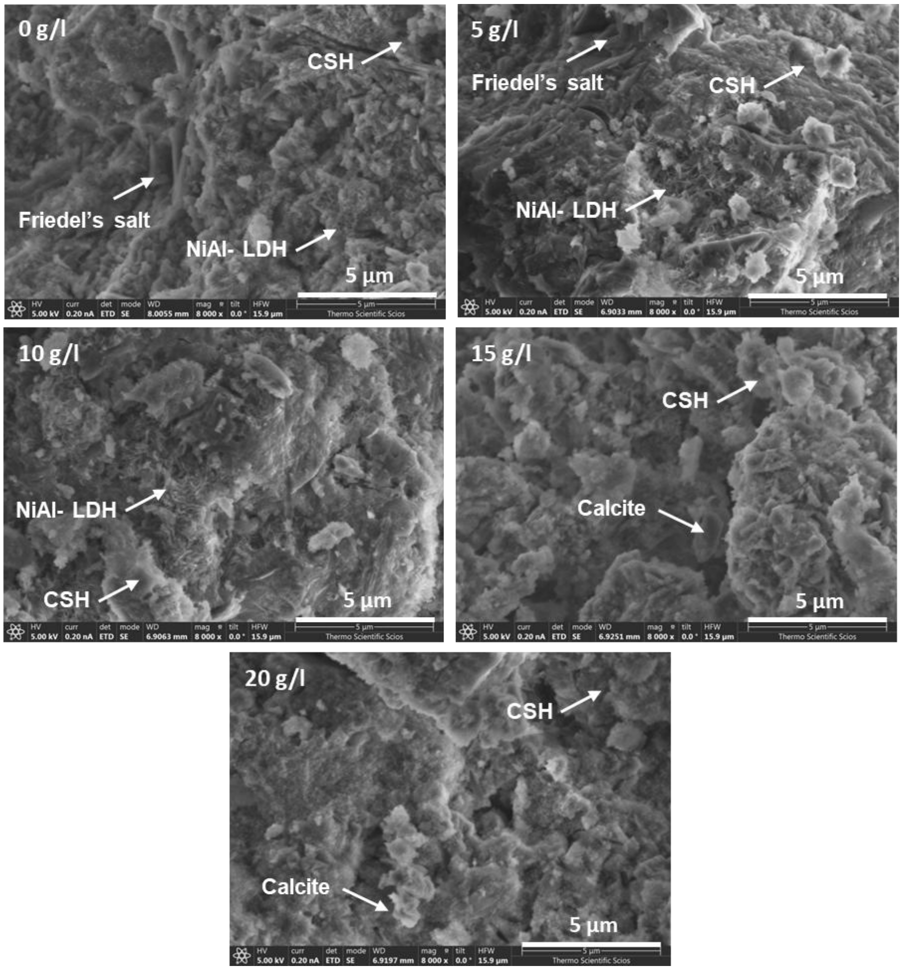

Figure 31. Scanning electron microscopy images of 0-20 g/l complexing agent containing cement specimens showing the precipitated hydration products (CSH- calcium silicate hydrate, NiAl-LDH- nickel-aluminum layered double hydroxides, Calcite and Friedel’s salt).

While in pure cement specimens, the presence of calcium- silicate hydrate (CSH), portlandite and ettringite (Aft) is clearly identifiable, in the model waste packages only the first one appears with great certainty. In the presence of the model radioactive waste compounds, the soluble salts alter the microstructure of cement, through influencing the ionic strength of the pore solution during cement hydration and by ion substitution in the hydrate phases.[230] Thus, instead of the ordinary cement phases, other similar products may form: foil- like NiAl- layered double hydroxides (NiAl-LDH) similar to hydrotalcite[231-233] or hexagonal-like Friedel's salt ($Ca_4Al_2(OH)_{12}Cl_2$ * 4 H_2O) similar to Afm phase[234-236] (see marked in **Figure 31**). These precipitates may be identified up to 15 g/l complexing agent concentration, until the amount of the model ions is larger than that of the complexing agents. The complexing agents in the model waste enhanced the formation of $Ca(CO)_3$ forms, like cubic-shaped calcite, which may be observed above 10 g/l conentration.[42, 237, 238] No significant difference is observable between the porous structure of the five samples in the micrometer size range.

The porous structure of the cemented model waste packages in aqueous states was studied by NMR relaxometry. The resulting T_2 relaxation time distribution curves of the samples are shown in **Figure 32a**, compared to pure cement and the 20% metakaolin composite as a reference. The assignment of the T_2 relaxation time domains to pore types was according to the previous ones in *Section 5.1*. Comparing the T_2 distributions in **Figure 32a**, it is observable that the presence of the model radioactive waste caused the slight merge of the characteristic relaxation time domains and a minor change in their contributions. The latter is more pronounced in the change of the relative amplitude values of the T_2 peaks (see in **Figure 32b**).

The model ions itself (0 g/l) increased the contribution of the smaller pores (A_{1-2}), which is more visible in the case of complexing agent containing samples, where the ratio of A_1 apparently increased. Since these are heterogenous, complex systems, the increasing contribution of the smaller pores may be explained by numerous phenomena like *I)* the additional precipitation of hydrate phases, seen by SEM, or *II)* the change of the mechanism of cement hydration due to additives (e.g. retarding effect of EDTA[239]). Wang et al. studied the effect of Na_2-EDTA on the pore structure of hardened cement pastes by MIP measurements and found that it did not affect the size of the pores but slightly reduced the volume of them (mainly above 300 nm diameter).[240] A similar trend is noticeable in A_3 in the presence of complexing agents (see in **Figure 32b**).

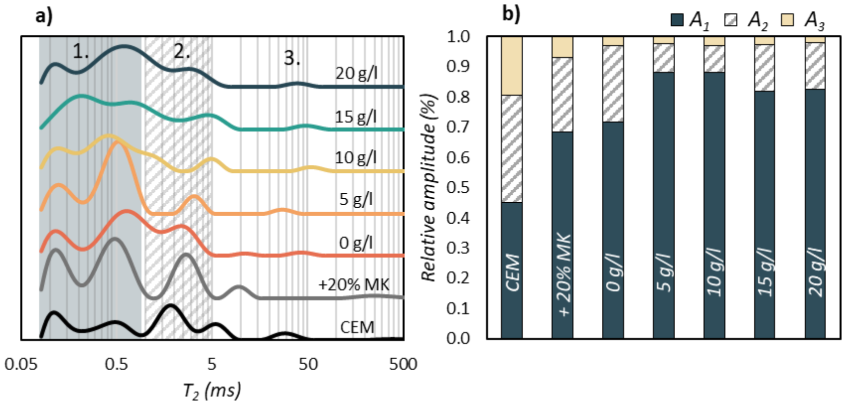

Figure 32. **a)** The T_2 relaxation time distribution in the cemented model waste packages compared to pure Portland cement (CEM, black) and the 20% metakaolin containing composite (+20%MK, grey). The identified pore types are marked on the figure as follows: 1- intra CSH sheet pore, 2- inter CSH gel pore, 3- capillary pore. **b)** Effect of complexing agents on the amplitude of water in different pores (numbers in the subscripts indicate the pore type 1-3).

The permeability of the porous structure of the 5 g/l and 20 g/l complexing agent containing samples was studied by 2D T_1-T_2 correlation NMR relaxometry. The obtained 2D T_1-T_2 correlation maps are shown in **Figure 33**, where in the diagonal, the characteristic pore types (1-3) of cement can be distinguished. As detailed in *Section 5.1.2*, the degree of peak separation provides information about the permeability and openness of the pores.[59, 94] In the case of the 5 g/l specimen, the peaks are more separated compared to the 20 g/l sample, which in accordance with the obtained diffusion processes (see in **Figure 30**), indicates a less permeable pore structure.

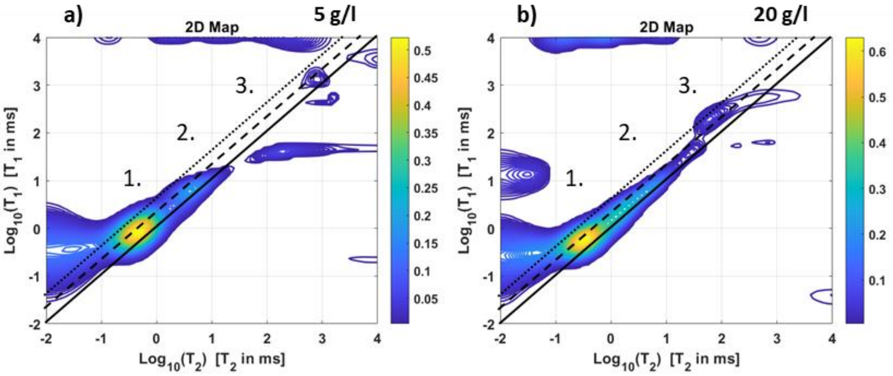

Figure 33. 2D T_1-T_2 relaxation correlation maps of **a)** 5 g/l and **b)** 20 g/l complexing agent containing cemented model waste packages with the characteristic pore types in the diagonal (1- intra CSH sheet pore, 2- inter CSH gel pore, 3- capillary pore). The dashed ($T_1=2T_2$) and dotted ($T_1=4T_2$) lines show the shifted principal diagonal.

The more permeable structure of 20 g/l samples is also apparent from the observable off-diagonal cross peak on the 2D map, since cross-peaks refer to chemical exchange between different water types.[59, 64, 65] The principal diagonal shifted to $T_1=2T_2$, thus the interaction strength between the solid surface and water is similar to that in pure cement and the base solid matrix (+20% metakaolin), see in *Section 5.1.2.*

In summary, it was shown that at low complexing agent concentration (5 g/l), the less permeable porous structure of the solid matrix restricted greatly the diffusion of water in it, however, the leaching of the model ions was enhanced due to the formation of metal- complexes. By contrast, in the case of the 20 g/l sample, the leaching of model ions was more restricted due to the presence of large amounts of free complexing agents and their competition with metal-complexes. Thus, the combined examination of the structural and leaching properties of samples gave a more nuanced picture of the behavior of the model ions in the cemented waste form.

Although radionuclides were simulated in these experiments, it is expected that using active isotopes would yield similar leaching, diffusion, sorption, and complexation behaviors, since radioactive and stable isotopes have nearly identical chemical properties.[14] However, radiation from active isotopes may induce structural and thermal effects in the cement matrix—such as gas formation and heat generation—that could slightly alter cement stability and radionuclide release.[241]

5.2.2. Long-term effect of the waste storage conditions

Monitoring the degradation of cemented waste under real disposal conditions can shed light on the structural changes that occur during the application and the degradation of the hydrate phases, which ultimately affect the sorption capacity and long-term stability of the binders. Ground water may occur in most repository locations after closure, which means the principal degradation of cement in a near-surface waste disposal facility.[28, 242] The hydrate phases of cement are not in equilibrium with the infiltrating water and can dissolve partly upon contact due to the drop of the alkalinity of the pore solution.[28] However, these degradation processes take place over several tens of thousands of years.[26, 28]

In this section, the structural change and degradation of model cemented waste packages under real storage conditions over 10 months are summarized. Model waste packages with 5 g/l and 20 g/l complexing agent concentrations were set in the western ditch of the NRWR at three different locations (dry, stagnant water, flowing water area). Their structural change and degradation were followed for 10 months by NMR relaxometry as it is a sufficiently sensitive method (see in *Section 5.1.1*). We also plan to conduct longer-term studies with the remaining samples in the repository (with an annual sampling cycle). The resulting T_2 relaxation time distributions of the two samples at various locations are shown in **Figure 34**. The characteristic pore types of cement could be identified and are marked on the distributions. The effects of the different locations are the following:

- *Dry location*: In the case of samples stored under dry conditions, the drying-induced water loss of the CSH gel was observed similarly to cement detailed in *Section 5.1.1*. The main changes can be observed in the first three peaks assigned to the intra CSH sheet and inter CSH gel pores (marked with 1 and 2. in **Figure 34a, d**). The amplitude of the 1st peak clearly decreases over time in the case of the 20 g/l sample, while it is quite stable for the 5 g/l sample. The 2nd and 3rd peaks, in addition to the decrease, also slightly shifted to longer T_2 relaxation times for both samples. As cement dries out, the occurring surface effects (e.g. capillary pressure, osmotic pressure) cause the shrinkage of the CSH structure and the drying-induced formation of coarser pores within the gel.[143, 144, 149] The mobile water content of the capillary pores (see in **Figure 34a, d**) did not significantly contribute to the T_2 distributions of the waste packages but slightly decreased over time. The remaining proton signal of these peaks may be assigned to water entrapped in closed pores. The water loss of the cementitious samples is more pronounced in the amplitude change of the water domains. The water content (A) of both the 5g/l and the 20 g/l samples decreased to ~40% of that of the control sample in 2 months. Then, in the following two months the water content increased by 20% (to ~60% of the control sample), indicating the water uptake of the CSH gel. We assume that this may be caused by the varying humidity of the air in the repository. After 4 months, the water content of the samples decreased gradually over time.
- *Stagnant water location*: In the case of samples stored under stagnant water in a pit, the peaks assigned to the CSH gel (marked with 1. and 2. in **Figure 34b, e**) do not vary significantly over time. However, it is visible that the water content of the porous structure increased in the aqueous environment, as the area of the peaks and their amplitude shows. The increase in the A_1 and A_2 (see in the insets of **Figure 34b, e**), may refer to the swelling of the CSH gel (opposite to drying in the previous point).[144, 153]

The increase in the A_3 assigned to the capillary pores, as well as the broadening of these peaks compared to the control sample may imply the dissolution of complexing agent and model ion containing precipitates resulting in more permeable, less separated pores. This process is more pronounced in the case of the 20 g/l sample. The peaks assigned to the capillary pores shift to shorter relaxation times in Round 4 and 5, indicating the somewhat compaction of the structure.

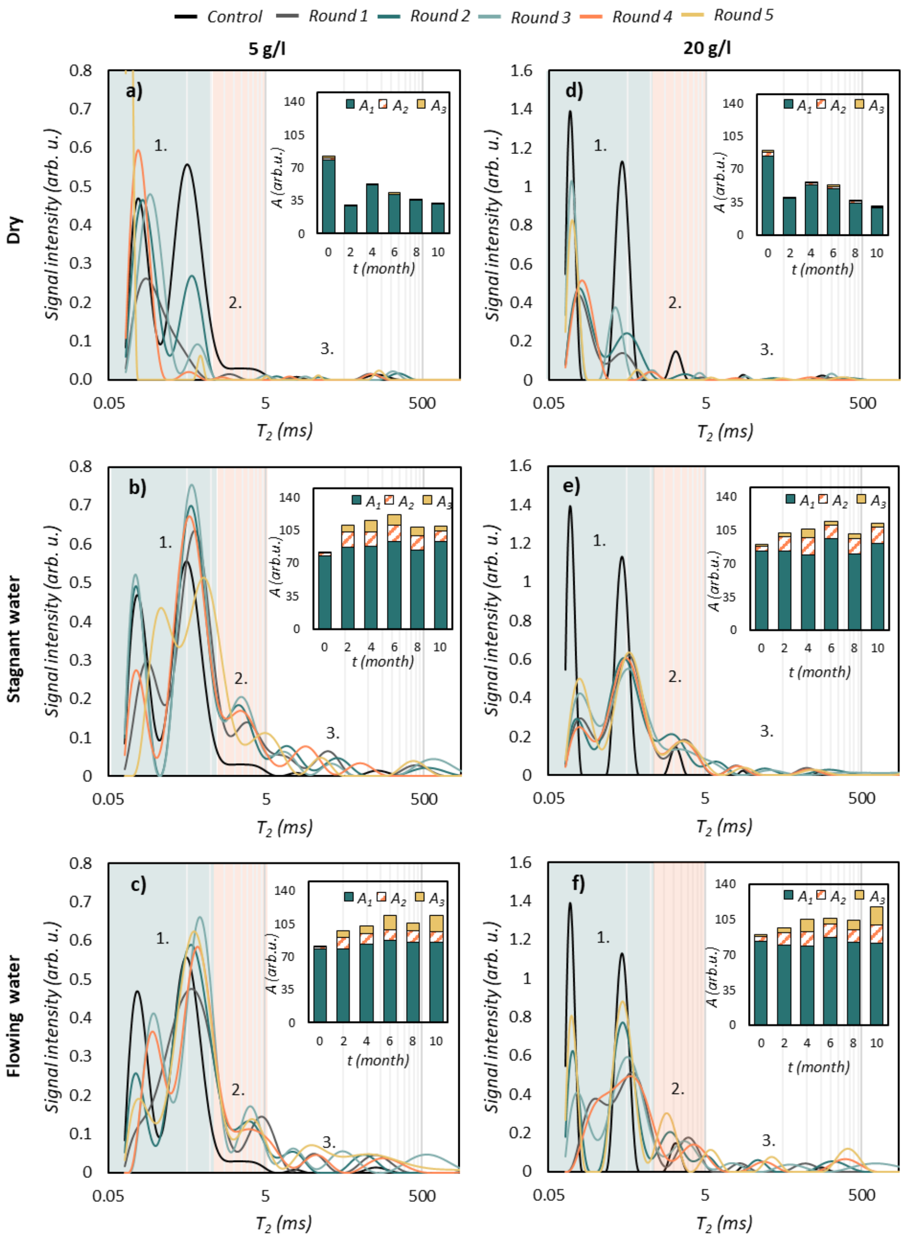

Figure 34. The effect of real conditions on the T_2 relaxation time distributions of the cemented model waste packages with 5 g/l (left) and 20 g/l complexing agent contents (right). The three distinct placement points were: **a, d)** dry, **b, e)** stagnant water and **c, f)** flowing water. The identified pore types are marked on the figure as follows: 1- intra CSH sheet pore, 2- inter CSH gel pore, 3- capillary pore. The inserted graphs show the change of the amplitudes assigned to the water types over time.

- *Flowing water location*: In the case of samples placed in flowing water, the swelling of the CSH gel is also observable (A_1 and A_2 in **Figure 34c, f**), however here the contribution of the larger pores (A_3) is more notable and increases over time. It can be also seen on the T_2 relaxation time distributions, where the position of the peaks assigned to the capillary pores fluctuated significantly. This can also refer to the dissolution of complexing agent containing precipitates, similar to stagnant water. However, here the volume of this process is larger, due to the higher concentration gradient caused by the constantly refreshed, flowing water, which facilitates the dissolution of the precipitates and the increasing macroporous character of the samples. The precipitates seen on the outer surface of the sample also support these assumptions. Based on these results so far, flowing water has had the most significant influence on the porous structure of the binders.

The aqueous environments had a slightly greater impact on the 20 g/l samples compared to the 5 g/l, as expected from the results presented in *Section 5.2.1*: the less restricted water diffusion and the more permeable porous structure in case of the 20 g/l specimen.

5.3. Examination of the repository's multi-barrier system

The final step of nuclear waste management is the disposal of radioactive waste in a licensed repository facility without intention of retrieval.[12] The repository should ensure long-term safe disposal of radioactive waste and isolate the waste from the biosphere.[12, 16] Usually, the multi-barrier concept is used for containment, which consists of engineered and natural restricting barriers.[12, 16, 18] These barriers ensure that radionuclides decay below exemption levels before their possibly release.[12] The engineered barrier system (EBS) contains *I)* the solidified waste package, *II)* the metallic container, *III)* backfill materials (e.g. clays, concrete), while the host rock of the repository is the natural geological barrier (NGB).[16]

Here, after the comprehensive characterization of the binding materials and the model waste packages, our perspective shifts towards the examination of other parts of the multi- barrier system, namely to bentonite as a backfill material and the Boda Claystone Formation as a possible natural geological barrier.

5.3.1. Bentonite- Engineered barrier

The engineered barriers of a repository should ensure complete containment of short-lived radionuclides.[16] While the solidified waste form and the metallic container limit the potential leaching of radionuclides to the groundwater, backfill materials should delay the possible emission of radionuclides to the environment as well as limit water flux toward the waste package.[16, 243] Backfill materials are used to fill the void spaces in the repository to limit water intrusion and to prevent the release of radionuclides through their sorption properties.[16] Swelling clay, such as bentonite, can ensure both processes. Bentonite is a high montmorillonite containing smectite clay mineral, known for its high swelling capacity and sorption properties. Montmorillonite is a layered aluminosilicate mineral consisting of silica-, aluminum- and oxygen-based, negatively charged, octahedral and tetrahedral layers (TOT structure).[244-247] The negative charge of the TOT layers is compensated by the counter ions (e.g. Na^+, Ca^{2+}) located in the interlayer spaces. [244-247] Bentonite, due to its layered structure, can bind water through swelling and restrict the diffusion of water, while the constant negative charge between the layers allows the sorption of cations. However, the degree of interaction with water is significantly influenced by the structure of bentonite, including the arrangement of the tetrahedral and octahedral planes and the quality of the cations incorporated between them. The structure of bentonite can be interpreted with three different structural units on different size-scales (see in **Figure 35**).[243]

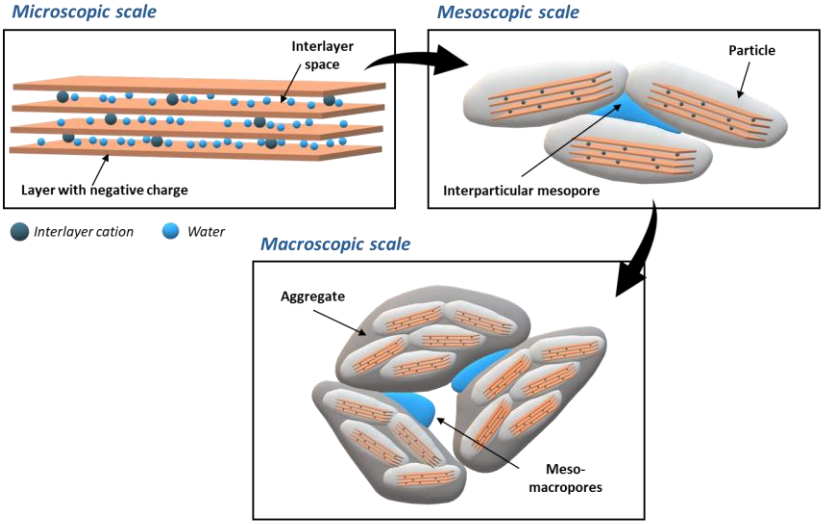

Figure 35. The schematic multi-scale structure of bentonite, based on the work of Salles et al.[243]

On the microscopic scale we can talk about the negatively charged TOT layers and their exchangeable counter ions, on the mesoscopic scale these layers associates to ordered lamella stacks (particles), while on the macroscopic scale the aggregates of these particles can be discussed according to Salles et al.[243]

The aqueous behavior, the structure and swelling properties of montmorillonite is extensively studied for example by thermogravimetric analysis[248], thermoporometry[243], particles size distribution method[249], NMR spectroscopy[245, 248, 250-252] as well as modeled by computational techniques.[244, 246, 247, 253] In this section, the investigation of the structure and swelling kinetics of two bentonite samples (Ca- and Na-bentonite) is presented at different water contents and over time by NMR relaxometry. The diffusion of water in the water saturated samples at equilibrium state was studied by PGSE NMR.

The obtained T_2 transversal relaxation times of water confined in the two bentonite samples at different water contents are shown in **Figure 36**. Two-three different water domains may be distinguished in the bentonite samples, which is expected based on the presence of various sized pores in bentonite and the complex electrochemical interactions (e.g. hydrogen bonding, osmotic attraction by the electric double layer charged surface- dipole attraction, London dispersion forces) between the bentonite particles and water.[250] The water domain with the shortest relaxation time (T_{2a}~ 0.2-

0.9 ms, marked with dark blue diamond in **Figure 36a**) may be assigned to the interlamellar water in the interlamellar spaces. Water in the smaller interparticular mesopores (T_{2b}~ 1.2- 8.7 ms, marked with orange triangle) and in the mesopores between the aggregates (T_{2c}~ 10- 72 ms, marked with blue circle) has somewhat greater mobility and is more sensitive to the increment of the water content. This last domain dominates (A_c, see in **Figure 36b**) in the Na-bentonite sample, while it is not present in Ca-bentonite.

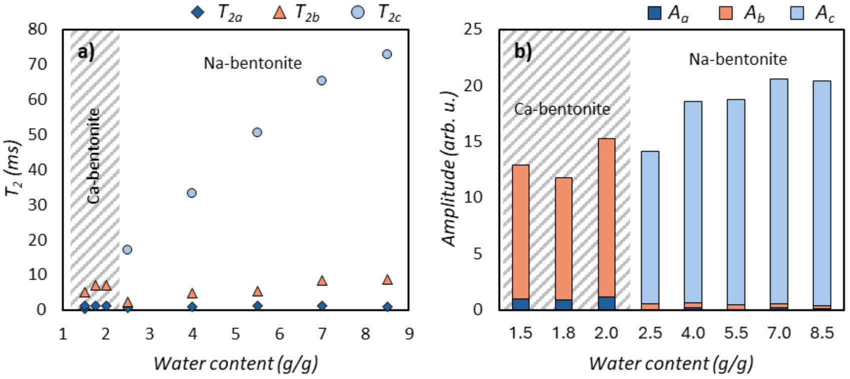

Figure 36. The effect of the added water content on **a)** the T_2 relaxation times and **b)** amplitude of water confined in Ca- and Na-bentonite. Water domains in different confinements are color coded: interlamellar space (T_{2a}, dark blue, diamond), interparticular mesopores (T_{2b}, orange, triangle) and larger mesopores between the aggregates (T_{2c}, light blue, circle).

With increasing water content, the characteristic relaxation times showed a minimal increase in the case of Ca-bentonite, while in the case of Na-bentonite, a significant increase was observed, indicating the greater swelling capacity of the latter. A similar increasing trend was found by NMR in several studies.[245, 248, 250] In the case of samples with the highest water content (2.2 g/g for Ca-bentonite and 8.5 g/g for Na-bentonite), the swelling process was followed in-situ by repetitive measurements (see **Figure 37a, b**) for 2-4 days. Most changes occurred in the T_2 relaxation time of water located in the larger mesopores between the bentonite particle aggregates, the amount of which is dominant in Na-bentonite (~70% of the water content), contrary to Ca-bentonite, where it is less than 1% of the water seen by NMR and disappears in the fully swollen sample (see inf **Figure 36a**). This difference between the bentonites is well visible on the T_2 distribution curves shown in **Figure 37c, d**.

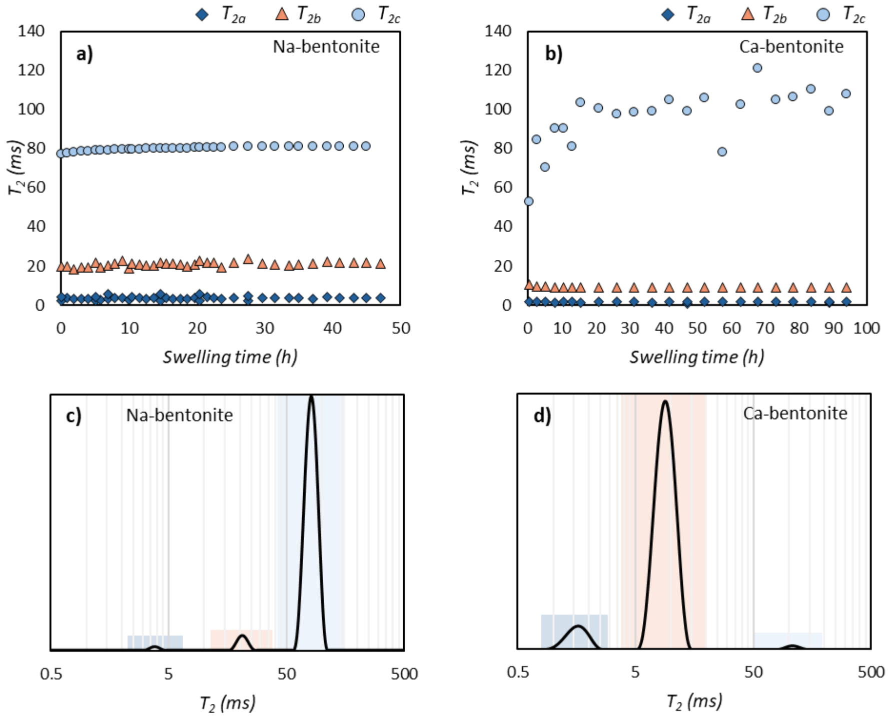

Figure 37. The change of the T_2 relaxation times over the swelling of **a)** Na- and **b)** Ca-bentonite with the indication of the different water types: interlamellar space (T_{2a}, dark blue, diamond), interparticular mesopores (T_{2b}, orange, triangle) and larger mesopores between the aggregates (T_{2c}, light blue, circle). The T_2 distribution curves of **c)** Na- and **d)** Ca-bentonite at the end point of the swelling measurement, where the contribution of the water types is highlighted.

Comparing the changes of the T_2 relaxation times over time in the case of the bentonite samples (see **Figure 37a, b**) it can be clearly seen that the value of T_{2a} and T_{2b} (water in the interlamellar space and interparticular mesopores) is lower in the Ca-bentonite samples, while T_{2c} (water between the aggregates) is longer compared to the Na-containing one. It indicates the more bound state of water in the smaller pores, and the less hindered movement of water in the larger mesopores in the Ca-analogue. In contrast, the mobility of water in the larger mesopores of Na-bentonite is restricted by the swelling solid phase.

Upon hydration, three main swelling processes characterize the structural changes of smectites, such as bentonite: a) crystalline swelling, b) osmotic swelling, and c) Brownian swelling.[243, 254, 255] Crystalline swelling occurs between TOT layers as water molecules shield the attractive interactions between the counterion and the clay layers involving the formation of 1- 4 layers of water molecules in the interlamellar spaces.[243, 254, 255] Osmotic swelling is an entropy driven process caused by the different counterion concentrations in the interlamellar space and the mesopores.[243, 254, 255] As the counter ions diffuse and absorb on the external surface of the lamellas, a Stern- and diffusive layer may form on their surface causing the weakening of the attractive van der Waals force between the lamellas according to the DLVO theory, which may result in the separation of the layers.[243, 254] Brownian swelling is also an entropy driven process occurring in highly diluted systems and means the thermal motion/ spread of the separated bentonite layers.[254, 255] While the swelling of Na- bentonite can be both crystalline and osmotic, Ca-bentonite mainly can go through crystalline swelling.[245]

The swelling kinetics of bentonites were studied by fitting the swelling curves derived from the T_2 transversal relaxation times with several kinetic models applied for swelling polymers in the literature.[256-260] We elaborated this novel kinetic modeling procedure based on T_2 relaxation data on swelling biodegradable crosslinked polymers, and the method seemed to be applicable for swelling bentonites as well, according to the following.[256]

The swelling kinetics of swelling materials (e.g. polymers) are usually deduced from the solvent uptake of the solid network in time. The ratio between the weight of the swollen solid at t time (m_t) and that of the dry solid (m_0) results in the swelling degree ($SD\%$), which changes in time like a saturation curve as the solvent enters the porous structure and reaches an equilibrium state. Here, the change of the T_{2c} was matched to the $SD\%$ considering the surface relaxivity (ξ) of bentonite and the bulk liquid relaxation time (T_{2bulk}) constant in **Equation 7,** since the quality of the bentonite is the same during the swelling:

$$SD(\%) = \frac{m_t - m_0}{m_0} \times 100 \sim \frac{T_{2(t)} - T_{2(0)}}{T_{2(0)}} \times 100 \qquad (21)$$

where $T_2(t)$ is the relaxation time constant of the swelling liquid at t time, $T_{2(0)}$ is the relaxation time constant in the initial state of the liquid.[256] The derived $SD\%(T_2)$ - swelling time curves are shown in **Figure 38a**.

Numerous kinetic models exist for the description of the swelling mechanism of hydrogels, which are well summarized in the study of Adnadjevic and Jovanovic.[260] These models were tested on the two bentonite samples, among which the second-order kinetics model described best the swelling process of the bentonites (see in **Figure 38b**). This model was proposed by H. Schott to describe the swelling of semicrystalline cross-linked polymers, where many kinds of polymer - solution interactions (e.g., H- bonds, dispersion effects, looping of mesh chains) may be present, which is not considered in the first-order kinetics model.[256, 258, 259]

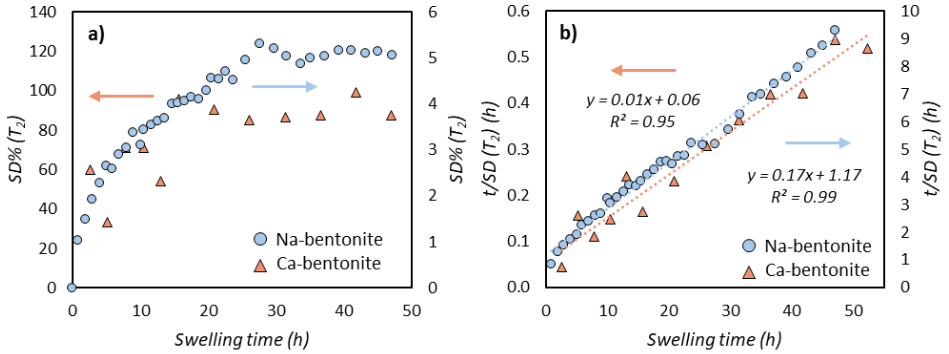

Figure 38. a) Swelling isotherms (SD% as a function of time for Na- and Ca-bentonite samples in water at 298 K derived from the T_{2c} relaxation time values. **b)** $t/SD(T_2)$ as a function of swelling time for bentonite samples with their fittings.

The second-order kinetics model gave better fits also for diffusion-controlled swelling compared to the other one.[249, 258] The second-order kinetics assumes a linear relationship between the *t/SD*% and time for the entire swelling period:[258]

$$\frac{t}{SD} = \frac{1}{SD_{eq}} t + \frac{1}{k_s \times {SD_{eq}}^2} \tag{22}$$

where SD_{eq} is the swelling degree at the equilibrium, k_s is the second-order swelling rate constant. This model presumes that the swelling rate depends on the available swelling capacity of the material at time *t* and on the so-called internal specific boundary area enclosing the sites, which have not interacted with the solvent at time *t* yet but are supposed to do it later.[258, 259] This finding can be attributed to the surface, where secondary interactions exist between the clay particles/ layers that will break due to swelling and permitting the expansion of the layered structure.

The second-order swelling rate constants of the saturated bentonites were derived from the linear fittings of $t/SD(T_2)$ curves are k_s= 0.02 1/h for Na- bentonite and k_s= 0.002 1/h for Ca- bentonite. These rate constants may be assigned to the osmotic swelling of bentonite, which is not notable in Ca-bentonite, as the small amplitudes of this domain (A_c, marked with light blue in **Figure 37d**), and the slow swelling rate constant shows. Magzoub et al. also applied the second-order kinetics model for the swelling of Ca/Na bentonites measured by particle size distribution method and obtained rate constants in the range of 0.002- 0.124 1/h.[249]

The structural change of the water saturated bentonites during osmotic swelling in our interpretation is the following: after immersing the bentonites, especially Na-bentonite into water, the solvation and crystalline swelling of the TOT layers happen. After that the hydrated counter ions and water may diffuse and absorb on the external surface of the lamellas creating an electric double layer, which decreases the secondary interactions between the lamellas/ particles and allows the expansion of the solid structure through osmotic swelling. This process is described in more detail in the *Appendix*.

In swollen bentonites lamellas, particles and aggregates can restrict the free movement of water molecules; thus, studying their self-diffusion may provide additional information about the solid structure and its permeability.[106-108, 256, 261] The diffusion of water was measured only within the swollen Na-bentonite by high-field NMR diffusometry (DOSY), since the fast relaxation of the most dominant water domain doesn't allow the diffusion measurement in Ca-bentonite (**Figure 37d**). According to T_2 relaxation times of water in Na- bentonite (**Figure 37c**), the diffusion of water between the aggregates in larger mesopores may be detected during the measurement. The obtained ^{1}H DOSY NMR spectra is shown in **Figure 39a**. The measurements were performed using several diffusion times (Δ). **Figure 39b** shows the diffusion time dependence of the determined diffusion coefficients (D= 7.5 × 10^{-10} - 1.7 × 10^{-9} m^2/s), the value of which is in all cases lower than that of bulk water (D_{bulk}= 2.3 × 10^{-9} m^2/s) indicating the somewhat restricted diffusion of water.[114] At longer diffusion times, where more time is available for the molecules to diffuse, the exponential decay of the ^{1}H proton signal could be fitted with two exponentials (**Equation 9**) as well, resulting in two diffusion coefficients ($D_{2\text{-}3}$ in **Figure 39b**). The faster diffusion (D_2~ 1.7 × 10^{-9} m^2/s) was similar to the ones gained from the single exponential fitting (D_1~ 1.5 × 10^{-9} m^2/s), while the more hindered diffusion process (D_3~ 7.5 × 10^{-10}), became detectable only at longer diffusion times, was almost an order of magnitude slower than D_1. Similar values were found in literature, while Dvinskikh and Fúró also found two diffusion processes in Na-bentonite.[251, 252, 262] The $D-\Delta$ curves are usually S-shaped and can be divided into three parts: free, restricted, and hindered diffusion regions.[106, 107] However, in our sample no diffusion time dependence of the diffusion coefficients could be clearly observed, thus this may mean that due to the permeability of the pore structure, the interpore diffusion is averaged, thus hindered diffusion region is reached.[106, 107]

In this region, the permeability (K) and the tortuosity (T) of the porous system can be determined. The permeability of a solid means its ability to transport fluid, while tortuosity indicates the diffusion path taken by the fluid in the porous structure, which greatly depends on the heterogeneity of the solid.[263, 264] According to Carman- Kozeny law, these two parameters are in correlation.[263, 264] Tortuosity (T) can be calculated from the ratio of the self-diffusion coefficient (D_∞) measured at long diffusion time (Δ) and that of the bulk liquid (D_0), as $D_0/D_\infty= T$. Thus, the tortuosity of Na-bentonite happened to be T= 1.5 (calculated from D_1). According to Nakashima, this is the predominant factor affecting the diffusivity of water in bentonite in NMR measurements.[251]

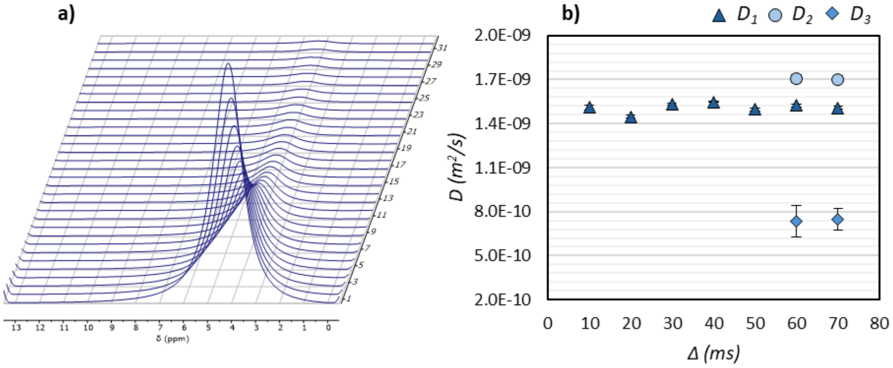

Figure 39. a) ^{1}H DOSY NMR spectra of water confined in swollen Na-bentonite. **b)** Diffusion time dependence of the diffusion coefficients derived (500 MHz, 298 K, *ns*= 64).

In summary, in this section the aqueous behavior of two bentonite samples was investigated with NMR which gave insight into the porous structure, the swelling mechanism of the bentonites as well as the characterization of the water diffusivity within the heterogenous swollen structure of them.

5.3.2. Boda Claystone Formation- Natural geological barrier

Geological formations are essential isolation barriers in geological repositories, the main purpose of which, beside the isolation of the waste form the biosphere, is the limitation of the possible release of long- lived radionuclides over several thousands (ILW) or several hundreds of thousands of years (HLW, SFW) from the progressively degrading engineered barriers.[16] Deep geological disposal is one of the main concepts of geological disposal, meaning the location of waste at ≥ 3 km depth, limiting any possible transport of radionuclides to the environment.[16] For this kind of repository, a suitable host rock is necessary, which should have favorable chemical, physical, geometrical, mechanical properties and be a uniform rock formation in a relatively simple geological environment.[265] Different types of rocks may meet these conditions, like crystalline, sedimentary (i.e., clay) or evaporite (i.e., salt) rocks.[16] In Hungary, the Boda Claystone Formation (BCF) is a possible host rock for the installation of a deep geological waste repository.

In this section, two borehole samples of Boda Claystone Formation (BCF) from different depth were investigated by low- field NMR to characterize the porous structure and the petrophysical characteristics of the host rock, which essentially influences the possible transportation process of radionuclides by the ground water.

In water-saturated rocks usually three different water types can be distinguished: the non-evaporable clay-bound water, the capillary-bound water, and the movable water (see in **Figure 40**).[112] From the point of view of the host- rock properties, some of the most important parameters are the permeability and the $T_{2cut\text{-}off}$ value of the rock. The latter one enables the distinguishment of the free- fluid index (FFI) and the bulk volume irreducible (BVI, see in **Figure 40**).[112] A further $T_{2cut\text{-}off}$ value for the clay-bound water may also be determined; however, in this case, the overlap of the T_2 relaxation time constants of the clay- and capillary-bound water may make it difficult.[112]

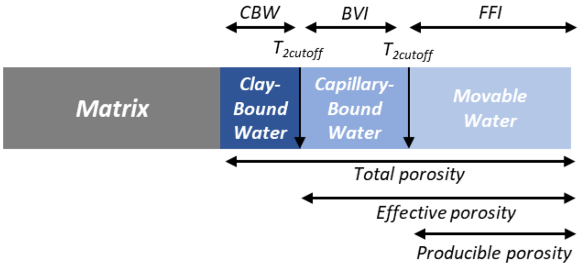

Figure 40. The composition of a rock with the porosities, determined by the water domains. The two typical $T_{2cut\text{-}off}$ values distinguish the movable and non-movable water domains as well as the non-evaporable clay- bound water and the capillary- bound water.[112]

The total NMR porosity (φ) of the rock sample, which is a lithology independent porosity value[266], can be calculated from the intensity of the measured T_2 decay curves and the derived T_2 distribution curves can be directly calibrated to porosity (see the y axis in **Figure 41**).[112] The determined porosities of the borehole samples were the following: φ=1.5% for BCF1 and φ= 5.8% for BCF2. Fedor et al. performed He-pycnometry and MIP measurements on other BCF samples and found that the porosity of the samples varied between 0.78 – 3%.[23] The porosity values obtained from NMR are comparable with these.

The T_2 relaxation time distribution of dry and water saturated borehole samples are shown in **Figure 41**, where four types of water with different mobility can be distinguished and assigned to pores of different sizes observed previously by Fedor et al.[23] The size of the pores was estimated according to **Equation 7**, assuming slit-like pores and a surface relativity value ($\xi \sim 2.7$ nm/ms) calculated from the ratio of $T_{2s} \sim 0.11$ ms (main relaxation domain after drying) and $\lambda \sim 0.3$ nm.[72, 80, 82, 83] The obtained pore size distributions are shown in the *Appendix*, **Figure A9**. The first fast relaxing (T_2~ 0.1 ms, d ~ 0.6 nm, ultramicropores) water domain in **Figure 41** can be identified as water bound to the clay mineral phase of the claystone. Water domains between T_2~ 0.7- 7.3 ms may be assigned to water filling the capillary pores (mesopores, 2 nm $< d <$ 50 nm). Meanwhile, the last domain, visible around T_2~ 50 ms, can be identified as water in the larger macropores of the claystone (d ~ 200- 500 nm).

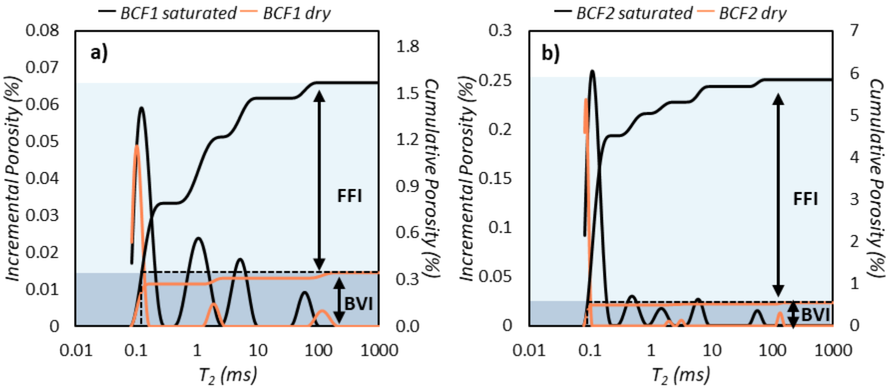

Figure 41. T_2 relaxation time distribution and the derived cumulative pore volume distributions of **a)** BCF1 and **b)** BCF2 in water saturated (black curves) and dry (orange curves) states. The vertical dashed lines shows the $T_{2cut\text{-}off}$ values, which separates the movable (*FFI*) pore filling water from the non-movable (*BVI*) bound water in the rock.

The quantitative contributions of the different pores can be deduced from the comparison of the areas of the T_2 domains in the water-saturated state. In the case of the BCF1 sample, the contribution of the ultramicropores (clay-bound water) was 51%, while that of the mesopores (capillary-bound water) was 43%, and it was 6% for macropores (movable water). Contrary, in BCF2 the ratios were as follows: 77% ultramicropores (clay-bound water), 20% mesopores (capillary-bound water), 3% macropores (movable water), meaning this borehole sample contained more clay mineral phases. By drying the samples, the intensity of the most bound type of water slightly changes, while a significant decrease can be observed in the movable water content (see in **Figure 41**, orange curves), the characteristic T_2 values of which slightly increase.

The $T_{2cut\text{-}off}$ values were determined from the intersection of the cumulative porosities of the borehole samples in dry and water saturated states (marked with dashed lines in **Figure 41**) according to the usual method applied by geologists.[112] $T_{2cut\text{-}off}$ was slightly higher for BCF1 (0.12 ms) than for BCF2 (0.10 ms). Usually, conventional reservoir rocks may be characterized with an exact $T_{2cut\text{-}off}$ value, like in sandstones $T_{2cut\text{-}off}$ is 33 ms, while it is 90-100 ms for carbonates and 3 ms is commonly used to identify clay bound water.[267] There are cases when the commonly accepted $T_{2cut\text{-}off}$ values are not suitable for the examined rocks, since many factors may influence it (e.g. capillary pressure, lithology, pore characteristics, paramagnetic impurities).[112] Sedimentary rocks (e.g. shales and claystones) are good examples of unconventional reservoirs, the complex pore network and small sized pores of which make their characterization challenging. [267] Testamanti and Rezaee found that in saturated shale samples most of the T_2 relaxation times occurred below 3 ms, thus the conventionally accepted clay bound water cut-off was unsuitable and instead they received $T_{2cut\text{-}off} \sim 0.22$ and 0.26 ms.[267] They also highlighted that in case of shale during drying temperature above 65°C caused the temporary loss of interlayer water in clays and affected permanently the porous structure.[267] This structural change and water loss in the clay phase can result in a lower apparent porosity, which can affect the determination of the $T_{2cut\text{-}off}$ value. Thus, the low $T_{2cut\text{-}off}$ values found in our claystone samples may be the result of structural changes caused by thermal damage, affecting the porosity, or maybe the determined $T_{2cut\text{-}off}$ values are suitable for separating CBW/ (FFI+BVI) instead of FFI/ BVI. We do not yet have enough information to decide this.

Assuming that the determined $T_{2cut\text{-}off}$ values can be used to distinguish FFI and BVI, the porosity of the rocks was divided (marked in **Figure 41**) between them. The FFI/BVI ratio was 1.21% / 0.35% = 3.5 for BCF1 and 5.28% / 0.56% = 9.43 for BCF2.

The lithology-independent permeability of a rock, which corresponds to the ability of a rock to transmit fluids, can be estimated from its T_2 relaxation time distribution.[266, 268-272] The two empirical models for the estimation of permeability (K) are the Kenyon model (also known as Schlumberger-Doll Research or SDR model)[273] and the Timur–Coates model.[112, 274] The Kenyon model calculates the permeability based on the logarithmic mean value of T_2 distribution ($T_{2,LM}$) as a pseudo-average pore size, while the Timur–Coates model uses the FFI/ BVI ratios determined based on the $T_{2cut\text{-}off}$ values.[112, 266, 268-274] Both two models were used for the permeability estimation of the borehole samples:

$$K_{SDR} = C_1 \varphi^m T_{2,LM}^n \qquad (23)$$

$$K_{coates} = \left(\frac{\varphi}{C_2}\right)^m \left(\frac{FFI}{BVI}\right)^n \qquad (24)$$

where φ is the porosity in percentage, C_1 and C_2 are empirical constants depending on the lithology of the rock, m and n are statistical model parameters.[273] [275] In the case of unknown rock, the values of $C_{1,2}$, m and n are typically set to 10, 4, 2 respectively.[272, 275]

The estimated permeability values were $K_{SDR} = 6.3 \times 10^{-14}$ m^2 and $K_{coates} = 5.9 \times 10^{-18}$ m^2 for BCF1; and $K_{SDR} = 3.8 \times 10^{-11}$ m^2 and $K_{coates} = 9.9 \times 10^{-15}$ m^2 for BCF2, indicating a less permeable structure for BFC1. Fedor et al. found somewhat lower values around 10^{-17} - 10^{-21} m^2 for other BCF samples by the pressure pulse decay (PPD) method.[21, 23] Bernáth et al. also studied the porosity and permeability of BCF borehole samples by NMR logging measurements and found that the porosity, bulk water content, and permeability are mainly related to cracks and cracked zones of the rock.[276] Their determined permeability values varied between 10^{-7}- 10 mD (millidarcy, 1D = 9.87×10^{-13} m^2) similar to our K_{coates} values.[276] The possible drawback of the above-mentioned models may be that they estimate the K values based on one variable and do not exploit the rich information content of the T_2 relaxation time distributions.[266]

The diffusion of water in the BCF2 borehole sample was followed by H_2O- D_2O exchange diffusion technique similarly to the cementitious materials described in *Section 5.1.2 and Section 5.2.1.* A relatively fast proton signal decay was found over time as shown in **Figure 42**.

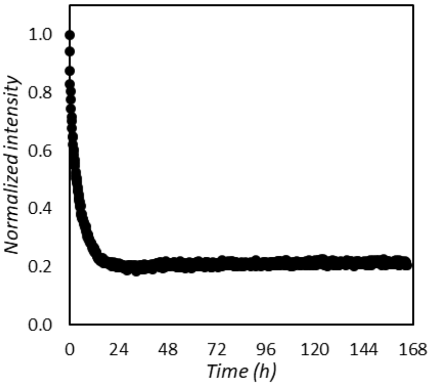

Figure 42. The normalized intensity of the proton signal over time in BCF2 borehole sample.

The diffusion coefficients of water were determined with a mathematical model derived by J. Crank[115] and the decay curve was best fitted with the assumption of two diffusion processes. The determined diffusion coefficients were $D_1 = 9.6 \times 10^{-12}$ m^2/s and $D_2 = 1.9 \times 10^{-10}$m^2/s. These restricted water diffusion processes may take place in the larger meso- and macropores of the claystone. These results confirm the compactness and very low permeability of BCF, which makes it suitable for the disposal of high-level waste.

6. Comprehensive characterization of a waste repository facility from the point of view of water diffusion

Water is the main medium for the transportation of radionuclides released from solidified waste forms, thus knowing its mobility in the waste repository is crucial for the long-term safe disposal of radioactive waste.[241, 277]

The self-diffusion coefficients (*D*) of water were determined at different levels of the radioactive waste repository. The determined *D* values are summarized in **Figure 43**, where a quasi- enhanced, but still restricted water diffusion can be observed from the inside, moving from the cemented waste form towards the host rock. In all cases, 2-3 diffusion processes could be distinguished. This proves that each single level of the multi-barrier system can retrain the diffusion of water, thus the migration of radionuclides.

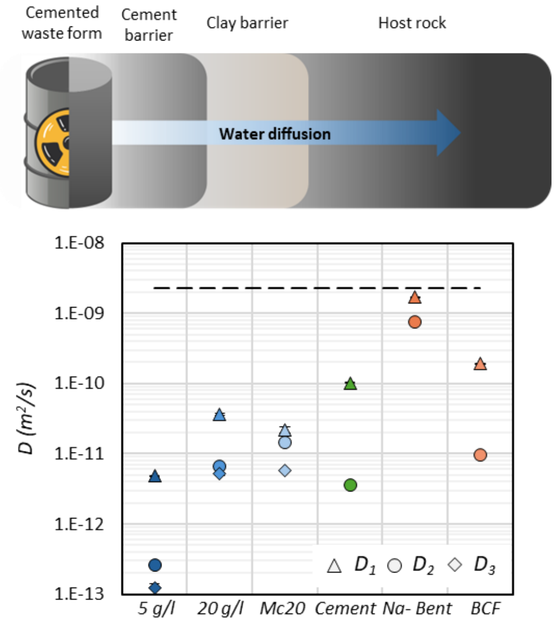

Figure 43. The alteration of the self-diffusion coefficient of water from the cemented model waste packages, through the engineered barriers (cement, bentonite), towards the geological barrier (host rock). The dashed line shows the self-diffusion coefficient of bulk water (D_{bulk}= 2.3 × 10^{-9} m^2/s[114]).

7. Summary

The aim of my doctoral research was to investigate the properties of waste forms, engineered barriers, and the geological environment for the final disposal of radioactive waste. Through the comparison of the NMR relaxometry with other structural characterization techniques it was shown that NMR relaxometry is a well applicable technique for the comprehensive characterization of the micro- and mesostructure of the main hydrate phase of cement, the CSH gel. It was also confirmed that NMR relaxometry is a sufficiently sensitive method to test the drying induced changes of cement. In conclusion, NMR relaxometry is a favorable method for industrial applications as well, since it can be reproducibly used to investigate the structure of wet and dry samples, or to monitor the formation/change of the structure in situ.

The effect of two pozzolans (metakaolin and fly ash) on the structure formation, hardened pore structure and surface properties of Portland cement was investigated. It was found that metakaolin mainly increased the rate of the CSH precipitation in the deceleration period (10-24 h), while fly ash affected the entire hydration process. FFC NMR measurements combined with the *3-Tau* model shed light on the stronger water-solid interactions in the fly ash composite. The comprehensive structural investigation of the composites showed that the metakaolin composites possessed a more contiguous solid matrix with few macroscopic voids, where the porous structure is dominated by the presence of micro- and mesopores. In the fly ash composites, the remaining fly ash particles enhanced the heterogeneity of the structure and increased the macro- and microporous features of the solid. These structural changes also affected the diffusion of water within the solid, causing a more restricted diffusion process in the metakaolin composite and a significant amount of remaining water in the micropores for the fly ash composites. Regarding the aimed application of the cement matrix, the substitution of cement with 20% metakaolin resulted in the most promising binder for the long-term safe disposal of radioactive waste.

With the permission of PURAM, model cemented waste packages were prepared based on the actual cementing recipe of radioactive waste. The probes contained model ions and complexing agents in various concentrations, typical of real waste. The model waste packages and the effect of the concentration of complexing agents were studied in two main directions (pore structure and leachability). The following trend was found relating to the leachability of the model ions: cesium> rhenium> nickel. The leachability of the three ions with respect to the complexing agent content was as follows: 0 and 20 g/l < 10 g/l < 5 and 15 g/l, meaning that at certain concentrations the leaching process is facilitated. Regarding the complexing agent content of the leachates, it was found that at 5 g/l concentration, the complexing agents leached out in the form of various and multinuclear metal complexes as well as transformed into compounds containing double bonds and rings, enhancing the mobilization of the model ions. At 20 g/l concentration, the greater leaching of calcium complexes, in addition to other metal complexes, was observed. Under the influence of complexing agents and model ions, a few new cement hydrate phases were formed (e.g.: NiAl-LDH, calcite), which increased the contribution of the smaller pores and slightly reduced the volume of larger pores. The effective diffusion coefficient of the model ions quasi decreased with increasing concentrations. In the case of the 5 g/l sample, a one-order-of-magnitude slower, anomalous water diffusion process was observed, compared to the 20 g/l sample, caused by the lower permeability of the cement matrix. Furthermore, moving beyond basic research towards application, the behavior of model waste packages under real disposal conditions was studied in the NRWR. Changes in the pore structure of the specimens indicated a significant effect of flowing water, while in the case of dry samples the drying of the CSH gel was observed.

Two levels of the multiple barrier system responsible for the long-term safety of radioactive waste repositories were also investigated: the engineering barrier (Na-, Ca-bentonite) and the geological environment suitable for the disposal of high-level waste (BCF). The structural changes of bentonite samples with increasing water content indicated the greater swelling ability of Na-bentonite. The swelling of Na-bentonite was monitored in situ and the modeling of the time dependence of the measured T_2 relaxation times indicated second-order kinetics swelling mechanism. In the swollen Na-bentonite sample, two restricted water diffusion processes were distinguished during HF-NMR measurements. In the case of the BCF borehole samples, the $T_{2\text{-}cutoff}$ value characterizing the porosity and bound water content was determined using NMR relaxometry. Two different water diffusion processes were distinguished in the reservoir rock.

In summary, during my doctoral research, I characterized the different levels of the multiple barrier system of radioactive waste repositories from a materials science perspective, paying special attention to the examination of waste packages. The diversity and complexity of the examined samples necessitated a multidisciplinary approach and the combined application of various examination methods. With the innovative combination of these methods, several key pieces of information (e.g.: porosity, permeability, leachability, water diffusion) were obtained that are useful for the safety analysis of radioactive waste repositories and the development of matrix materials for waste packages.

8. Összefoglalás

Doktori kutatómunkám célja a radioaktív hulladékok elhelyezése során alkalmazott kötőanyagok, mérnöki gátrendszer és a geológiai környezet tulajdonságainak (kioldhatóság, anyagszerkezet, permeábilitás) vizsgálata volt, főként folyadék fázisú NMR spektroszkópiás módszerekkel. Kutatómunkám három fő részre volt osztható, az eredményeket eszerint a felosztás szerint ismertetem.

Radioaktív hulladékok végleges elhelyezéséhez kapcsolódó kötőanyagok

Elsőként a hulladék kondicionálására alkalmas kötőanyag, a Portland cement vizes és száraz közegű pórusszerkezeti jellemzését végeztük el komplex módon, számos szerkezetvizsgáló módszer együttes alkalmazásával, mely szükséges kiindulási alap volt az egyes adalékok hatásának vizsgálatához és képet adott a valós körülmények között lejátszódó folyamatokról (száradás). Az eredmények megerősítették, hogy az NMR relaxometria egy jól alkalmazható technika a fő cement hidrát fázis, a CSH gél mikro- és mezostruktúrájának átfogó jellemzésére, a különböző pórusok T_2 relaxációs idő szerinti elkülönítésére, valamint kellően érzékeny módszer a cement száradás okozta változásainak vizsgálatára. Összefoglalva, az NMR relaxometria egy kedvező módszer ipari alkalmazásra is, mely reprodukálhatóan alkalmazható nedves és száraz minták szerkezetének vizsgálatára, vagy a szerkezet kialakulásának/változásának in situ monitorozására.

Ezt követően a két puccolán adalék (metakaolin, kőszénpernye) hatását vizsgáltuk a Portland cement szerkezetére és felületi tulajdonságaira. A puccolánok hatását a cement hidratációjára NMR relaxometriás és FFC NMR mérésekkel követtük, mely rámutatott arra, hogy bár mindkét puccolán növeli a CSH gél és alumínium tartalmú hidrát fázisok mennyiségét, azt a cement hidratációs folyamatának más- más szakaszában teszik meg. Ennek ismerete a hulladékcsomagok kiöntése során lehet hasznos: míg a metakaolin főként a cement hidratációjának deklarációs szakaszában (10-24 h) gyorsította a fő hidratációs termék kiválását, addig a kőszénpernye a folyamat minden szakaszát lassította. Az FFC NMR mérések a 3-Tau modellel kombinálva rávilágítottak az adalék tartalmú mintákban erősebb víz- szilárdanyag kölcsönhatásra a cementhez képest. A megszilárdult metakaolin tartalmú cementekben a víz diffúziója lassabbnak bizonyult a kőszénpernyéhez képest, és az adaléktartalom függvényében 20 % aránynál mutatott minimumot. A pórusok átjárhatósága szempontjából is 20 % metakaolin esetén találtuk a leginkább elkülönülő pórusokat és a legkisebb mértékű cserefolyamatot a T_1-T_2 korrelációs mérések alapján. A kőszénpernye 20 %-ban a cementhez adagolva szintén javította a megszilárdult kötőanyag mikropórusos szerkezetét és növelte a megkötött víztartalmát. Azonban ezzel párhuzamosan nőtt minta makropórusos jellege is, mely vízdiffúzió szempontjából kedvezőtlen. Ezzel szemben a metakaolin a cement mikro- és mezopórusos jellegét növelte, mely kevésbé permeábilis, homogénebb és összefüggő szilárd mátrixot eredményezett. Így a metakaolin kedvezőbb adalékanyagnak bizonyult a radioaktív hulladékok hosszú távú biztonságos elhelyezése szempontjából.

Valós hulladéktárolás körülményeinek hatása

Az RHK Kft. engedélyével a valósan alkalmazott cementálási receptúra alapján készítettünk modell hulladékcsomag próbatesteket, melyek a cementen és metakaolinon túl a valós hulladékot jellemző modell oldatot, modell ionokat és komplexképzőket tartalmaztak különböző koncentrációban. A modell hulladékcsomagokat két fő irányvonalon (pórusszerkezet és kioldhatósági tulajdonságok) jellemeztük és vizsgáltuk a komplexképzők koncentrációjának hatását. A kioldhatósági tulajdonságok vizsgálatára gyorsított kioldási kísérletet végeztünk, majd meghatároztuk a kioldott fázisok modell ion (Cs, Re, Ni) és szerves szén tartalmát ICP MS és nagyterű NMR technikákkal. A modellionok kioldhatósága tekintetében a következő trendet tapasztaltuk: cézium> rénium> nikkel. A három ion kioldhatósága a komplexképző koncentrációkra nézve a következőképp alakult: 0 és 20 g/l <10 g/l <5 és 15 g/l, ami azt jelenti, hogy bizonyos koncentrációknál a kioldódási folyamat kedvezményezett volt. Az ionok effektív diffúziós együtthatója kvázi csökkent a komplexképzők koncentrációjának növelésével. Az 5 g/l komplexképző tartalmú minta esetén egy elnyújtott, anomáliát mutató víz diffúziós folyamatot találtunk, a 20 g/l komplexképző tartalmú mintához képest, melyben a víz a 20% metakaolin tartalmú kompozithoz hasonlóan mozgott. A kioldódott szerves széntartalom nagyterű NMR spektroszkópiás azonosítása során, az 5 g/l minta esetén egy komplex proton spektrumot kaptunk, mely különböző egy- és többmagvú fémkomplexek, valamint kettős kötéseket és gyűrűket tartalmazó új vegyületek jelenlétre utalt. Ezzel szemben a 20 g/l koncentráció esetén komplexképző ágensek főként Ca-komplexek formájában mosódtak ki. A komplexképzők és modell ionok hatására számos új cement hidrát termék képződött (pl.: NiAl-LDH, kalcit), melyek csökkentették a nagyobb pórusok és növelték a kisebbek hozzájárulását a cement pórusszerkezetéhez. 5 g/l koncentráció esetén a pórusszerkezet permeábilitása alacsonyabb volt, mely jó egyezést mutatott a mért jelentősen gátolt víz diffúzióval.

Ezenfelül, az alapkutatáson túl az alkalmazás irányában elmozdulva vizsgáltuk a modell hulladékcsomagok viselkedését valós körülmények között a Nemzeti Radioaktívhulladék-tárolóban (NRHT) három különböző pontján. A próbatestek pórusszerkezetében bekövetkező változások rámutattak az átfolyó víz szignifikáns szerkezetalakító hatására, míg a száraz állapotú minták esetén a CSH gél száradását tapasztaltuk.

A hulladéktároló többszörös gátrendszerének vizsgálata

A radioaktívhulladék-tárolók hosszú távú biztonságáért felelős többszörös gátrendszer vízmozgás szempontjából fontos két szintjét, a mérnöki gátat (Na-, Ca-bentonit) és a nagyaktivitású hulladékok elhelyezésére alkalmas geológiai környezetet (Bodai Aleurolit Formáció) is vizsgáltuk. A bentonit minták növekvő víztartalom hatására bekövetkező szerkezetváltozása rámutatott a Na-bentonit kedvező duzzadóképességére. A Na-bentonit duzzadását in situ követtük és a mért T_2 relaxációs idők időfüggésének modellezése az agyagásvány másodrendű kinetika szerinti duzzadására utalt. A duzzasztott Na-bentonit mintában két gátolt vízdiffúziós folyamatot tudtunk elkülöníteni nagyterű NMR mérések során.

A Bodai Aleurolit Formáció két különböző mélységből származó furatmintájának pórusszerkezetét, porozitását és a víz kötöttségét jellemző $T_{2\text{-}cutoff}$ értékét NMR relaxometriásan határoztuk meg. A tároló kőzetben H_2O- D_2O cserediffúziós technikával két különböző víz diffúziós folyamatot találtunk.

Összegezve a doktori kutatásom során anyagtudományi oldalról jellemeztem a radioaktív hulladéktárolók többszörös gátrendszerének különböző szintjeit, kiemelt figyelmet fordítva a hulladékcsomagok vizsgálatára. A vizsgált minták sokszínűsége és komplexitása szükségessé tette a multidiszciplináris megközelítést és a különféle vizsgálati módszerek együttes alkalmazását. A vizsgált szilárd minták több ponton elengedhetetlenné tették a folyadék alapú NMR módszerek optimalizálását, új mérési módok bevonását a kutatásba. A módszerek innovatív kombinációjával olyan kulcsfontosságú információkat nyertünk (pl.: porozitás, permeábilitás, kioldhatóság, vízdiffúzió), melyek hasznosak a radioaktív hulladéktárolók biztonsági elemzésének, valamint a hulladékcsomagolások mátrixanyagának fejlesztése szempontjából.

9. References

1. *Disposal of Radioactive Waste*. INTERNATIONAL ATOMIC ENERGY AGENCY: Vienna, 2011.
2. Zagyvai, P., et al., *A nukleáris üzemanyagciklus radioaktív hulladékai : egyetemi jegyzet*. MTA Energiatudományi Kutatóközpont: Budapest, 2013.
3. Barbhuiya, S., et al., Cement-based solidification of nuclear waste: Mechanisms, formulations and regulatory considerations. *Journal of Environmental Management* **2024,** *356*, 120712.
4. Ojovan, M. I., et al., Chapter 1 - Introduction to Immobilisation. In *An Introduction to Nuclear Waste Immobilisation (Third Edition)*, Ojovan, M. I.; Lee, W. E.; Kalmykov, S. N., Eds. Elsevier: 2019; pp 1.
5. Ojovan, M. I., et al., Chapter 9 - Principles of Nuclear Waste Management. In *An Introduction to Nuclear Waste Immobilisation (Third Edition)*, Ojovan, M. I.; Lee, W. E.; Kalmykov, S. N., Eds. Elsevier: 2019; pp 107.
6. *Fundamental Safety Principles*. INTERNATIONAL ATOMIC ENERGY AGENCY: Vienna, 2006.
7. 1996. évi CXVI. törvény az atomenergiáról. Országgyűlés, Ed. 1996.
8. COUNCIL DIRECTIVE 2011/70/EURATOM of 19 July 2011 establishing a Community framework for the responsible and safe management of spent fuel and radioactive waste. Union, C. o. t. E., Ed. 2011.
9. A kiégett üzemanyag és a radioaktív hulladék kezelésének nemzeti politikája. Kormánya, M., Ed. 2015.
10. Magyarország nemzeti programja a kiégétt üzemanyag és a radioaktív hulladék kezelésére. Kormánya, M., Ed. 2016.
11. *Classification of Radioactive Waste*. INTERNATIONAL ATOMIC ENERGY AGENCY: Vienna, 2009.
12. Ojovan, M. I., et al., Chapter 13 - Nuclear Waste Processing Schemes. In *An Introduction to Nuclear Waste Immobilisation (Third Edition)*, Ojovan, M. I.; Lee, W. E.; Kalmykov, S. N., Eds. Elsevier: 2019; pp 167.
13. *Radiological characterization of shut down nuclear reactors for decommissioning purposes*; IAEA, Vienna (Austria); International Atomic Energy Agency, Vienna (Austria): IAEA, 1998; p Medium: X; Size: 184 p.
14. Nagy, N., et al., Környezeti radioaktivitás. *Magyar Kémiai Folyóirat* **2019,** *125*, 75.
15. *Characterization of Radioactive Waste Forms and Packages*. INTERNATIONAL ATOMIC ENERGY AGENCY: Vienna, 1997.
16. Ojovan, M. I., et al., Chapter 22 - Nuclear Waste Disposal. In *An Introduction to Nuclear Waste Immobilisation (Third Edition)*, Ojovan, M. I.; Lee, W. E.; Kalmykov, S. N., Eds. Elsevier: 2019; pp 415.
17. *The Safety Case and Safety Assessment for the Disposal of Radioactive Waste*. INTERNATIONAL ATOMIC ENERGY AGENCY: Vienna, 2012.
18. *Design Principles and Approaches for Radioactive Waste Repositories*. INTERNATIONAL ATOMIC ENERGY AGENCY: Vienna, 2020.
19. Nős, B., Innovációk a radioaktívhulladék- elhelyezésben. RHK, Ed. 2025.
20. Demény, A., et al., A Preliminary Stable Isotope Study on a Potential Radioactive Waste Repository Site in the Mecsek Mountains, Southern Hungary. *Rapid Communications in Mass Spectrometry* **1996,** *10* (11), 1415.
21. Fedor, F., et al., Laboratory pressure pulse decay permeability measurement of Boda Claystone, Mecsek Mts., SW Hungary. *Physics and Chemistry of the Earth, Parts A/B/C* **2008,** *33*, S45.

22. R. Varga, A., et al., Chemical composition, provenance and early diagenetic processes of playa lake deposits from the Boda Siltstone Formation (Upper Permian), SW Hungary. *Acta Geologica Hungarica* **2005,** *48* (1), 49.
23. Fedor, F., et al., New results of Boda Claystone research: Genesis, mineralogy, geochemistry, petrophysics. In *Multiple Roles of Clays in Radioactive Waste Confinement*, Norris, S.; Neeft, E. A. C.; Van Geet, M., Eds. Geological Society of London: 2019; Vol. 482, p 0.
24. Nős, B., A mérnöki gátak szerepe a Bátaapáti Tároló biztonságában *Nukleon* **2009,** *2* (3), 42.
25. Baranyi, A., et al., Radioactive Waste Embedding in Cement Matrix and the Establishment of Cemented Waste Testing Laboratory at Paks Nuclear Power Plant. *Journal of Physics: Conference Series* **2022,** *2315* (1), 012030.
26. Ma, B., et al., The essential role of cement-based materials in a radioactive waste repository. *npj Materials Sustainability* **2024,** *2* (1), 21.
27. Ojovan, M. I., et al., Chapter 17 - Immobilisation of Radioactive Waste in Cement. In *An Introduction to Nuclear Waste Immobilisation (Third Edition)*, Ojovan, M. I.; Lee, W. E.; Kalmykov, S. N., Eds. Elsevier: 2019; pp 271.
28. Ochs, M., et al., Cementitious Materials and Their Sorption Properties. In *Radionuclide and Metal Sorption on Cement and Concrete*, Ochs, M.; Mallants, D.; Wang, L., Eds. Springer International Publishing: Cham, 2016; pp 5.
29. Li, J., et al., Solidification of radioactive wastes by cement-based materials. *Progress in Nuclear Energy* **2021,** *141*, 103957.
30. Marchon, D., et al., 8 - Mechanisms of cement hydration. In *Science and Technology of Concrete Admixtures*, Aïtcin, P.-C.; Flatt, R. J., Eds. Woodhead Publishing: 2016; pp 129.
31. Aïtcin, P. C., 3 - Portland cement. In *Science and Technology of Concrete Admixtures*, Aïtcin, P.-C.; Flatt, R. J., Eds. Woodhead Publishing: 2016; pp 27.
32. Luhar, I., et al., Solidification/Stabilization Technology for Radioactive Wastes Using Cement: An Appraisal. *Materials* **2023,** *16* (3), 954.
33. Koťátková, J., et al., Concrete and cement composites used for radioactive waste deposition. *Journal of Environmental Radioactivity* **2017,** *178-179*, 147.
34. Jennings, H. M., Refinements to colloid model of C-S-H in cement: CM-II. *Cement and Concrete Research* **2008,** *38* (3), 275.
35. Feldman, R. F., et al., A model for hydrated Portland cement paste as deduced from sorption-length change and mechanical properties. *Matériaux et Construction* **1968,** *1* (6), 509.
36. Basquiroto de Souza, F., et al., A century of research on calcium silicate hydrate (C–S–H): Leaping from structural characterization to nanoengineering. *Journal of the American Ceramic Society* **2022,** *105* (5), 3081.
37. Powers, T. C. *Physical properties of cement paste*; 1960.
38. Powers, T. C., et al., Studies of the Physical Properties of Hardened Portland Cement Paste. *ACI Journal Proceedings 43* (9).
39. *The Behaviours of Cementitious Materials in Long Term Storage and Disposal of Radioactive Waste*. INTERNATIONAL ATOMIC ENERGY AGENCY: Vienna, 2013.
40. Fabian, M., et al., Characterization of Simulated Liquid Radioactive Waste in a New Type of Cement Mixture. *ACS Omega* **2022,** *7* (41), 36108.
41. El-Kamash, A. M., et al., Leaching kinetics of 137Cs and 60Co radionuclides fixed in cement and cement-based materials. *Cement and Concrete Research* **2002,** *32* (11), 1797.
42. Goo, J.-Y., et al., Effects of EDTA on the leaching behaviors of Cs(I) and Co(II) from cement waste forms. *Journal of Hazardous Materials* **2024,** *463*, 132830.

43. Goo, J.-Y., et al., Leaching Behavior of Cesium, Strontium, Cobalt, and Europium from Immobilized Cement Matrix. *Applied Sciences* **2021,** *11* (18), 8418.
44. Ojovan, M. I., et al., Long-term field and laboratory leaching tests of cemented radioactive wastes. *Journal of Hazardous Materials* **2011,** *187* (1), 296.
45. Papadokostaki, K. G., et al., Study of leaching mechanisms of caesium ions incorporated in Ordinary Portland Cement. *Journal of Hazardous Materials* **2009,** *171* (1), 1024.
46. Yokozeki, K., Chapter 9 - Leaching from Cementitious Materials Used in Radioactive Waste Disposal Sites. In *Thermodynamics, Solubility and Environmental Issues*, Letcher, T. M., Ed. Elsevier: Amsterdam, 2007; pp 169.
47. Liu, P. S., et al., Chapter Nine - Characterization Methods: Basic Factors. In *Porous Materials*, Liu, P. S.; Chen, G. F., Eds. Butterworth-Heinemann: Boston, 2014; pp 411.
48. Washburn, E. W., Note on a Method of Determining the Distribution of Pore Sizes in a Porous Material. *Proceedings of the National Academy of Sciences* **1921,** *7* (4), 115.
49. Cook, R. A., et al., Mercury porosimetry of cement-based materials and associated correction factors. *Construction and Building Materials* **1993,** *7* (4), 231.
50. Cook, R. A., et al., Mercury porosimetry of hardened cement pastes. *Cement and Concrete Research* **1999,** *29* (6), 933.
51. Rouquerol, J., et al., Liquid intrusion and alternative methods for the characterization of macroporous materials (IUPAC Technical Report). *Pure and Applied Chemistry* **2011,** *84* (1), 107.
52. Meyer, K., et al., NIST recommended practice guide ::porosity and specific surface area measurements for solid materials. , National Institute of Standards and Technology, Gaithersburg, MD: 2006.
53. László, K., *Felületek fizikai kémiája*. Typotex Kiadó: 2011.
54. Thommes, M., et al., Physisorption of gases, with special reference to the evaluation of surface area and pore size distribution (IUPAC Technical Report). *Pure and Applied Chemistry* **2015,** *87* (9-10), 1051.
55. Sing, K., The use of nitrogen adsorption for the characterisation of porous materials. *Colloids and Surfaces A: Physicochemical and Engineering Aspects* **2001,** *187-188*, 3.
56. Akhtar, K., et al., Scanning Electron Microscopy: Principle and Applications in Nanomaterials Characterization. In *Handbook of Materials Characterization*, Sharma, S. K., Ed. Springer International Publishing: Cham, 2018; pp 113.
57. Zhou, W., et al., Fundamentals of Scanning Electron Microscopy (SEM). In *Scanning Microscopy for Nanotechnology: Techniques and Applications*, Zhou, W.; Wang, Z. L., Eds. Springer New York: New York, NY, 2007; pp 1.
58. Bede, A., et al., NMR relaxation of molecules confined inside the cement paste pores under partially saturated conditions. *Cement and Concrete Research* **2016,** *89*, 56.
59. McDonald, P. J., et al., Surface relaxation and chemical exchange in hydrating cement pastes: A two-dimensional NMR relaxation study. *Physical Review E* **2005,** *72* (1), 011409.
60. Papp, V., et al., State and role of water confined in cement and composites modified with metakaolin and additives. *Journal of Molecular Liquids* **2023,** *388*, 122716.
61. Ardelean, I., The Effect of an Accelerator on Cement Paste Capillary Pores: NMR Relaxometry Investigations. *Molecules* **2021,** *26* (17), 5328.
62. Rusu, M. M., et al., Monitoring the Effect of Calcium Nitrate on the Induction Period of Cement Hydration via Low-Field NMR Relaxometry. *Molecules* **2023,** *28* (2), 476.
63. Cadar, C., et al., NMR T1–T2 correlation analysis of molecular absorption inside a hardened cement paste containing silanised silica fume. *Molecular Physics* **2019,** *117* (7-8), 1000.

64. McDonald, P. J., et al., Two-dimensional correlation relaxometry studies of cement pastes performed using a new one-sided NMR magnet. *Cement and Concrete Research* **2007,** *37* (3), 303.
65. McDonald, P. J., et al., Two-dimensional correlation relaxation studies of cement pastes. *Magnetic Resonance Imaging* **2007,** *25* (4), 470.
66. Fleury, M., et al., Diffusion of water in industrial cement and concrete. *Magn Reson Imaging* **2019,** *56*, 32.
67. Fleury, M., et al., Water diffusion measurements in cement paste, mortar and concrete using a fast NMR based technique. *Construction and Building Materials* **2020,** *259*, 119843.
68. Hore, P. J., *Mágneses magrezonancia*. Nemzeti Tankönyvkiadó Rt.: Debrecen-Budapest, 2004.
69. Blümich, B., Introduction. In *Essential NMR: For Scientists and Engineers*, Blümich, B., Ed. Springer International Publishing: Cham, 2019; pp 1.
70. Blümich, B., Basic Principles. In *Essential NMR: For Scientists and Engineers*, Blümich, B., Ed. Springer International Publishing: Cham, 2019; pp 9.
71. McDonald, P. J., et al. *The characterisation of cement based materials using T2 1H nuclear magnetic resonance relaxation analysis*; NPL Management Ltd: UK, 2016.
72. Barrie, P., Characterization of porous media using NMR methods. 2000; Vol. 41, pp 265.
73. Mirau, P. A., *A Practical Guide to Understanding the NMR of Polymers*. John Wiley & Sons, Inc.: 2005.
74. Valori, A., et al., The morphology of C–S–H: Lessons from 1H nuclear magnetic resonance relaxometry. *Cement and Concrete Research* **2013,** *49*, 65.
75. Nestle, N., et al., Liquid-phase self-diffusion in hydrating cement pastes — results from NMR studies and perspectives for further research. *Cement and Concrete Research* **2007,** *37* (3), 398.
76. Jurt, S., et al., *Applied NMR Spectroscopy for Chemists and Life Scientists*. Wiley-VCH Verlag GmbH: 2013.
77. Kéri, M., et al., Interaction of resorcinol-formaldehyde carbon aerogels with water: A comprehensive NMR study. *Carbon* **2022,** *189*, 57.
78. Brownstein, K. R., et al., Spin-lattice relaxation in a system governed by diffusion. *Journal of Magnetic Resonance (1969)* **1977,** *26* (1), 17.
79. Halperin, W. P., et al., Application of spin-spin relaxation to measurement of surface area and pore size distributions in a hydrating cement paste. *Magnetic Resonance Imaging* **1994,** *12* (2), 169.
80. D'Orazio, F., et al., Molecular diffusion and nuclear-magnetic-resonance relaxation of water in unsaturated porous silica glass. *Physical Review B* **1990,** *42* (16), 9810.
81. Blümich, B., Relaxometry and Laplace NMR. In *Essential NMR: For Scientists and Engineers*, Blümich, B., Ed. Springer International Publishing: Cham, 2019; pp 111.
82. D'Orazio, F., et al., Application of nuclear magnetic resonance pore structure analysis to porous silica glass. *Journal of Applied Physics* **1989,** *65* (2), 742.
83. Allen, S. G., et al., Morphology of porous media studied by nuclear magnetic resonance. *The Journal of Chemical Physics* **1997,** *106* (18), 7802.
84. Liu, H., et al., Determining pore length scales and pore surface relaxivity of rock cores by internal magnetic fields modulation at 2MHz NMR. *Journal of Magnetic Resonance* **2014,** *246*, 110.
85. Muller, A. C. A., et al., A reassessment of mercury intrusion porosimetry by comparison with 1H NMR relaxometry. *Cement and Concrete Research* **2017,** *100*, 350.

86. Muller, A. C. A., et al., Use of bench-top NMR to measure the density, composition and desorption isotherm of C–S–H in cement paste. *Microporous and Mesoporous Materials* **2013,** *178*, 99.

87. Bede, A., et al., Revealing the influence of water-cement ratio on the pore size distribution in hydrated cement paste by using cyclohexane. *AIP Conference Proceedings* **2017,** *1917* (1).

88. McDonald, P. J., et al., Characterisation of intra- and inter-C–S–H gel pore water in white cement based on an analysis of NMR signal amplitudes as a function of water content. *Cement and Concrete Research* **2010,** *40* (12), 1656.

89. BLINC, R., et al., NMR Relaxation Study of Adsorbed Water in Cement and C3S Pastes. *Journal of the American Ceramic Society* **1978,** *61* (1-2), 35.

90. Korb, J. P., NMR and nuclear spin relaxation of cement and concrete materials. *Current Opinion in Colloid & Interface Science* **2009,** *14* (3), 192.

91. Valori, A. Characterisation of Cementitious Materials by 1H NMR. University of Surrey, Guildford, 2009.

92. Liu, L., et al., Application of Low-Field NMR to the Pore Structure of Concrete. *Applied Magnetic Resonance* **2021,** *52* (1), 15.

93. Enjilela, R., et al., T1-T2* relaxation correlation measurements. *Journal of Magnetic Resonance* **2021,** *326*, 106961.

94. Song, Y. Q., et al., T1–T2 Correlation Spectra Obtained Using a Fast Two-Dimensional Laplace Inversion. *Journal of Magnetic Resonance* **2002,** *154* (2), 261.

95. Korb, J. P., et al., Microstructure and texture of hydrated cement-based materials: A proton field cycling relaxometry approach. *Cement and Concrete Research* **2007,** *37* (3), 295.

96. Muncaci, S., et al., Frequency-dependent NMR relaxation of liquids confined inside porous media containing an increased amount of magnetic impurities. *Magnetic Resonance in Chemistry* **2013,** *51* (2), 123.

97. Korb, J. P., et al., Translational diffusion of liquids at surfaces of microporous materials: Theoretical analysis of field-cycling magnetic relaxation measurements. *Physical Review E* **1997,** *56* (2), 1934.

98. Badea, C., et al., The effect of silica fume on early hydration of white Portland cement via fast field cycling-NMR relaxometry. *AIP Conference Proceedings* **2017,** *1917* (1).

99. Badea, C., et al., The Effect of Curing Temperature on Early Hydration of Gray Cement Via Fast Field Cycling-NMR Relaxometry. *Applied Magnetic Resonance* **2014,** *45* (12), 1299.

100. Petrov, O., et al., A study of freezing–melting hysteresis of water in different porous materials. Part II: surfactant-templated silicas. *Physical Chemistry Chemical Physics* **2011,** *13* (36), 16358.

101. Petrov, O. V., et al., NMR cryoporometry: Principles, applications and potential. *Progress in Nuclear Magnetic Resonance Spectroscopy* **2009,** *54* (2), 97.

102. Mitchell, J., et al., Nuclear magnetic resonance cryoporometry. *Physics Reports* **2008,** *461* (1), 1.

103. Valckenborg, R. M. E., et al., Combined NMR cryoporometry and relaxometry. *Journal of Physics D: Applied Physics* **2002,** *35* (3), 249.

104. Kimmich, R., *NMR Tomography, Diffusometry, Relaxometry*. 2019.

105. Johnson, C. S., Diffusion ordered nuclear magnetic resonance spectroscopy: principles and applications. *Progress in Nuclear Magnetic Resonance Spectroscopy* **1999,** *34* (3), 203.

106. Cho, C.-H., et al., Water self-diffusion in chlorella sp. studied by pulse field gradient NMR. *Magnetic Resonance Imaging* **2003,** *21* (9), 1009.

107. Anisimov, A. V., et al., Water diffusion in biological porous systems: a NMR approach. *Magnetic Resonance Imaging* **1998,** *16* (5), 565.

108. Valiullin, R., et al., Time dependent self-diffusion coefficient of molecules in porous media. *The Journal of Chemical Physics* **2001,** *114* (1), 452.

109. Brand, T., et al., Intermolecular interaction as investigated by NOE and diffusion studies. *Progress in Nuclear Magnetic Resonance Spectroscopy* **2005,** *46* (4), 159.

110. Meiboom, S., et al., Modified Spin-Echo Method for Measuring Nuclear Relaxation Times. *Review of Scientific Instruments* **1958,** *29* (8), 688.

111. Does, M. D., et al. *MERA Toolbox (1D,2D Multi-exponential Relaxation Analysis)*, 2.02 Vanderbilt University.

112. Coates, G. R., et al. In *NMR logging : principles and applications*, 1999.

113. Bortolotti, V., et al., I2DUPEN: Improved 2DUPEN algorithm for inversion of two-dimensional NMR data. *Microporous and Mesoporous Materials* **2018,** *269*, 195.

114. Mills, R., Self-diffusion in normal and heavy water in the range 1-45.deg. *The Journal of Physical Chemistry* **1973,** *77* (5), 685.

115. Crank, J., *The mathematics of diffusion*. Oxford university press: 1979.

116. Ammann, C., et al., A simple multinuclear NMR thermometer. *Journal of Magnetic Resonance (1969)* **1982,** *46* (2), 319.

117. C1308-08(2017), A., Standard Test Method for Accelerated Leach Test for Diffusive Releases from Solidified Waste and a Computer Program to Model Diffusive, Fractional Leaching from Cylindrical Waste Forms ASTM International: West Conshohocken, PA,, 2017.

118. Chen, H., et al., 200 years of Portland cement: Technological advancements and sustainability challenges. *Journal of Cleaner Production* **2025,** *486*, 144500.

119. Aïtcin, P. C., 1 - The importance of the water–cement and water–binder ratios. In *Science and Technology of Concrete Admixtures*, Aïtcin, P.-C.; Flatt, R. J., Eds. Woodhead Publishing: 2016; pp 3.

120. Ojovan, M. I., et al., Chapter 15 - Immobilisation of Radioactive Wastes in Cement. In *An Introduction to Nuclear Waste Immobilisation*, Ojovan, M. I.; Lee, W. E., Eds. Elsevier: Oxford, 2005; pp 179.

121. Aïtcin, P. C., 2 - Phenomenology of cement hydration. In *Science and Technology of Concrete Admixtures*, Aïtcin, P.-C.; Flatt, R. J., Eds. Woodhead Publishing: 2016; pp 15.

122. Jensen, O. M., et al., Water-entrained cement-based materials: I. Principles and theoretical background. *Cement and Concrete Research* **2001,** *31* (4), 647.

123. Nadelman, E. I., et al., Application of Powers' model to modern portland and portland limestone cement pastes. *Journal of the American Ceramic Society* **2017,** *100* (9), 4219.

124. Pop, A., et al., The Effects of Different Superplasticizers and Water-to-Cement Ratios on the Hydration of Gray Cement Using T2-NMR. *Applied Magnetic Resonance* **2013,** *44* (10), 1223.

125. Papp, V., et al., Effect of metakaolin and fly ash on the early hydration and pore structure of Portland cement. *Cement and Concrete Research* **2025,** *196*, 107928.

126. Snoeck, D., et al., Comparison of different techniques to study the nanostructure and the microstructure of cementitious materials with and without superabsorbent polymers. *Construction and Building Materials* **2019,** *223*, 244.

127. Kurihara, R., et al., Surface area development of Portland cement paste during hydration: Direct comparison with 1H NMR relaxometry and water vapor/nitrogen sorption. *Cement and Concrete Research* **2022,** *157*, 106805.

128. Zhang, H., et al., Surface relaxation and permeability of cement pastes with hydrophobic agent: Combining 1H NMR and BET. *Construction and Building Materials* **2021,** *311*, 125264.

129. Schulte Holthausen, R., et al., A phenomenological approach on the influence of paramagnetic iron in cement stone on 2D T1-T2 relaxation in single-sided 1H nuclear magnetic resonance. *Cement and Concrete Research* **2019,** *120*, 279.
130. Dalas, F., et al., Surface Relaxivity of Cement Hydrates. *The Journal of Physical Chemistry C* **2014,** *118* (16), 8387.
131. Joseph, S., et al., Microstructural analysis of cement paste blended with blast furnace slag using 1H NMR relaxometry. *Cement and Concrete Composites* **2024,** *146*, 105377.
132. Bryar, T. R., et al., Paramagnetic Effects of Iron(III) Species on Nuclear Magnetic Relaxation of Fluid Protons in Porous Media. *Journal of Magnetic Resonance* **2000,** *142* (1), 74.
133. Zhou, C., et al., Pore-size resolved water vapor adsorption kinetics of white cement mortars as viewed from proton NMR relaxation. *Cement and Concrete Research* **2018,** *105*, 31.
134. Song, Y., et al., Pore structure characterization of saturated cement-based materials by nuclear magnetic resonance considering water sensitivity. *Journal of Building Engineering* **2025,** *101*, 111868.
135. Wang, X., et al., Pore Structure Damages in Cement-Based Materials by Mercury Intrusion: A Non-Destructive Assessment by X-Ray Computed Tomography. *Materials* **2019,** *12* (14), 2220.
136. Ma, H., Mercury intrusion porosimetry in concrete technology: tips in measurement, pore structure parameter acquisition and application. *Journal of Porous Materials* **2014,** *21* (2), 207.
137. Song, Y., et al., Pore Structure Characterization of Hardened Cement Paste by Multiple Methods. *Advances in Materials Science and Engineering* **2019,** *2019* (1), 3726953.
138. Dubinin, M. In *The equation of the characteristic curve of activated charcoal*, Dokl. Akad. Nauk. SSSR., 1947; pp 327.
139. Barrett, E. P., et al., The Determination of Pore Volume and Area Distributions in Porous Substances. I. Computations from Nitrogen Isotherms. *Journal of the American Chemical Society* **1951,** *73* (1), 373.
140. Brunauer, S., et al., Adsorption of Gases in Multimolecular Layers. *Journal of the American Chemical Society* **1938,** *60* (2), 309.
141. Odler, I., The BET-specific surface area of hydrated Portland cement and related materials. *Cement and Concrete Research* **2003,** *33* (12), 2049.
142. Korpa, A., et al., The influence of different drying methods on cement paste microstructures as reflected by gas adsorption: Comparison between freeze-drying (F-drying), D-drying, P-drying and oven-drying methods. *Cement and Concrete Research* **2006,** *36* (4), 634.
143. Abdolhosseini Qomi, M. J., et al., Advances in atomistic modeling and understanding of drying shrinkage in cementitious materials. *Cement and Concrete Research* **2021,** *148*, 106536.
144. Gajewicz, A. M., et al., A 1H NMR relaxometry investigation of gel-pore drying shrinkage in cement pastes. *Cement and Concrete Research* **2016,** *86*, 12.
145. HANSEN, W., Drying Shrinkage Mechanisms in Portland Cement Paste. *Journal of the American Ceramic Society* **1987,** *70* (5), 323.
146. Thomas, J. J., et al., Structural Changes to the Calcium–Silicate–Hydrate Gel Phase of Hydrated Cement with Age, Drying, and Resaturation. *Journal of the American Ceramic Society* **2008,** *91* (10), 3362.
147. Maruyama, I., Multi-scale Review for Possible Mechanisms of Natural Frequency Change of Reinforced Concrete Structures under an Ordinary Drying Condition. *Journal of Advanced Concrete Technology* **2016,** *14* (11), 691.

148. Soja, W., et al., Evolution of microstructural changes in cement paste during environmental drying. *Cement and Concrete Research* **2020,** *134*, 106093.
149. Igami, R., et al., Full-scale observation of drying-induced microstructure change in hardened cement paste by water and 2-propanol 1H NMR relaxometry. *Cement and Concrete Research* **2024,** *186*, 107698.
150. Muller, A. C. A., et al., Densification of C–S–H Measured by 1H NMR Relaxometry. *The Journal of Physical Chemistry C* **2013,** *117* (1), 403.
151. Maruyama, I., et al., Surface area changes in C3S paste during the first drying analyzed by 1H NMR relaxometry. *Cement and Concrete Research* **2022,** *156*, 106762.
152. Maruyama, I., et al., Dynamic microstructural evolution of hardened cement paste during first drying monitored by 1H NMR relaxometry. *Cement and Concrete Research* **2019,** *122*, 107.
153. Maillet, B., et al., Dynamic NMR Relaxometry as a Simple Tool for Measuring Liquid Transfers and Characterizing Surface and Structure Evolution in Porous Media. *Langmuir* **2022,** *38* (49), 15009.
154. Degefa, A. B., et al., Machine learning applied to predicting phase assemblages of hardened cementitious systems. *Ceramics International* **2024,** *50* (10), 17783.
155. Moghaddam, F., et al., The effect of fly ash fineness on heat of hydration, microstructure, flow and compressive strength of blended cement pastes. *Case Studies in Construction Materials* **2019,** *10*, e00218.
156. She, A., et al., Probing the hydration of composite cement pastes containing fly ash and silica fume by proton NMR spin-lattice relaxation. *Science China Technological Sciences* **2010,** *53* (6), 1471.
157. *Handling and Processing of Radioactive Waste from Nuclear Applications*. INTERNATIONAL ATOMIC ENERGY AGENCY: Vienna, 2001.
158. Bligh, M. W., et al., Investigation of early hydration dynamics and microstructural development in ordinary Portland cement using 1H NMR relaxometry and isothermal calorimetry. *Cement and Concrete Research* **2016,** *83*, 131.
159. John, E., et al., Cement hydration mechanisms through time – a review. *Journal of Materials Science* **2023,** *58* (24), 9805.
160. Rahimi-Aghdam, S., et al., Cement hydration from hours to centuries controlled by diffusion through barrier shells of C-S-H. *Journal of the Mechanics and Physics of Solids* **2017,** *99*, 211.
161. Tang, Y.-J., et al., Low-Field Nuclear Magnetic Resonance Investigation on Early Hydration Characterization of Cement Paste Mixed with Mineral Admixtures. *Buildings* **2023,** *13* (9), 2318.
162. Walkley, B., et al., Solid-state nuclear magnetic resonance spectroscopy of cements. *Materials Today Advances* **2019,** *1*, 100007.
163. Faure, P. F., et al., Proton NMR relaxation as a probe for setting cement pastes. *Magnetic Resonance Imaging* **2008,** *26* (8), 1183.
164. Lothenbach, B., et al., Supplementary cementitious materials. *Cement and Concrete Research* **2011,** *41* (12), 1244.
165. Marchon, D., et al., 12 - Impact of chemical admixtures on cement hydration. In *Science and Technology of Concrete Admixtures*, Aïtcin, P.-C.; Flatt, R. J., Eds. Woodhead Publishing: 2016; pp 279.
166. Liu, H., et al., A novel method for semi-quantitative analysis of hydration degree of cement by 1H low-field NMR. *Cement and Concrete Research* **2021,** *141*, 106329.
167. Mardani-Aghabaglou, A., et al., Comparison of fly ash, silica fume and metakaolin from mechanical properties and durability performance of mortar mixtures view point. *Construction and Building Materials* **2014,** *70*, 17.

168. Skibsted, J., et al., Reactivity of supplementary cementitious materials (SCMs) in cement blends. *Cement and Concrete Research* **2019,** *124*, 105799.
169. Saboo, N., et al., Effect of fly ash and metakaolin on pervious concrete properties. *Construction and Building Materials* **2019,** *223*, 322.
170. Snellings, R., et al., Future and emerging supplementary cementitious materials. *Cement and Concrete Research* **2023,** *171*, 107199.
171. Aïtcin, P. C., 4 - Supplementary cementitious materials and blended cements. In *Science and Technology of Concrete Admixtures*, Aïtcin, P.-C.; Flatt, R. J., Eds. Woodhead Publishing: 2016; pp 53.
172. Lagier, F., et al., Influence of Portland cement composition on early age reactions with metakaolin. *Cement and Concrete Research* **2007,** *37* (10), 1411.
173. Justice, J. M., et al., Influence of Metakaolin Surface Area on Properties of Cement-Based Materials. *Journal of Materials in Civil Engineering* **2007,** *19* (9), 762.
174. Faux, D., et al., Advances in the Interpretation of Frequency-Dependent Nuclear Magnetic Resonance Measurements from Porous Material. *Molecules* **2019,** *24* (20), 3688.
175. Faux, D. A., et al., A model for the interpretation of nuclear magnetic resonance spin-lattice dispersion measurements on mortar, plaster paste, synthetic clay and oil-bearing shale. *Microporous and Mesoporous Materials* **2018,** *269*, 39.
176. Kogon, R., et al., 3TM: Software for the 3-Tau Model. *SoftwareX* **2022,** *17*, 100979.
177. Scrivener, K. L., et al., Hydration of cementitious materials, present and future. *Cement and Concrete Research* **2011,** *41* (7), 651.
178. Matsushima, T., Desorption Kinetics☆. In *Encyclopedia of Interfacial Chemistry*, Wandelt, K., Ed. Elsevier: Oxford, 2018; pp 59.
179. Frías, M., et al., The effect that the pozzolanic reaction of metakaolin has on the heat evolution in metakaolin-cement mortars. *Cement and Concrete Research* **2000,** *30* (2), 209.
180. Chindaprasirt, P., et al., Effect of fly ash fineness on microstructure of blended cement paste. *Construction and Building Materials* **2007,** *21* (7), 1534.
181. Godefroy, S., et al., Surface nuclear magnetic relaxation and dynamics of water and oil in macroporous media. *Physical Review E* **2001,** *64* (2), 021605.
182. Milestone, N. B., Reactions in cement encapsulated nuclear wastes: need for toolbox of different cement types. *Advances in Applied Ceramics* **2006,** *105* (1), 13.
183. Collepardi, M. M., 6 - Water Reducers/Retarders. In *Concrete Admixtures Handbook (Second Edition)*, Ramachandran, V. S., Ed. William Andrew Publishing: Park Ridge, NJ, 1996; pp 286.
184. Dransfield, J., 4 - Admixtures for concrete, mortar and grout. In *Advanced Concrete Technology*, Newman, J.; Choo, B. S., Eds. Butterworth-Heinemann: Oxford, 2003; pp 3.
185. Glasser, F. P., Mineralogical aspects of cement in radioactive waste disposal. *Mineralogical Magazine* **2001,** *65* (5), 621.
186. Crawford, R. W., et al., Instrinsic sorption potential of cement components for 134Cs. *Cement and Concrete Research* **1984,** *14* (4), 595.
187. Evans, N. D. M., Binding mechanisms of radionuclides to cement. *Cement and Concrete Research* **2008,** *38* (4), 543.
188. Bagosi, S., et al., Caesium immobilisation in hydrated calcium-silicate-aluminate systems. *Cement and Concrete Research* **1998,** *28* (12), 1753.
189. Glasser, F. P., Fundamental aspects of cement solidification and stabilisation. *Journal of Hazardous Materials* **1997,** *52* (2), 151.
190. Bourchy, A., et al., The evolution of hydrated lime-based cementitious waste forms during leach testing leading to enhanced technetium retention. *Journal of Hazardous Materials* **2022,** *430*, 128507.

191. Tallent, O. K., et al., Immobilization of Technetium and Nitrate in Cement-Based Materials. *MRS Proceedings* **1987,** *112*, 23.

192. Gillispie, E. C., et al., Competitive TcO4–, IO3–, and CrO42– Incorporation into Ettringite. *Environmental Science & Technology* **2021,** *55* (2), 1057.

193. Jiménez, A., et al., Thermal Stability of Ettringite Exposed to Atmosphere: Implications for the Uptake of Harmful Ions by Cement. *Environmental Science & Technology* **2015,** *49* (13), 7957.

194. Saslow, S. A., et al., Immobilizing Pertechnetate in Ettringite via Sulfate Substitution. *Environmental Science & Technology* **2020,** *54* (21), 13610.

195. Felipe-Sotelo, M., et al., The solubility of nickel and its migration through the cementitious backfill of a geological disposal facility for nuclear waste. *Journal of Hazardous Materials* **2016,** *314*, 211.

196. Ochs, M., et al., Solubility of Radionuclides in Fresh and Leached Cementitious Systems at 22°C and 50°C. *MRS Online Proceedings Library* **1997,** *506* (1), 773.

197. Lövgren, L. In *Effects of complexing compounds on sorption of metal ions to cement*, 2006.

198. Smillie, S., et al., Reaction of EDTA, oxalic acid and citric acid with Portland cement. *Advances in Cement Research* **1999,** *11*, 97.

199. Guidone, R. E., et al., Citrate sorption on cement hydrates. *Cement and Concrete Research* **2024,** *178*, 107404.

200. Nemes, Z., et al., Kinetics of strontium ion adsorption on natural clay samples. *Journal of Radioanalytical and Nuclear Chemistry* **2005,** *266* (2), 289.

201. Barnes, C. J., et al., Chapter 5 - Isotopic Exchange in Soil Water. In *Isotope Tracers in Catchment Hydrology*, Kendall, C.; McDonnell, J. J., Eds. Elsevier: Amsterdam, 1998; pp 137.

202. Whitaker, S., Diffusion and dispersion in porous media. *AIChE Journal* **1967,** *13* (3), 420.

203. Sharma, R., et al., Cesium immobilization of high pH and low pH belite-rich cement under varying temperature. *Journal of Hazardous Materials* **2024,** *469*, 133995.

204. Pescatore, C., Improved expressions for modeling diffusive, fractional cumulative leaching from finite-size waste forms. *Waste Management* **1990,** *10* (2), 155.

205. Guerrero, A., et al., Cemented materials in the LLW and MLW Spanish disposal. *Materiales de Construcción* **1999,** *49* (255), 31.

206. El-Kamash, A. M., et al., Immobilization of cesium and strontium radionuclides in zeolite-cement blends. *Journal of Hazardous Materials* **2006,** *136* (2), 310.

207. Wang, G. C., 7 - Environmental aspects of slag utilization. In *The Utilization of Slag in Civil Infrastructure Construction*, Wang, G. C., Ed. Woodhead Publishing: 2016; pp 131.

208. Zhu, Y., et al., Advances in immobilization of radionuclide wastes by alkali activated cement and related materials. *Cement and Concrete Composites* **2022,** *126*, 104377.

209. Song, F., et al., Leaching behavior of heavy metals from sewage sludge solidified by cement-based binders. *Chemosphere* **2013,** *92* (4), 344.

210. Means, J. L., et al., The environmental biogeochemistry of chelating agents and recommendations for the disposal of chelated radioactive wastes. *Nuclear and Chemical Waste Management* **1981,** *2* (3), 183.

211. Mathuthu, E., et al., EDTA as a chelating agent in quantitative 1H-NMR of biologically important ions. *Biochemistry and Cell Biology* **2021,** *99* (4), 465.

212. Hafer, E., et al., Qualitative and quantitative 1H NMR spectroscopy for determination of divalent metal cation concentration in model salt solutions, food supplements, and pharmaceutical products by using EDTA as chelating agent. *Magnetic Resonance in Chemistry* **2020,** *58* (7), 653.

213. Han, S., et al., Determination of the Concentrations of Metal Cations in Aqueous Solutions Using Proton NMR Spectral Area Integration of the EDTA Complexes. *Journal of Solution Chemistry* **2004,** *33* (3), 301.
214. Monakhova, Y. B., et al., Rapid NMR determination of inorganic cations in food matrices: Application to mineral water. *Food Chemistry* **2017,** *221*, 1828.
215. Jószai, R., et al., Multinuclear NMR and DFT studies of the structure and fluxionality for MIII–ethylenediamine-tetraacetate complexes (M(EDTA)−, M=Al, Ga and In) in solution. *Journal of Molecular Liquids* **2007,** *131-132*, 72.
216. Grant, M. W., et al., The structure of nickel(II)–ethylenediaminetetra-acetic acid complexes in aqueous solution determined by 17O nuclear magnetic resonance. *Journal of the Chemical Society D: Chemical Communications* **1970,** (21), 1446.
217. Means, J. L., et al., Migration of Radioactive Wastes: Radionuclide Mobilization by Complexing Agents. *Science* **1978,** *200* (4349), 1477.
218. Brooks, S. C., et al., Reactive transport of EDTA-complexed cobalt in the presence of ferrihydrite. *Geochimica et Cosmochimica Acta* **1996,** *60* (11), 1899.
219. D, J. V., Stability constants of metal-ion complexes (Sillen, Lars Gunnar; Martell, Arthur E.). *Journal of Chemical Education* **1965,** *42* (9), 521.
220. Eddy, M. A., et al., Characterization of a Ternary Neodymium-HEDTA-Citrate Complex in the Actinide Lanthanide Separation Process. *ACS Omega* **2022,** *7* (17), 15005.
221. Sherry, A. D., et al., Nuclear magnetic resonance study of the interaction of neodymium(III) with amino acids and carboxylic acids. Aqueous shift reagent. *Journal of the American Chemical Society* **1973,** *95* (9), 3011.
222. Fernández, C. O., et al., Probing the metal site in Rhus vernicifera stellacyanin by Ni(II) substitution and paramagnetic NMR spectroscopy. *Inorganica Chimica Acta* **1998,** *273* (1), 367.
223. Gácsi, A., et al., Some aspects of the aqueous solution chemistry of the Na+/Ca2+/OH−/Cit3− system: The structure of a new calcium citrate complex forming under hyperalkaline conditions. *Journal of Molecular Structure* **2016,** *1118*, 110.
224. Bodor, A., et al., 1H- and 13C-NMR as tools to study aluminium coordination chemistry—aqueous Al(III)–citrate complexes. *Coordination Chemistry Reviews* **2002,** *228* (2), 175.
225. Stuyck, W., et al., Selective defunctionalization of citric acid to tricarballylic acid as a precursor for the production of high-value plasticizers. *Green Chemistry* **2020,** *22* (22), 7812.
226. Wyrzykowski, D., et al., Thermal behaviour of citric acid and isomeric aconitic acids. *Journal of Thermal Analysis and Calorimetry* **2011,** *104* (2), 731.
227. Silva, A. M. N., et al., Determination of the pKa value of the hydroxyl group in the α-hydroxycarboxylates citrate, malate and lactate by 13C NMR: implications for metal coordination in biological systems. *BioMetals* **2009,** *22* (5), 771.
228. Behnood, A., et al., Methods for measuring pH in concrete: A review. *Construction and Building Materials* **2016,** *105*, 176.
229. De Bruyne, A., et al., Efficient two-step production of biobased plasticizers: dehydration-hydrogenation of citric acid followed by Fischer esterification. *Green Chemistry* **2023,** *25* (10), 3896.
230. Atkins, M., et al., Application of portland cement-based materials to radioactive waste immobilization. *Waste Management* **1992,** *12* (2), 105.
231. Yang, H., et al., Application of layered double hydroxides (LDHs) in corrosion resistance of reinforced concrete-state of the art. *Construction and Building Materials* **2021,** *307*, 124991.
232. Li, Y., et al., Structure and lithium storage performances of nickel hydroxides synthesized with different nickel salts. *Ionics* **2017,** *23* (7), 1625.

233. Zheng, W., et al., Sulfidation of Hierarchical NiAl−LDH/Ni−MOF Composite for High-Performance Supercapacitor. *ChemElectroChem* **2019,** *6* (13), 3375.
234. Wang, X., et al., Formation of Friedel's salt using steel slag and potash mine brine water. *Construction and Building Materials* **2019,** *220*, 119.
235. Talero, R., et al., Morphological Differentiation and Crystal Growth Form of Friedel's Salt Originated from Pozzolan and Portland Cement. *Industrial & Engineering Chemistry Research* **2012,** *51* (38), 12517.
236. Suryavanshi, A. K., et al., Mechanism of Friedel's salt formation in cements rich in tri-calcium aluminate. *Cement and Concrete Research* **1996,** *26* (5), 717.
237. Choi, H., et al., Effect of Addition of Ca2+ and CO32? Ions with Temperature Control on Self-Healing of Hardened Cement Paste. *Materials* **2019,** *12* (15), 2456.
238. Jiang, J., et al., Calcite crystallization in the cement system: morphological diversity, growth mechanism and shape evolution. *Physical Chemistry Chemical Physics* **2018,** *20* (20), 14174.
239. Thomas, N. L., et al., The hydration of Portland cement, C3S and C2S in the presence of a calcium complexing admixture (EDTA). *Cement and Concrete Research* **1983,** *13* (3), 391.
240. Wang, J., et al., Effect of disodium EDTA on hydration and mechanical properties of calcium sulphoaluminate-belite cement. *Cement and Concrete Research* **2023,** *164*, 107041.
241. Gera, J. H. a. F., Understanding what happens underground. *IAEA Bulletin* **1985,** *27* (2), 35.
242. Glasser, F. P., et al., Cements in Radioactive Waste Disposal. *MRS Bulletin* **1994,** *19* (12), 33.
243. Salles, F., et al., A calorimetric study of mesoscopic swelling and hydration sequence in solid Na-montmorillonite. *Applied Clay Science* **2008,** *39* (3), 186.
244. Meleshyn, A., et al., The gap between crystalline and osmotic swelling of Na-montmorillonite: A Monte Carlo study. *The Journal of Chemical Physics* **2004,** *122* (3), 034705.
245. Ohkubo, T., et al., Pore distribution of compacted Ca-montmorillonite using NMR relaxometry and cryoporometry: Comparison with Na-montmorillonite. *Microporous and Mesoporous Materials* **2021,** *313*, 110841.
246. Segad, M., et al., Ca/Na Montmorillonite: Structure, Forces and Swelling Properties. *Langmuir* **2010,** *26* (8), 5782.
247. Katti, D. R., et al., Molecular modeling of initiation of interlayer swelling in Na–montmorillonite expansive clay. *Canadian Geotechnical Journal* **2015,** *52* (9), 1385.
248. Cheng, K., et al., Combined interpretation of NMR and TGA measurements to quantify the impact of relative humidity on hydration of clay minerals. *Applied Clay Science* **2017,** *143*, 362.
249. Magzoub, M. I., et al., An Investigation of the Swelling Kinetics of Bentonite Systems Using Particle Size Analysis. *Journal of Dispersion Science and Technology* **2020,** *41* (6), 817.
250. Eizaguirre, P., et al., Exploring two regimes of water mobility in unsaturated expansive clay using NMR relaxometry. *Applied Clay Science* **2024,** *251*, 107324.
251. Nakashima, Y., Pulsed field gradient proton NMR study of the self-diffusion of H2O in montmorillonite gel: Effects of temperature and water fraction. *American Mineralogist* **2001,** *86* (1-2), 132.
252. Porion, P., et al., Water Mobility within Compacted Clay Samples: Multi-Scale Analysis Exploiting 1H NMR Pulsed Gradient Spin Echo and Magnetic Resonance Imaging of Water Density Profiles. *ACS Omega* **2018,** *3* (7), 7399.

253. Pradhan, S. M., et al., Evolution of Molecular Interactions in the Interlayer of Na-Montmorillonite Swelling Clay with Increasing Hydration. *International Journal of Geomechanics* **2015,** *15* (5), 04014073.
254. Wang, B., et al., A diffusion model for the swelling of compacted Na–montmorillonite in water. *Applied Clay Science* **2021,** *214*, 106301.
255. Laird, D. A., Influence of layer charge on swelling of smectites. *Applied Clay Science* **2006,** *34* (1), 74.
256. Papp, V., et al., Structure and Swelling Properties of Biodegradable Cross-Linked Polyurethanes by Means of Nuclear Magnetic Resonance. *The Journal of Physical Chemistry B* **2025,** *129* (22), 5607.
257. Tran, H. N., et al., Mistakes and inconsistencies regarding adsorption of contaminants from aqueous solutions: A critical review. *Water Research* **2017,** *120*, 88.
258. Schott, H., Swelling kinetics of polymers. *Journal of Macromolecular Science, Part B* **1992,** *31* (1), 1.
259. Schott, H., Kinetics of swelling of polymers and their gels. *Journal of Pharmaceutical Sciences* **1992,** *81* (5), 467.
260. Adnadjevic, B., et al., Novel approach in investigation of the poly(acrylic acid) hydrogel swelling kinetics in water. *Journal of Applied Polymer Science* **2008,** *107* (6), 3579.
261. Forgács, A., et al., Mechanism of Hydration and Hydration Induced Structural Changes of Calcium Alginate Aerogel. *ACS Applied Materials & Interfaces* **2021,** *13* (2), 2997.
262. Dvinskikh, S. V., et al. *Magnetic resonance imaging and nuclear magnetic resonance investigations of bentonite systems*; 2009.
263. Graczyk, K. M., et al., Predicting porosity, permeability, and tortuosity of porous media from images by deep learning. *Scientific Reports* **2020,** *10* (1), 21488.
264. Koponen, A., et al., Permeability and effective porosity of porous media. *Physical Review E* **1997,** *56* (3), 3319.
265. *Geological Disposal Facilities for Radioactive Waste*. INTERNATIONAL ATOMIC ENERGY AGENCY: Vienna, 2011.
266. Plastino, A., et al., Combining classification and regression for improving permeability estimations from 1H NMR relaxation data. *Journal of Applied Geophysics* **2017,** *146*, 95.
267. Testamanti, M. N., et al., Determination of NMR T2 cut-off for clay bound water in shales: A case study of Carynginia Formation, Perth Basin, Western Australia. *Journal of Petroleum Science and Engineering* **2017,** *149*, 497.
268. Daigle, H., et al., Extending NMR data for permeability estimation in fine-grained sediments. *Marine and Petroleum Geology* **2009,** *26* (8), 1419.
269. Rios, E. H., et al., Modeling rock permeability from NMR relaxation data by PLS regression. *Journal of Applied Geophysics* **2011,** *75* (4), 631.
270. Cui, Y., et al., A numerical study of field strength and clay morphology impact on NMR transverse relaxation in sandstones. *Journal of Petroleum Science and Engineering* **2021,** *202*, 108521.
271. Pape, H., et al., Permeability Prediction for Low Porosity Rocks by Mobile NMR. 2009; Vol. 166, pp 1125.
272. Wei, D.-F., et al., Estimation of Permeability from NMR Logs Based on Formation Classification Method in Tight Gas Sands. *Acta Geophysica* **2015,** *63* (5), 1316.
273. Kenyon, W. E., et al., A Three-Part Study of NMR Longitudinal Relaxation Properties of Water-Saturated Sandstones. *SPE Formation Evaluation* **1988,** *3* (03), 622.
274. Coates, G. R., et al. In *The MRIL In Conoco 33-1 An Investigation Of A New Magnetic Resonance Imaging Log*, SPWLA 32nd Annual Logging Symposium, 1991.

275. Mao, Z.-q., et al., Estimation of Permeability by Integrating Nuclear Magnetic Resonance (NMR) Logs with Mercury Injection Capillary Pressure (MICP) Data in Tight Gas Sands. *Applied Magnetic Resonance* **2013,** *44* (4), 449.
276. Bernáth Gy., K. A. C., Szongoth G., Csabafi R., Gúthy T., Zilahi-Sebess L., Mélyfúrás-geofizikai és VSP mérési eredmények a BAF -2 és BAF-1, -1A, -1Af fúrásokban. In *Bodai Agyagkő Formáció kutatás szakmai előadói nap kiadványa*, 2018; pp 36.
277. Bianchi, M., et al., Radionuclide Transport Behavior in a Generic Geological Radioactive Waste Repository. *Groundwater* **2015,** *53* (3), 440.

10. Publications and conferences

Publications related to the dissertation

1. **V. Papp,** I. Ardelean, A. Bulátkó, K. László, A. Csík, R. Janovics, M. Kéri: ***Effect of metakaolin and fly ash on the early hydration and pore structure of Portland cement***, Cement and Concrete Research **2025**, Volume 196, 107928. https://doi.org/10.1016/j.cemconres.2025.107928
2. **V. Papp,** B. Vadkerti, I. Bányai, S. Kéki, M. Kéri: ***Structure and Swelling Properties of Biodegradable Cross-Linked Polyurethanes by Means of Nuclear Magnetic Resonance***, The Journal of Physical Chemistry B **2025**, 129 (22), 5607-5620. https://doi.org/10.1021/acs.jpcb.5c01046
3. **V. Papp**, R. Janovics, M. Kéri: ***NMR characterization of the permeability and structure of Boda Claystone Formation (BCF)***, Scientia et Securitas **2024**, 4(4), 285-293. https://doi.org/10.1556/112.2023.00187
4. **Papp V.,** Papp I., Janovics R., Nemes Z., Kéri M.: ***Radioaktív hulladékok komplexképző tartalmának hatása a kötőanyag szerkezetére és kioldhatóságára***, Sugárvédelem **2024**, XVII. évf. 1. szám 1-14.
5. **V. Papp**, R. Janovics, T. P. Kertész, Z. Nemes, T. Fodor, I. Bányai, M. Kéri: ***State and role of water confined in cement and composites modified with metakaolin and additives***, Journal of Molecular Liquids **2023**, 388, 122716. https://doi.org/10.1016/j.molliq.2023.122716
6. **Papp V.,** Janovics R., Nemes Z., Kéri M.: ***Cementkő mátrixok rehidratációjának NMR spektroszkópiás vizsgálata***, XXIV. Tavaszi Szél Konferencia kiadvány **2021**, 536-550. ISBN 978-615-81991-1-7

Other publications

7. A. Forgács, **V. Papp**, G. Paul, L. Marchese, A. Len, Z. Dudás, I.Fábián, P. Gurikov, J. Kalmár: ***Mechanism of Hydration and Hydration Induced Structural Changes of Calcium Alginate Aerogel,*** ACS Applied Materials & Interfaces **2021**,13, 2, 2997–3010. https://doi.org/10.1021/acsami.0c17012

8. M. Kéri, A. Forgács, **V. Papp**, I. Bányai, P. Veres, A. Len, Z. Dudás, J. Kalmár: ***Gelatin content governs hydration induced structural changes in silica-gelatin hybrid aerogels – Implications in drug delivery,*** Acta Biomaterialia **2020**, Vol. 105, 131-145. https://doi.org/10.1016/j.actbio.2020.01.016

9. I. Lázár, A. Forgács, A. Horváth, G. Király, G. Nagy, A. Len, Z. Dudás, **V. Papp**, Z. Balogh, K. Moldován, L. Juhász, Cs. Cserháti, Zs. Szántó, I. Fábián, J. Kalmár: ***Mechanism of Hydration of Biocompatible Silica-Casein Aerogels Probed by NMR and SANS Reveal Backbone Rigidity***, Applied Surface Science **2020**, 531. 147232. https://doi.org/10.1016/j.apsusc.2020.147232

10. **Papp V.,** Kéri M., Forgács A., Len A., Dudás Z., P. Gurikov, Kalmár J.: ***Kalandozás a nanovilágban, pórusos anyagok vizsgálata különleges módszerekkel,*** A Debreceni Egyetem Szakkollégiumainak I. Tudományos Konferenciájának Tanulmánykötete **2020**, 93-105. ISBN 978-963-490-223-2

11. **Papp V.**, Kéri M., Forgács M., Len A., Dudás Z., Kalmár J.: ***Szilika- zselatin aerogélek szerkezete és nedvesedési tulajdonságai,*** I. FKF Szimpózium Konferencia Kiadvány **2019**, 178-183. ISBN 978-615-6018-00-7

Conference presentations related to the dissertation

1. **Papp V**., Janovics R., Nemes Z., Kéri M.
   Cementkő mátrixok rehidratációjának NMR spektroszkópiás vizsgálata *(lecture presentation)*
   XXIV. Tavaszi Szél Konferencia, Kémiai és környezettudományi szekció, Gyógyszerészeti, analitikai, ipari és szintetikus kémiai alszekció
   2021.05.29-30. Online
   I. helyezés

2. **Papp V.**, Janovics R., Nemes Z., Kéri M.
   Víz a hulladéktárolóban? Avagy a rehidratáció hatása a cementkő mátrixok szerkezetére *(poster presentation)*
   II. FKF Szimpózium
   2021.06.16-18. Online

3. **Papp V.**, Janovics R., Nemes Z., Kéri M.
   Radioaktív hulladékok végleges elhelyezéséhez kapcsolódó cementkő mátrixok szerkezetének vizsgálata *(lecture presentation)*
   XLVI. Sugárvédelmi Továbbképző Tanfolyam
   2021.09.14-16. Zalakaros, Hungary
   Sugárvédelmi Nívódíj III. helyezés és Különdíj

4. **Papp V.**, Vadkerti B., Kéri M.
   Biodegradábilis keresztkötött polimerek viselkedése vizes közegben *(lecture presentation)*
   XLIV. Kémiai Előadói Napok
   2021.10.26-27. Online

5. **V. Papp**, V. Nagy, B. Vadkerti, M. Kéri
   Study of swelling biodegradable crosslinked polymers by NMR *(poster presentation)*
   10th Jubilee Interdisciplinary Doctoral Conference (*2021IDK*)
   2021.11.12-13., Pécs, Hungary

6. **V. Papp**, R. Janovics, Z. Nemes, M. Kéri
   Investigation of the structure of binders related to the final disposal of radioactive waste *(lecture presentation)*
   2021 évi ELFTSV Online Sugárvédelmi Mikulás
   2021.12.06. Online

7. **Papp V.**, Janovics R., Nemes Z., Kéri M.
   Radioaktív hulladékok végleges elhelyezéséhez kapcsolódó cementkövek szerkezetének vizsgálata *(lecture presentation)*
   HISZ Tavaszi Tudományos Hallgatói Konferencia
   2022.05.06. Debrecen, Hungary

8. **V. Papp**, R. Janovics, Z. Nemes, I. Bányai, M. Kéri
   Investigation of the structure of binders related to the final disposal of radioactive waste *(lecture presentation)*
   ATOMKI Seminar
   2022.05.24. Debrecen, Hungary

9. **V. Papp**, R. Janovics, Z. Nemes, I. Bányai, M. Kéri
   Investigation of the structure of binders related to the final disposal of radioactive waste *(lecture presentation)*
   6th European Congress on Radiation Protection
   2022.05.30.-06.03. Budapest, Hungary

10. **V. Papp**, R. Janovics, Z. Nemes, I. Bányai, M. Kéri
    NMR characterization of cement binders related to the radioactive waste conditioning *(poster presentation)*
    Chemistry Physics and Biology of Colloids and Interfaces
    2022.06.06-10. Eger, Hungary

11. **Papp V.,** Vadkerti B., Kéri M.,
    Biodegradábilis keresztkötött polimerek NMR spektroszkópiás vizsgálata *(lecture presentation)*
    DE Intézményi ÚNKP Konferencia
    2022.06.13. Debrecen, Hungary

12. **V. Papp**, R. Janovics, Z. Nemes, I. Bányai, M. Kéri

Role of water in the curing process and structure formation of cement and metakaolin-based binders *(lecture presentation)*
International Symposium on recent advances in NMR applications to materials
2022.09.16-19. Hirschegg, Austria

13. **Papp V.**, Janovics R., Nemes Z., Bányai I., Kéri M.
Geopolimerek, mint potenciális kötőanyagok a radioaktív hulladék kondicionálásban *(lecture presentation)*
Meeting with PURAM
2022.09.28. Paks, Hungary

14. **Papp V.,** Janovics R., Nemes Z., Bányai I., Kéri M.
A metakaolin szerepe a radioaktív hulladékok kondicionálása során *(lecture presentation)*
10. Környezetkémiai Szimpózium
2022.09.29-30. Siófok, Hungary

15. **Papp V.,** Janovics R., Kéri M.
Geopolimerek szerepe a radioaktív hulladékok kondicionálásában *(lecture presentation)*
Hatvani István Szakkollégium, Őszi Tudományos Hallgatói Konferencia
2022.12.08. Debrecen, Hungary

16. **V. Papp**, D. Nyul, L. Novák, I. Bányai, M. Kéri
What can liquid-phase NMR tell us about porous materials? *(poster presentation)*
Workshop on Aerogels Characterization and Modelling
2023.03.29-31. Debrecen, Hungary

17. **Papp V.**, Kertész T. P., Nyul D., Janovics R., Bányai I., Kéri M.
Mit ad a kötőanyagok megismeréséhez a folyékony fázisú NMR? *(poster presentation)*
MKE 4. Nemzeti Konferencia
2023.07.10-12. Eger, Hungary

18. **V. Papp**, R. Janovics, I. Papp, T. P. Kertész, Z. Nemes, M. Kéri
What can leach out of the cements that bind radioactive waste? *(lecture presentation)*
Alpine NMR Workshop on recent advances in NMR methods
2023.09.14-17. Mátrafüred, Hungary

19. **Papp V.**, Papp I., Janovics R., Nemes Z., Kéri M.
Radioaktív hulladékok komplexképző tartalmának hatása a kötőanyag szerkezetére és kioldhatóságára *(lecture presentation)*
HISZK 2024. évi Tavaszi Tudományos Hallgatói Konferencia
2024.05.10. Debrecen, Hungary

20. **Papp V.**, Janovics R., Kéri M.
    Kisterű NMR módszerek cement alapú kötőanyagok megismerésére *(lecture presentation)*
    NMR Munkabizottság 2024. évi Előadóülése
    2024.05.23-24. Balatonszemes, Hungary

21. **V. Papp**, R. Janovics, I. Papp, Z. Nemes, M. Kéri
    Applicability of Liquid- phase NMR to characterize the structure and leachability of cement- based binders *(lecture presentation)*
    International Atomic Energy Agency, Technical Meeting on Achievements and Challenges in Radioactive Waste Characterization
    2024. 08. 26-30 Vienna, Austria

22. **V. Papp**, R. Janovics, I. Ardelean, K. László, A. Csík, M. Kéri
    Effect of pozzolans on the early hydration and structure of Portland cement by means of NMR *(lecture presentation)*
    Alpine NMR Workshop
    2024.09.20-22. Cluj-Napoca, Romania

11. Appendix

Table A1. Diffusion coefficients (D_{1-3}) of confided water in 10-30% metakaolin (Mc10-30) and fly ash (Fc10-30) containing cement composites.

	D_1 (m^2/s)	**D_2 (m^2/s)**	**D_3 (m^2/s)**
Mc10	3.7E-11 ± 1.8E-13	7.5E-11 ± 9.3E-12	2.2E-12 ± 2.7E-14
Mc20	1.4E-11 ± 4.1E-13	2.2E-11 ± 1.9E-12	5.8E-12 ± 2.1E-14
Mc30	1.0E-11 ± 4.9E-14	5.0E-11 ± 3.9E-12	9.4E-12 ± 1.4E-12
Pc10		1.6E-10 ± 1.5E-12	5.3E-12 ± 1.4E-13
Pc20		1.5E-10 ± 2.0E-12	2.2E-12 ± 2.2E-13
Pc30		3.7E-10 ± 1.0E-11	3.8E-12 ± 2.4E-13

Table A2. The determined rate constants (k) of the leaching kinetics of ^{133}Cs, ^{60}Ni and ^{185}Re from the small sized model waste packages at T= 298 K. The standard errors (σ) of the fittings are shown.

Model ion	Complexing agent concentration									
	0 g/l		**5 g/l**		**10 g/l**		**15 g/l**		**20 g/l**	
	k	σ	k	σ	k	σ	k	σ	k	σ
^{133}Cs	**0.28**	0.02	**0.26**	0.01	**0.28**	0.01	**0.31**	0.02	**0.28**	0.01
^{60}Ni	-	-	**0.22**	0.01	**0.24**	0.02	**0.27**	0.04	**0.21**	0.01
^{185}Re	**0.28**	0.03	**0.22**	0.01	**0.25**	0.01	**0.24**	0.01	**0.24**	0.01

Table A3. The determined effective diffusion coefficients (D_e) of ^{133}Cs in the case of small sized model waste packages. The relative errors (E_{R2}) of the fittings are shown. The diffusivity of the model ion was determined using both the semi-infinite and the infinite models.

^{133}Cs	Complexing agent concentration									
	0 g/l		5 g/l		10 g/l		15 g/l		20 g/l	
	D (m^2/s)	E_{R^2} (%)	D (m^2/s)	E_{R^2} (%)	D (m^2/s)	E_{R^2} (%)	D (m^2/s)	E_{R^2} (%)	D (m^2/s)	E_{R^2} (%)
Semi-infinite	1.5E-13	157.3	1.7E-13	139.5	1.4E-13	142.6	1.7E-13	189.1	9.5E-14	118.6
Infinite	1.1E-13	0.4	9.9E-14	0.04	8.5E-14	0.3	1.5E-13	0.5	6.7E-14	0.3
	3.0E-15		5.1E-15		4.9E-15		1.8E-15		1.3E-15	

Table A4. The determined effective diffusion coefficients (D_e) of ^{60}Ni in the case of small sized model waste packages. The relative errors (E_{R2}) of the fittings are shown. The diffusivity of the model ion was determined using both the semi-infinite and the infinite models.

^{60}Ni	Complexing agent concentration									
	0 g/l		5 g/l		10 g/l		15 g/l		20 g/l	
	D (m^2/s)	E_{R^2} (%)	D (m^2/s)	E_{R^2} (%)	D (m^2/s)	E_{R^2} (%)	D (m^2/s)	E_{R^2} (%)	D (m^2/s)	E_{R^2} (%)
Semi-infinite			4.4E-16	13.6	2.5E-16	11.0	2.2E-16	22.4	7.9E-17	4.9
Infinite			3.1E-16	0.01	2.1E-16	0.04	9.1E-17	0.05	6.6E-17	0.01

Table A5. The determined effective diffusion coefficients (D_e) of ^{185}Re in the case of small sized model waste packages. The relative errors (E_{R2}) of the fittings are shown. The diffusivity of the model ion was determined using both the semi-infinite and the infinite models.

^{185}Re	Complexing agent concentration									
	0 g/l		5 g/l		10 g/l		15 g/l		20 g/l	
	D (m^2/s)	E_{R^2} (%)	D (m^2/s)	E_{R^2} (%)	D (m^2/s)	E_{R^2} (%)	D (m^2/s)	E_{R^2} (%)	D (m^2/s)	E_{R^2} (%)
Semi-infinite	4.3E-15	31.1	4.5E-14	57.4	2.8E-14	60.2	3.4E-14	78.6	1.1E-14	38.6
Infinite	5.1E-15	0.5	4.5E-14	0.03	3.0E-14	0.1	3.5E-14	0.1	1.1E-14	0.1

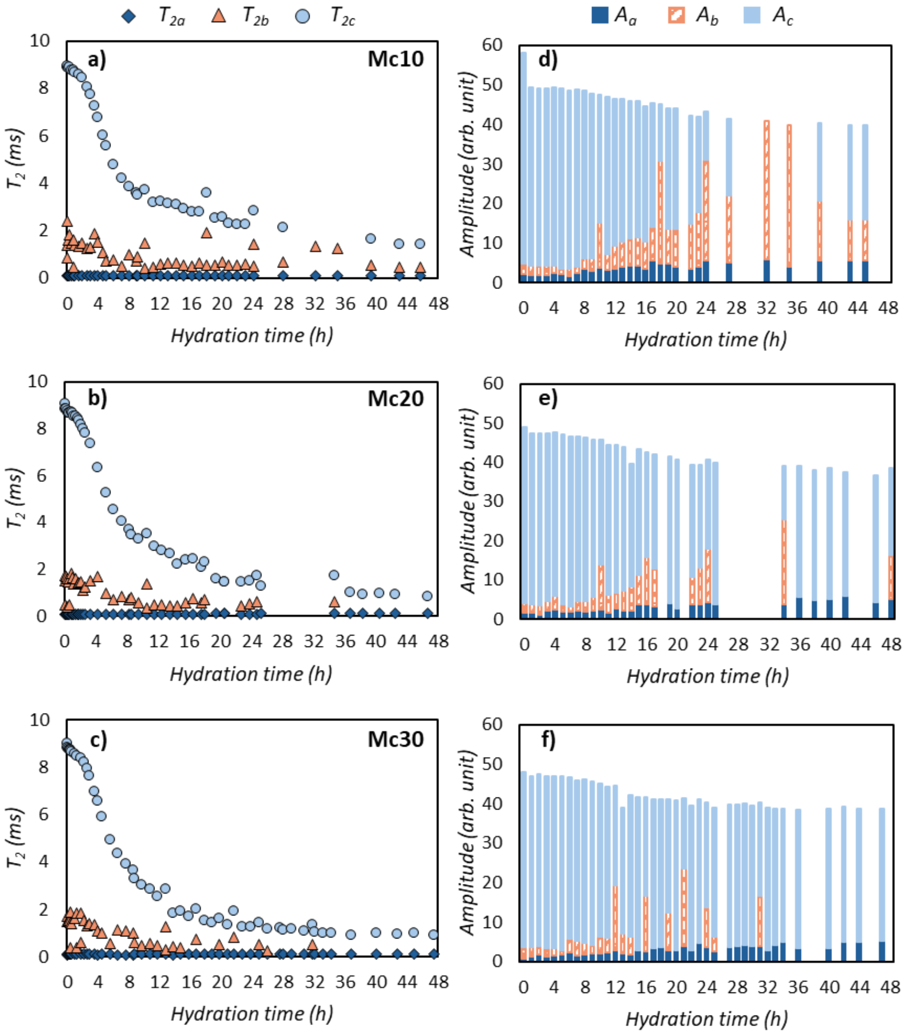

Figure A1. Change of the **a-c)** T_2 relaxation time values and **d-f)** amplitudes of water types in different cement pores: intra CSH sheet (dark blue, diamond), inter CSH gel (orange, triangle) and smaller capillary pores (light blue, circle) over the hydration of 10-30% metakaolin containing cement composites.

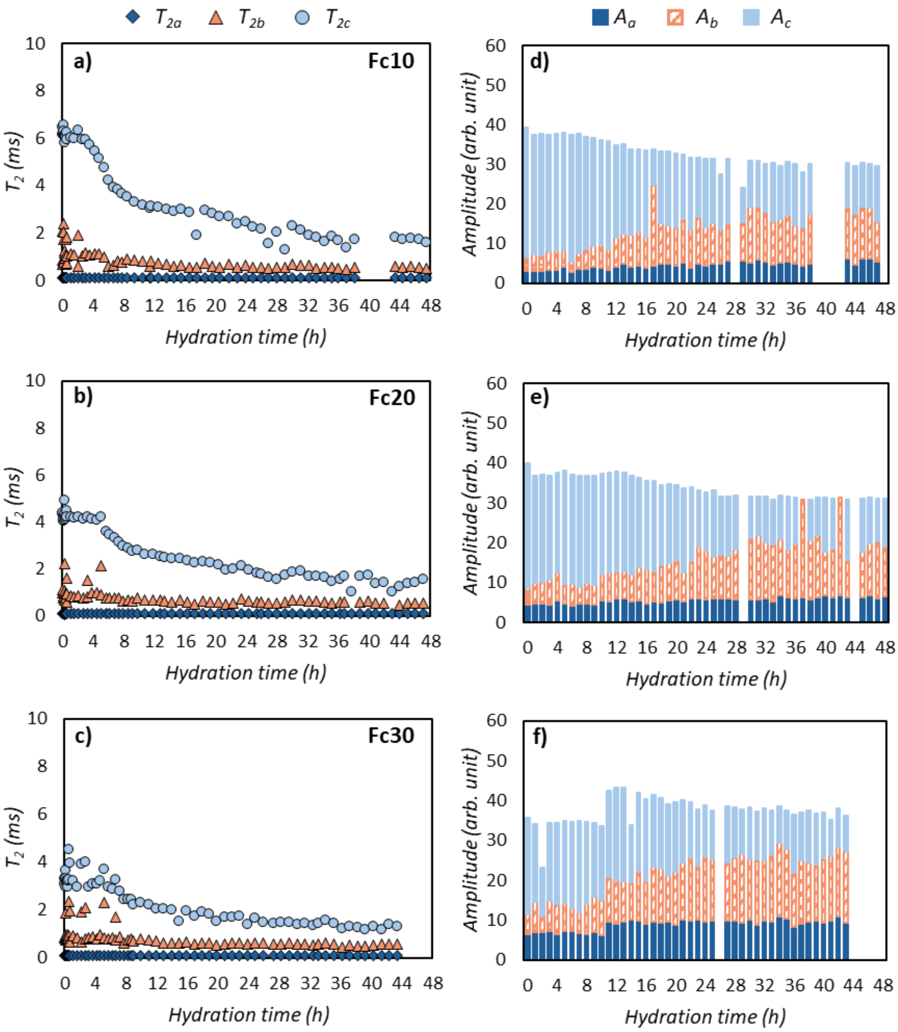

Figure A2. Change of the **a-c)** T_2 relaxation time values and **d-f)** amplitudes of water types in different cement pores: intra CSH sheet (dark blue, diamond), inter CSH gel (orange, triangle) and smaller capillary pores (light blue, circle) over the hydration of 10-30% fly ash containing cement composites.

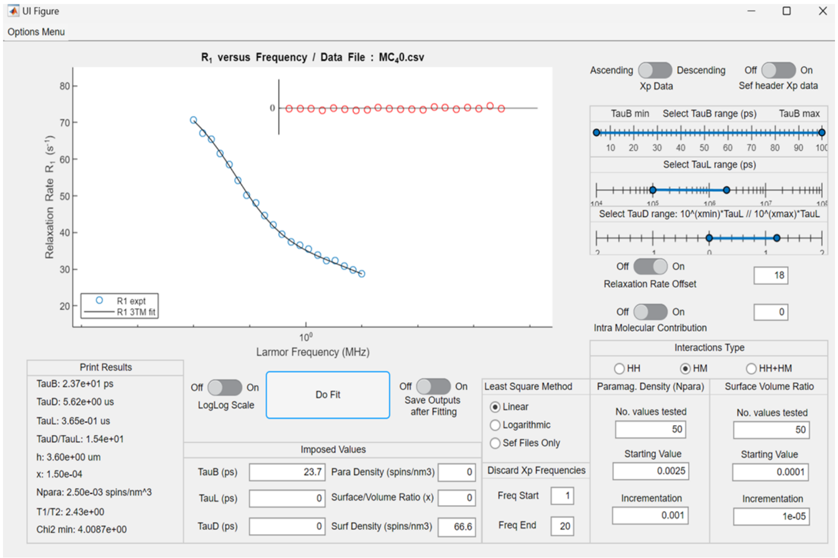

Print Results
TauB: 2.37e+01 ps
TauD: 5.62e+00 us
TauL: 3.65e-01 us
TauD/TauL: 1.54e+01
h: 3.60e+00 um
x: 1.50e-04
Npara: 2.50e-03 spins/nm^3
T1/T2: 2.43e+00
Chi2 min: 4.0087e+00

Off ○ On LogLog Scale
Off ○ On Save Outputs after Fitting

Imposed Values
TauB (ps): 23.7
TauL (ps): 0
TauD (ps): 0
Para Density (spins/nm3): 0
Surface/Volume Ratio (x): 0
Surf Density (spins/nm3): 66.6

Least Square Method
● Linear
○ Logarithmic
○ Sef Files Only

Discard Xp Frequencies
Freq Start: 1
Freq End: 20

Ascending ○ Descending Xp Data
Off ○ On Sef header Xp data
TauB min Select TauB range (ps) TauB max
Select TauL range (ps)
Select TauD range: 10^(xmin)*TauL // 10^(xmax)*TauL

Off ○ On Relaxation Rate Offset: 18
Off ○ On Intra Molecular Contribution: 0

Interactions Type
○ HH ● HM ○ HH+HM

Paramag. Density (Npara)
No. values tested: 50
Starting Value: 0.0025
Incrementation: 0.001

Surface Volume Ratio
No. values tested: 50
Starting Value: 0.0001
Incrementation: 1e-05

Figure A3. Fitting of the T_1 dispersion curve of pure Portland cement at t= 40 min of the hydration process by 3TM fitting software provided by Kogon and Faux. [176]

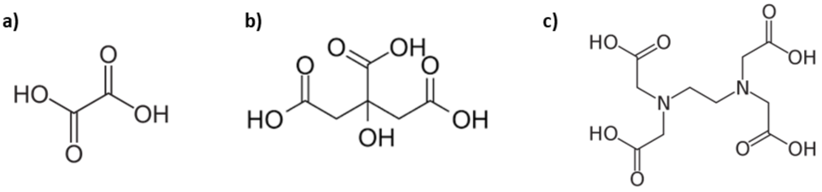

Figure A4. Chemical structure of **a)** oxalic acid, **b)** citric acid and **c)** EDTA (ethylenediaminetetraacetic acid).

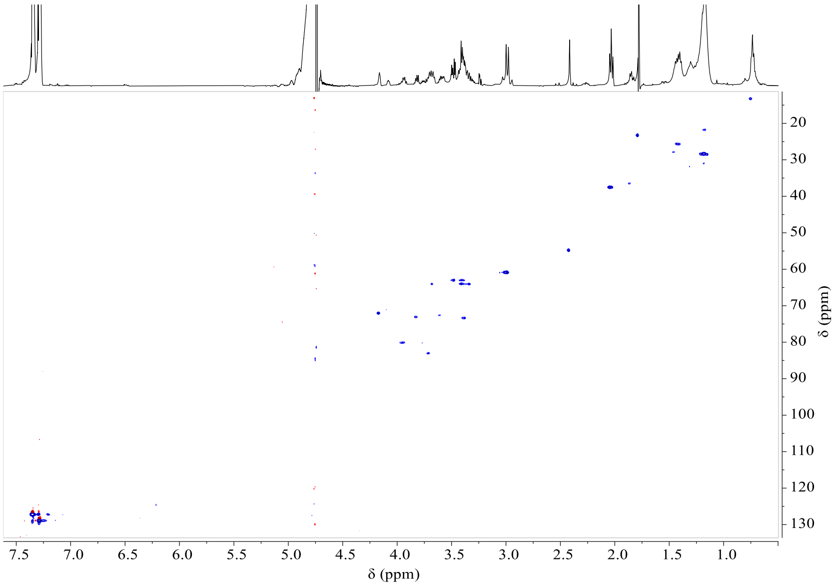

Figure A5. HSQC NMR spectrum of the organic compounds leached from the 5 g/l complexing agent containing model cemented waste package (500 MHz, 298 K).

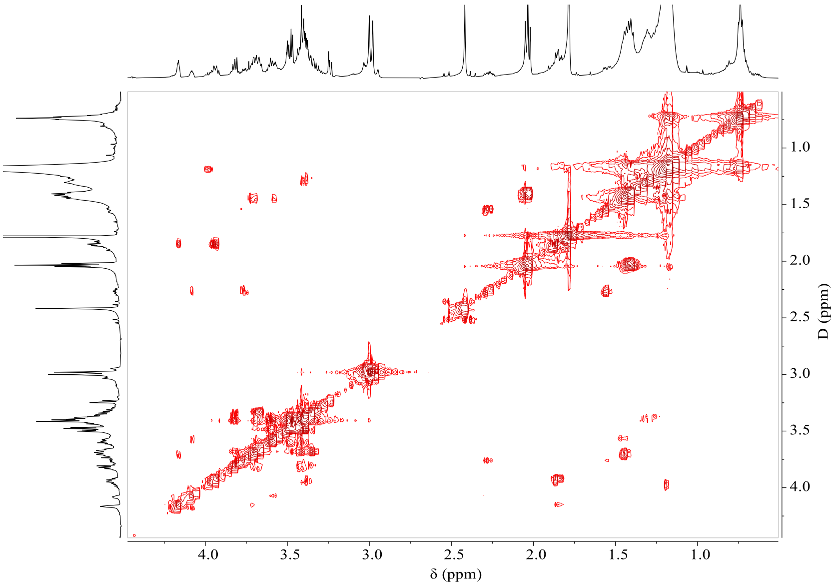

Figure A6. COSY NMR spectrum of the organic compounds leached from the 5 g/l complexing agent containing model cemented waste package (500 MHz, 298 K).

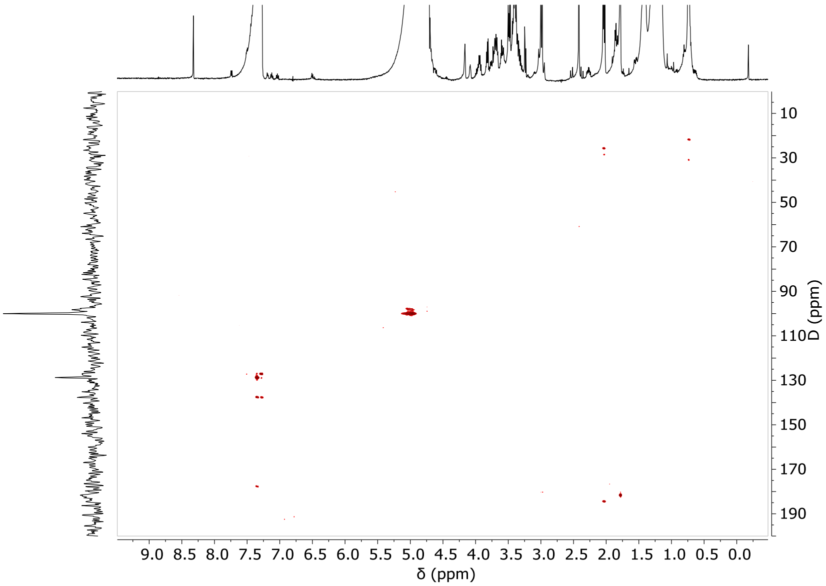

Figure A7. HMBC NMR spectrum of the organic compounds leached from the 5 g/l complexing agent containing model cemented waste package (500 MHz, 298 K).

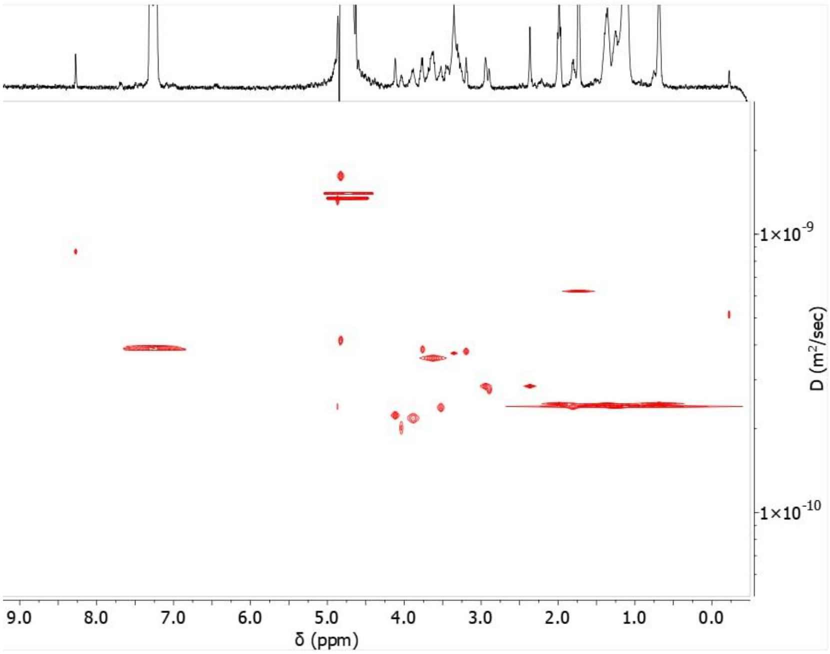

Figure A8. DOSY NMR spectrum of the organic compounds leached from the 5 g/l complexing agent containing model cemented waste package (400 MHz, 298 K).

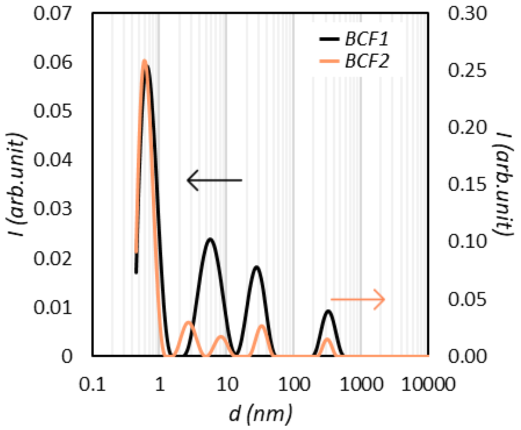

Figure A9. The derived size distribution curves of BCF1(black) and BCF2 (orange) samples in water-saturated state.

Detailed kinetics of the swelling process of bentonite

The liquid uptake of bentonite over the swelling process depends on its swelling capacity and the internal specific boundary area. The former means that bentonite can only take up a certain amount of liquid (*W*), which corresponds to its swelling capacity (W_c).[258, 259] The internal specific boundary area indicates the sites, which have not interacted with the solvent at time *t* yet but are supposed to do it later.[258, 259] This means that when bentonite gets in contact with water, water molecules can form two binding sites, one for itself and one for another molecule by breaking the secondary interactions.[256] The process can be described on the basis of the interpretation of Schott by the following equations:[256, 258, 259]

$$L + 2W_c \overset{k_1}{\rightarrow} W + {W_c}^* \qquad \text{(A1)}$$

$$ {W_c}^* + L \overset{k_2}{\rightarrow} W \qquad \text{(A2)}$$

where *L* is the liquid, W_c is the swelling capacity of the polymer, *W* is the amount of liquid taken up, and ${W_c}^*$ is the remaining liquid capacity. Expressing the liquid uptake in time leads to **Equation A3-A6**:

$$2\frac{d[W]}{dt} = k_1[L][W_c]^2 + k_2[L][{W_c}^*] \qquad \text{(A3)}$$

$$\frac{d[{W_c}^*]}{dt} = k_1[L][W_c]^2 - k_2[L][{W_c}^*] \qquad \text{(A4)}$$

$$[{W_c}^*] = \frac{k_1[L][W_c]^2}{k_2[L]} \qquad \text{(A5)}$$

$$2\frac{d[W]}{dt} = k_1[L][W_c]^2 + \frac{k_2[L]k_1[L][W_c]^2}{k_2[L]} \qquad \text{(A6)}$$

Simplify with $k_2[L]$, **Equation A6**. turns into the following form:

$$\frac{d[W]}{dt} = k_1[L][W_c]^2 \tag{A7}$$

Due to the excess amount of the liquid, $[L]$ can be considered as constant, and we get to the second-order equation of swelling:

$$\frac{d[W]}{dt} = k_1[W_c]^2 = k_1[W_\infty - W]^2 \tag{A8}$$

where W_∞ is the equilibrium liquid uptake, and k_1 equals to k_s mentioned above.

The described process is schematically shown in **Figure A10**.

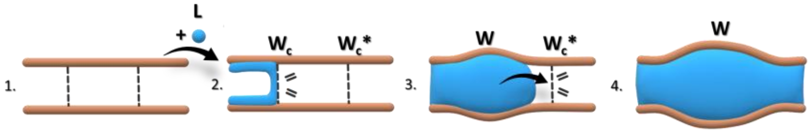

Figure A10. Schematic picture of the bentonite swelling process according to the second-order kinetics with the two, swelling rate-determining steps. L is the liquid, W_c is the swelling capacity of the clay, W is the amount of liquid taken up, and W_c^* is the remaining liquid capacity.[256] The brown lines indicate the lamellas/particles in bentonite.